Lysosome Disrupting Transformable Peptide Amphiphiles & Orally Available CRISPR-Cas Ribonucleoprotein for Genome Editing

By

CHRISTOPHER M. BAEHR
DISSERTATION

Submitted in partial satisfaction of the requirements for the degree of

DOCTOR OF PHILOSOPHY

in

Biomedical Engineering

in the

OFFICE OF GRADUATE STUDIES

of the

UNIVERSITY OF CALIFORNIA

DAVIS

Approved:

Kit S. Lam, Chair

Yuanpei Li

Eduardo Silva

Kermit Caraway

Committee in Charge

2021

ACKNOWLEDGEMENTS

First, I would like to thank Dr. Kit S. Lam for building an excellent environment to think, dream and work on the scientific endeavor in exciting and innovative ways. Dr. Lam has an incredibly imaginative perspective that I hope to imbibe in my ongoing work, and I thank him for his excellent mentorship throughout the last five years.

I thank my committee members, Dr. Carraway, who allowed my work to be showcased at the annual cancer symposium, and has contributed several ideas to the CPTNP project. Dr. Silva has given me very reliable professional advice through the years. And Dr. Li, who has been highly supportive and immensely helpful throughout my time at UC Davis.

I want to thank all my collaborators, without whom these projects could not have been completed. Particularly Dr. Lu Zhang, who involved me in his projects, and helped me learn essential project development skills. Dr. Lei Wang who worked with fiber-forming materials previously and helped develop the CPTNP project. Dr. David Segal and Dr. Henny O'Geen who have been endlessly supportive and introduced me to genome editing. Dr. Holland Cheng, Dr. C.C. Chen, who originally developed the HEVNP platform, Dr. Zsophia Kiss, and Mo Baikoghi, who made significant contributions to the project.

I would further like to thank my mentors in the laboratory, Dr. Chris Li, Dr. Wenwu Xiao, and Johnathan Li, who taught me the core skills I would need to carry out the projects enclosed herein. I would like to thank Dr. Randy Carney for his help as a mentor and a friend; Randy was a constant source of ideas and helped as a

Postdoctoral fellow in the lab and a great help as a reviewer of my work as a professor. Dr. Lu Zhang helped me tremendously by working with me to develop rigorous experimental designs. I would further like to thank Dr. Urvashi Bhardwaj, without whom much more of my time in the laboratory would have been spent hungry and without reagents. I would like to thank all of my friends in the laboratory, without whom the work enclosed here would not have been possible, even if they did not work directly on the projects they include: Dr. Ruiwu Liu, Mr. Yousif Ajena, Dr. Shivani Bansal, Dr. Diedra Shorty, Dr. Shabnam Jafari, Dr. Christabelle De Souza, Dr. Marina Ricci, Dr. Cindy Lin, Mythili Ramachandran, Dr. Yanyu Huang, Sakshi Pandita, Andy Domokos, Sara Adas, XJ Yu, Yongheng Wang, Ruiqi Huang, Dr. Aaron Lindstrom, Dr. Ai-Hong Ma, Audrey Nguyen, Dr. Lucas Solano, Dr. James Shih, and Dr. Sumaira Amir.

I would like to thank all my friends and faculty in the biomedical engineering department who contributed to a welcoming and collaborative environment, without whom my experience at UC Davis would have been wholly less.

Finally, I would like to thank all of my close friends and family who have supported me in pursuing my Ph.D. I could not have completed everything here without the support networks you have provided. Again, thanks, everyone.

Abstract

Non-small cell lung cancer (NSCLC) is the largest contributor to cancer mortality in the United States. Traditional chemotherapies are toxic and prone to the development of drug resistance. Recently, several drug candidates were shown to induce lysosomal membrane permeabilization (LMP) in aggressive cancers. This has led to increased interest in lysosome dysregulation as a therapeutic target. However, approaches are needed to overcome two limitations of current lysosomal inhibitors: low specificity and potency. Here, we report the development of a transformable nanomaterial that is triggered to induce LMP of lysosomes in NSCLC. The nanomaterial consists of peptide amphiphiles, which self-assemble into nanoparticles, colocalize with the lysosome, and change conformation to nanofibrils due to lysosomal pH shift, leading to the disruption of the disruption of the lysosome, cell death, and cisplatin sensitization. We have found that this cell-penetrating transformable peptide nanoparticle (CPTNP) was cytotoxic to NSCLC cells in the low-micromolar range, synergizing cisplatin cytotoxicity four-fold. Moreover, we demonstrate CPTNP's promising antitumor effect in mouse xenograft models with limited toxicity when given in combination with low-dose cisplatin chemotherapy. CPTNPs the first example of enhanced LMP via transformable peptide nanomaterial and offers a promising new strategy for cancer therapy.

Crispr-Cas genome editing promises to revolutionize medicine as it is currently conceived; if it can overcome the challenge of targeted tissue delivery. Several CRISPR-Cas delivery systems have been developed which can systemically edit somatic tissue in vivo if IV delivered. However, no system currently exists which can edit somatic cells after the oral delivery of CRISPR-Cas. Hepatitis E virus, like nanoparticles, were originally developed by the Cheng group and have previously been used to deliver plasmid-based vaccines orally and are a strong platform for the oral delivery of nucleic acid and protein cargos. Herein we develop Cas9 ribonucleoprotein-loaded Hepatitis E virus-like nanoparticles capable of delivering CRISPR-Cas editing systems in vivo via the oral route. We demonstrate 39% editing efficiency in vitro and up to 10% editing efficiency in the crypts of small intestinal tissue. This is the first example of orally available Crispr-Cas gene editing.

Together these systems represent two novel nano-systems which make major advancements in self-assembling cancer therapeutics and orally available gene editing.

Table of Contents

1. **Introduction**

Here I will introduce critical backgrounds for the projects included herein. Firstly, I will discuss the history and development of self-assembling peptide nanomaterials for cancer therapy and other key backgrounds in the development of chapters 2 & 3. Secondly, I will discuss the history and development of CRISPR-Cas delivery systems and key backgrounds for chapter 4.

1.1. History and Development of Self Assembling Peptide Nanomaterials for Cancer Therapy

The first self-assembling nanofibers created from chains of amino acids blinked into existence 2-3 billion years ago, with the advent of actin, tubulin, and intermediate filaments, the cytoskeleton, and distinguishing feature of eukaryotic cells. Precursor filaments may be traced back even further if we consider MreB a prokaryotic cousin to actin.[1] Synthetic technology has caught up with some delay, in many instances inspired by their natural cousins. Recently, bioinspired nanofiber forming peptide amphiphiles have garnered interest as cancer therapeutics through a variety of mechanisms ranging receptor ligand-responsive material,[2,3] to enzymatically triggered nanofiber formation,[4–6] and pH-sensitive materials.[7] These ‘programable’ materials offer several advantages to traditional chemotherapeutics, including site-specificity, extended tumor retention, and high biocompatibility. Moreover, these novel therapeutics also lend themselves to rational design based on common motifs and several rules of self-assembly that may be easily transferred to new designs. In this introductory chapter, we will discuss the

development of peptide nanofibers and the current application of these materials in cancer therapy.

Alzheimer's disease is a neurodegenerative disease typically characterized by the deposition of two types of amyloid plaques in the brain parenchyma. Intracellular deposition of the misfolded tau protein creating neurofibrillary 'tangles'.[8] And more prominently, the beta-amyloid protein. Alzheimer's plaques are comprised primarily of beta-amyloid proteins formed after the cleavage of the Alzheimer's precursor protein (APP) by beta & gamma secretases, resulting in a 37-49 amino acid residue peptide previously referred to as beta-amyloid. This beta-amyloid peptide was initially isolated and sequenced from Alzheimer's tissue samples in the late 1980s. In the 1980s and 1990s, synthetic peptides replicating the beta-amyloid peptide were synthesized. They became a standard research tool to explore the mechanistic drivers of Alzheimer's disease and other neurological amyloidoses such as Creutzfeldt-Jakob disease and BSE.[8] Perhaps the first fully synthetic peptide nanofiber was synthesized 1986.[9] The synthetic peptide consisted of residues 12-28 of the isolated beta-amyloid protein. And, indeed these AB peptide fragments are commercially available today for investigators interested in intramolecular interactions in these fibers with exciting results. Eventually, the pentapeptide sequence KLVFF was identified as the primary nucleation site of beta-amyloid fibrils.[10] The structure and supramolecular chemistry of beta-amyloid plaques were further shown to form peptide dimers via a steric zipper between two peptides and larger subunits vis pi-pi interaction of the side chains of the phenylalanine residues. Modified KLVFF peptides for treating Alzheimer's plaques would become a predecessor to some of the first synthetic supramolecular peptide therapeutics. By attaching

hydrophilic moieties to KLVFF peptides, several groups were able to modulate the critical aggregation concentration of Alzheimer plaques, thereby disrupting their formation in vivo.[10]

While beta-amyloid was being investigated for its role in senior plaques, other peptide-based nanofibers were in development for their industrial and biological applications; a group at MIT was developing an ionic charge-based platform derived from the yeast protein Zoutin.[11] One of the first examples of synthetic supramolecular peptide chemistry, these nanomaterials relied on alternating positive and negative charges $(EAEAKAKA)_n$ to form beta sheet like nanomaterials. These nanomaterials were initially inspired by the self-assembling yeast protein zoutin,[12] which carries a similar charged pattern. The original work authored by Shuguang Zhang and published in PNAS after a series of rejections in 1993 would go on to be a seminal paper in the early years of peptide-based supramolecular chemistry.[11] The self-assembling properties of the peptide were first discovered when the group introduced the compound to nerve growth factor-differentiated rat PC-12 cells in DMEM. The compound did not affect the cells as they expected but formed membraneous superstructures in solution. The group then stained the structures with congo red, and discovered that the dye incorporated into the structures, an indicator of pleated beta-sheets. The circular dichromacy spectra and electron microscopy would reinforce this assertion.[11] Zhang's group would continue to develop the charge-based platform, producing a wide range of nanomaterials by modifying the charge-charge interactions and end groups.

Zhang's work would quickly turn to the application space. Zhang demonstrated in 1995 that the membranous beta-sheet forming peptide material could be used as a 3D

scaffold for tissue growth. When an RGD peptide was incorporated into the nanomaterial structure, several cell types could be grown on the surface of the material, including primary human fibroblasts, making the platform an attractive medium for tissue engineering at the time.[13]

Early work in the ‘00s with the platform focused on developing structures that promoted neurite outgrowth of primary neurons, a unique property of these materials at the time.[14] The above work would result in the founding of 3DMatrix and eventually the FDA approval of the self-assembling product, PuraSinus in 2019, which self assembles into wound healing gel when in contact with physiological fluids. The system replaces current would packing materials and offers advantages in adhesion prevention, hemostasis, and wound healing.

At the same time Harlgerink et al would develop similar materials which could engender mineralization. These mineralized materials provided devel a good platform for osteocyte growth.[15] This work would lay the groundwork for the first spike in nanofiber material development addressing the needs of tissue engineering. Tissue engineering applications would dominate the peptide nanofiber field from 2005-2010.

1.2. Nanofibers for Cancer Therapy

As the nanomaterial community became increasingly interested in cancer therapeutics, bio-inspired nanofiber platforms were no exception. In 2010 Stupp et al. published the first work detailing peptide nanofibers as a cancer therapeutic.[16] The group designed amphiphilic peptides with the membrane disruptive KLAK sequence. The nanomaterial was more readily taken up than the peptide alone leading to

cytotoxicity in vitro.[17] Several works would follow, which would demonstrate anticancer effects in vitro and in vivo.[18–20] This work would spur a new wave of cancer therapeutic nanofibers. Other groups would develop peptide nanofiber-based hydrogels capable of delivering chemotherapies.[21]

These new materials would continue to develop and currently can be classified into roughly four groups of nanomaterials based on conditions leading to self-assembling: (1) materials assembling on the principal of enzymatic cleavage, (2) critical aggregation concentration has been reached, (3) receptor-mediated nanofiber formation, and (4) pH-mediated nanofiber formation. I will describe each of these groups and outline a few key publications for each example.

In the mid-2010s, several groups reported on enzyme ‘instructible’ peptide nanofiber prodrugs. The prodrugs consist primarily of three critical domains: 1) a hydrophobic group, typically an alkyl tail or aromatic group, 2) a fiber-forming peptide, typically a zwitterionic motif or a beta-amyloid mimetic motif-containing at least two phenylalanine groups as discussed above, and 3) a hydrophilic, enzymatically cleavable peptide, which prevents fibril formation. Once cleaved and the critical aggregation concentration is satisfied, these materials form a fibril network, or ‘gelate’. This fibril formation disrupts critical processes, intra or extracellularly, depending upon the location of the enzyme. This tri-domain structure would set the format of peptide nanofiber platforms for the rest of the decade.

These systems have been explored since at least 2007, [22,23] But the first reported fibril forming prodrug was reported by Tanakada et al., where a peptide gelator with alkyl tail and an MMP7 cleavable sequence was synthesized. The peptide was shown to

selectively gelate inside MMP7 overexpressing cancer cells, thus selectively targeting cancer cells in vitro.[6] Kuang et al. would develop similar di-peptides with a carboxylesterase cleavable sulfate group, a double phenylalanine as the fiber forming motif, and an aromatic naphthalene as the hydrophobic moiety. Once inside the cell, this compound formed a nano fibular network, disrupting actin formation and inducing cisplatin sensitization and cell death.[24] Many other enzyme-instructible self-aggregating (EISA) compounds would be explored for their anti-cancer activity over the coming decade. [5,6,24–28]

The critical aggregation concentration (CAC) is the critical concentration at which a self-aggregating material assembles. While most every self-assembling material has a CAC, some groups have used this principle, coupled with Spatio-temporal control of the material to cause the selective formation of peptide nanofibers. A prime example of this is the work of Jeena et al., 2017-19.[29–31] Wherein peptide amphiphiles containing the hydrophobic pyrene, the amino acids Phe-Phe and a mitochondrial targeting moiety. The mitochondrial targeting moiety causes the material to reach its CAC in the mitochondria but not elsewhere, thereby selectively forming nanofibers in the mitochondria. These materials are selective for certain cancer lines, likely because of the mitochondria's increased number and activity.

Receptor-ligand mediated fibril assembly is a unique approach whereby the designed peptide amphiphile consists of three key motifs. First, a hydrophobic domain, followed by the fibril forming domain, finally, a hydrophilic-ligand binding domain is included. When this ligand-binding domain interacts with its target, the nanofiber is allowed to form. Lu et al. in the Lam lab first demonstrated this in 2020, wherein the tri-

domain peptide consisted of HER2 binding peptide, a KLVFF based peptide amphiphile, and bis-pyrene, a fluorescent hydrophobe.[3] Such transformable peptide amphiphiles would self-assemble into nanoparticles under aqueous conditions and transform in vitro or in vivo into a nanofibril network upon interaction with HER2 protein. This non-toxic nanomaterial significantly reduced tumor burden in two separate breast cancer xenograft models by inhibiting HER2 dimerization. Later iterations of this mechanism proved to be effective at remaining in the tumor microenvironment, but that the tumor inhibitory effect is a feature of the particular ligand-receptor interaction.[2]

Several groups have explored the development of pH-responsive self-assembling nanofibers, as we will detail later in this dissertation.[7,32,33] However, in many tumors, the tumor microenvironment carries a slightly acidic pH compared to other tissues. As seen in the receptor-mediated nanofiber assembly nano-platform above, the extended tumor retention properties of tumor assembling nanomaterials can be attractive for phototherapeutic or drug delivery platforms. So it is no surprise that some groups have developed materials that may be triggered to self-assemble by the acidic pH of the tumor microenvironment .[32] Our group has developed materials that are triggered by the lysosomal pH shift to form nanofibers.[7] If the reader is interested in these materials, continue to chapters 2 &3.

1.3. Non-Small cell lung cancer

NSCLC is, by modern standards, an imprecise term and refers to a broad range of lung cancers, including adenocarcinoma, squamous-cell carcinoma, large-cell carcinoma, and more poorly differentiated variants, NSCLC- not otherwise specified.

However, this last characterization is continuously being refined. These characterizations of NSCLC are largely therapy driven, i.e. bevacizumab, has toxic effects in squamous-cell carcinoma while pemetrexed has no or little activity in the same tumor type. While the quality of life and progression-free survival had improved for patients with specific and predictable biomarkers and those susceptible to immunotherapy, those reliant on chemotherapy had not enjoyed the same benefits.[35] This is despite the fact that the standard of care for stage IIIB and IV is still platinum base chemotherapy.[36]

Platinum-based chemotherapies are cytotoxic to all rapidly dividing cells, primarily by crosslinking pyridine bases in DNA. These cisplatin-DNA adducts prevent proliferation and induce apoptosis.[37] Unfortunately, this affects many other tissues in addition to the tumor space. Common side effects from systemic platinum-based chemotherapy include nausea and vomiting, myelosuppression, neuropathy, ototoxicity, hepatotoxicity, and nephrotoxicity.[37] The most common dose-limiting toxicity in cisplatin therapy is peripheral neurotoxicity. Ataxia and vibration sense is often lost after the first few treatment cycles, followed by cumulative and irreversible ototoxicity. Carboplatin is generally better tolerated and is frequently dose limited by myelosuppression.[38] Low patient tolerance for these drugs often leads to dose reduction, which can spur tumor resistance and poor tumor response, and thereby poor prognosis.

1.4 The Lysosome

Lysosomes are found in all eukaryotic cells; however, their size, structure, and function can significantly differ. Plant and yeasts tend to have a single or few lysosomes

(sometimes called vacuoles) of several micrometers in diameter. Metazoan cells, by contrast, can have hundreds of lysosomes typically ranging in size from 0.1 – 1μM.[39] The lysosome is a membrane-bound organelle traditionally conceptualized as the 'garbage' center of the cell. Most prolifically, it is decorated with transmembrane proteins, Lysosomal Associated Membrane protein 1 and Lysosomal Associated Membrane Protein 2 (LAMP1 & LAMP2). These proteins are heavily glycosylated on their luminal side, which provides the lysosomal membrane protection from the luminal lytic enzymes of the lysosome. The enzymatic components of the lysosome are tuned to operate at the acidic pH of the lysosome, which is roughly between 4-5.5 and can digest a wide range of macromolecules. The end products of this digestion are either returned to the cytoplasm for use in biosynthetic reactions or stored for later use by the cell.[40]

The lysosome plays a major role in the breakdown and release of critical metabolic components; In cancer, where the pathology is often driven by high catabolism, lysosomal function tends to be highly modified, particularly in aggressive tumors.[39] Autophagy, macropinocytosis, and endocytosis all tend to be upregulated in aggressive tumors. These lysosomal alterations correlate well with angiogenesis and cancer metastasis,[41] and are mediated via down-regulation in lysosomal-associated membrane protein 1 & 2 (LAMP1,2), up-regulation of oncogenes Src and Ras, and alteration of the localization of HSP70.[42] While changes centered around lysosomal metabolism and exocytosis confer a proliferative advantage to cancer cells,[43–46] they also promote instability of the lysosomal membrane, making lysosomal membrane permeation (LMP) a promising cancer therapeutic target.[47]

1.5 Crispr Cas9 Delivery

One of the most considerable remaining challenges to therapeutic, in vivo, CRISPR-Cas genome editing is efficient and targeted delivery of genome editing tools to specific organ or cell types of interest. To date, several approaches to in vivo delivery of CRISPR-Cas have been attempted with varying levels of success. These approaches include physical methods like microinjection and electroporation, alongside chemical methods like targeting ligands, lipid nanoparticles, gold nanoparticles and adeno-associated viruses. In this subsection, we will explore current in vivo CRISPR-Cas delivery tools and platforms.

1.5.1 Brief History of CRISPR-Cas

Early interest in Clustered Regularly Interspaced Short Palindromic Repeats (CRISPRs) originated from a series of bioinformatics studies which revealed that spacer sequences in CRISPRs were sometimes identical to sequences found in phages and plasmids.[49,50] These observations would eventually lead to the revelation that CRISPRs were critical components of bacterial and Archaeal active immune systems.[51,52] A series of mechanistic studies would follow and show that the CRISPR loci are processed into a library of RNAs that guide nucleases to sequence-specific nucleic acid targets.[53] In 2012, the first example of directed DNA cleavage by a cas9 system was published.[54] In 2013, two groups would post studies detailing directed editing in mammalian cells.[55,56] Figure 1 describes what happened next.

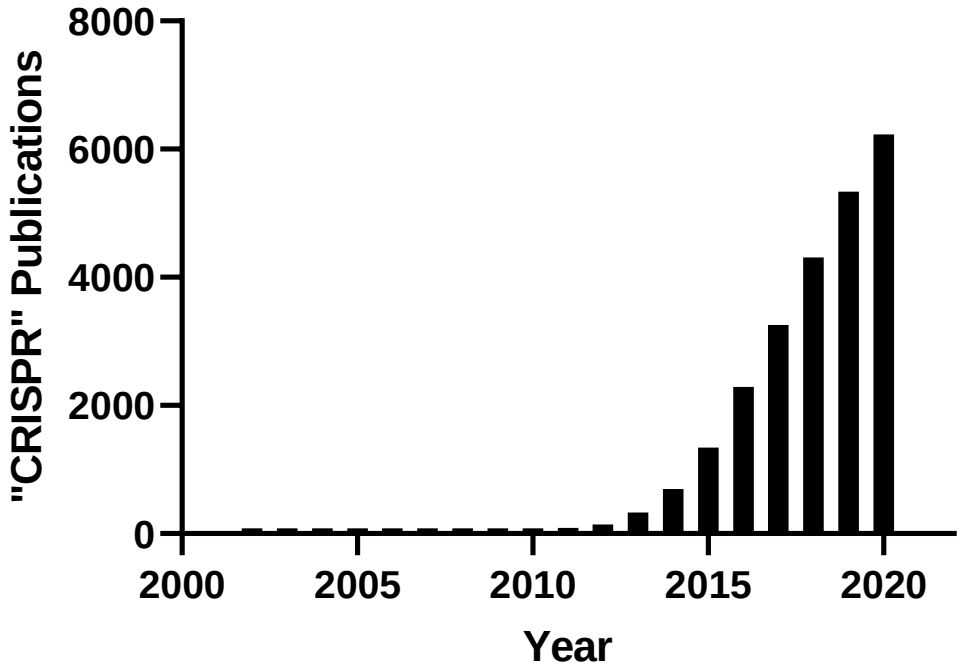

Figure 1: Pubmed results for “CRISPR” annualized and displayed.

1.5.2. Delivery

Once it was established that CRISPR-Cas9 systems could effectively edit DNA in a range of organisms, the rush to find therapeutic applications and adequate delivery systems began.

Here we will organize in vivo delivery systems by vehicle. We will discuss five broad categories; each system has its advantages and disadvantages, alongside a history of use, which we will discuss in the coming passages.

Hydrodynamic injection

Perhaps the most straightforward method of administrating CRISPR-Cas9 gene-editing tools is the direct intravenous injection of large volumes (8-10% of body weight) of an aqueous solution of plasmid DNA encoding for Cas9 and sgRNA. The

hydrodynamic pressure produces pores in the membrane of some endothelial cells and allows for transfection with the plasmid. Such techniques were the subject of the first in vivo gene editing study targeting the Fah mutation, a mouse model of tyrosinemia.[57] Predictably, the editing efficiency of this technique is low; Yin et Al. achieved 0.4% six days after treatment. However, in some cases, this may be sufficient to correct disease states. In Yin et al., 0.4% editing was adequate to prevent weight loss in $FAH^{mut/mut}$ mice.

However, despite its success in small animals, hydrodynamic injection has been less promising in humans; previous clinical trials utilizing hydrodynamic injection failed due to the development of cirrhosis.[58]

Electroporation

Electroporation has long been used to introduce plasmids or other materials into cells, and it can be carried out in vivo. So, it is no surprise that electroporation was used as an early in vivo CRISPR-Cas9 delivery tool. Electroporation allows the incorporation of extracellular materials into the cell by inducing temporary membrane poration induced via a short electrical discharge. In this way, plasmids or other materials that would generally remain outside the cell can be incorporated and expressed.[59] In utero murine studies of plasmid delivery via electroporation revealed two-fold higher editing vs hydrodynamic injection and a 91% survival rate. [60] Electroporation may enhance the delivery of RNP and mRNA systems as well, however, in adult organisms, electroporation is limited by cytotoxicity and locality.

Viral vector delivery systems

Several viral vectors have been explored for their capacity to deliver CRISPR-Cas9 payload, but perhaps the most available vehicle is an adeno-associated virus (AAV). AAV has several advantages over other viral vectors because it carries single-strand DNA (ssDNA); it is rarely incorporated into the host genome, which can lead to toxicity in other vectors. The ssDNA may also be encoded as donor DNA for knock-in.[61] Moreover, several AAV platforms have already been FDA approved or are currently moving through clinical trials.[62] Together, these factors made AAV a ripe platform for some of the first examples of in vivo genome engineering. Conducted just two years after the first demonstration of DNA editing via CRISPR-Cas9 systems, AAV encoding Cas9 and gRNA targeting PCSK9 was shown to edit ~50% of liver hepatocytes after tail vein injection and lower cholesterol levels by 35-40%.[63] AAV technology has continued to develop with the advent of base-editing[64] technology. Recently, the Liu group utilized a dual AAV system to rescue a mouse model of Hutchens Gilford progeria.[65]

Lipid Nanoparticles

Lipid nanoparticles (LNP) have come of age in the aftermath of the Sars-Cov2 global pandemic, as lipid nanomaterials containing messenger RNA (mRNA) constitute the two most successful vaccines for the protection of Covid19.[66] LNPs containing base-editor mRNA have proven to be similarly effective in editing PCSK9 the liver of primates.[67,68] Musunuru et al. reports near-complete PCSK9 knockdown in the liver with a single dosage of mRNA-loaded LNPs, alongside a reduction of blood PCSK9 levels by 90% and low-density lipoprotein by 60%. These findings come only seven years after

the first PCSK9 knockdown studies utilizing AAV and nine years after the first publication of DNA editing via CRISPR-Cas9.

Typically, LNPs consist of positively charged lipids complexed with negatively charged nucleic acids. Complexed particles can be uptaken by endocytosis or macro-pinocytosis. Several commercial products exist for LNP encapsulation of DNA, RNA, or even RNPs.[69] LNPs still face challenges in systemic delivery of material outside of the liver, however, several LNP formulations have been shown to deliver to alternative sites.[70,71]

RNP delivery systems

RNP is generally considered to be the most efficient modality for difficult to transfect and somatic cells.[72] Additionally, because the Cas9 and sgRNA are complexed before introduction into the cell, fewer off-target effects are generated by RNPs when compared with mRNA and plasmid. Large-scale production of RNP may be easier in some ways with RNP. However, a limited number of RNP delivery systems have been developed. As mentioned above, some LNP systems capable of encapsulating RNPs have been created. Additionally, other groups have complexed RNPs with cell-penetrating peptides to induce editing.[73]

Chen et al. developed a biodegradable capsid capable of delivering RNP with high efficiency in vitro and intra-retinal and intramuscularly in vivo.[74] The system is more efficient than Lipofectamine in vitro and can be surface conjugated with peptides to improve delivery.

Hamilton et al. developed a lentiviral capsid capable of encapsulating a cas9 RNP. This system efficiently edited $CD4^+$ T cells ex vivo.[75] Overall, RNP delivery platforms appear to have a bright future which we will discuss later in this document.

1.6. Conclusion

Self-assembling peptide nanomaterials have developed dramatically from the initial development of beta-amyloid peptides to cell-adhesive hydrogels, to finally cancer therapeutics. These materials have demonstrated ability to reduce tumor burden in vivo through a variety of mechanisms. As these systems continue to develop, we expect to see increasingly innovative approaches and perhaps appearances in the clinic.

Several major nanomaterial platforms exist for the systemic delivery of CRISPR-Cas gene-editing tools. While AAV and mRNA platforms have had demonstrated success in large animals delivering gene-editing technology, RNP delivery platforms are still in their infancy despite numerous advantages. In the third chapter of this document, we will detail our efforts to develop a targeted and orally available RNP delivery vehicle for intestinal genome editing.

1.7. References

1. Amos, L. A., van den Ent, F. & Löwe, J. Structural/functional homology between the bacterial and eukaryotic cytoskeletons. *Curr. Opin. Cell Biol.* **16**, 24–31 (2004).
2. Zhang, L. *et al.* Tumor Receptor-Mediated In Vivo Modulation of the Morphology, Phototherapeutic Properties, and Pharmacokinetics of Smart Nanomaterials. *ACS Nano* **15**, 468–479 (2021).

3. Zhang, L. *et al.* Transformable peptide nanoparticles arrest HER2 signalling and cause cancer cell death in vivo. *Nat. Nanotechnol.* **15**, 145–153 (2020).
4. Zhou, Z. *et al.* Enzyme-instructed self-assembly with photo-responses for the photo-regulation of cancer cells. *Org. Biomol. Chem.* **15**, 6892–6895 (2017).
5. Dong, L. *et al.* Alkaline Phosphatase-Instructed Self-Assembly of Gadolinium Nanofibers for Enhanced T2-Weighted Magnetic Resonance Imaging of Tumor. *Anal. Chem.* **89**, 6922–6925 (2017).
6. Tanaka, A. *et al.* Cancer Cell Death Induced by the Intracellular Self-Assembly of an Enzyme-Responsive Supramolecular Gelator. *J. Am. Chem. Soc.* **137**, 770–775 (2015).
7. Baehr, C. M. *et al.* Transformable amyloid-beta mimetic peptide amphiphiles for lysosomal disruption in non-small cell lung cancer. *Biomaterials* **277**, 121078 (2021).
8. Murphy, M. P. & LeVine, H. Alzheimer's Disease and the β-Amyloid Peptide. *J. Alzheimers Dis. JAD* **19**, 311 (2010).
9. Castaño, E. M. *et al.* In vitro formation of amyloid fibrils from two synthetic peptides of different lengths homologous to alzheimer's disease β-protein. *Biochem. Biophys. Res. Commun.* **141**, 782–789 (1986).
10. Lowe, T. L., Strzelec, A., Kiessling, L. L. & Murphy, R. M. Structure−Function Relationships for Inhibitors of β-Amyloid Toxicity Containing the Recognition Sequence KLVFF. *Biochemistry* **40**, 7882–7889 (2001).
11. Zhang, S., Holmes, T., Lockshin, C. & Rich, A. Spontaneous assembly of a self-complementary oligopeptide to form a stable macroscopic membrane. *Proc. Natl. Acad. Sci.* **90**, 3334–3338 (1993).

12. Zhang, S., Lockshin, C., Herbert, A., Winter, E. & Rich, A. Zuotin, a putative Z-DNA binding protein in Saccharomyces cerevisiae. *EMBO J.* **11**, 3787–3796 (1992).
13. Zhang, S. *et al.* Self-complementary oligopeptide matrices support mammalian cell attachment. *Biomaterials* **16**, 1385–1393 (1995).
14. Holmes, T. C. *et al.* Extensive neurite outgrowth and active synapse formation on self-assembling peptide scaffolds. *Proc. Natl. Acad. Sci.* **97**, 6728–6733 (2000).
15. Hartgerink, J. D., Beniash, E. & Stupp, S. I. Self-Assembly and Mineralization of Peptide-Amphiphile Nanofibers. *Science* **294**, 1684–1688 (2001).
16. Standley, S. M. *et al.* Induction of Cancer Cell Death by Self-assembling Nanostructures Incorporating a Cytotoxic Peptide. *Cancer Res.* **70**, 3020–3026 (2010).
17. Standley, S. M. *et al.* Induction of cancer cell death by self-assembling nanostructures incorporating a cytotoxic peptide. *Cancer Res.* **70**, 3020–3026 (2010).
18. Soukasene, S. *et al.* Antitumor Activity of Peptide Amphiphile Nanofiber-Encapsulated Camptothecin. *ACS Nano* **5**, 9113–9121 (2011).
19. Toft, D. J. *et al.* Coassembled cytotoxic and pegylated peptide amphiphiles form filamentous nanostructures with potent antitumor activity in models of breast cancer. *ACS Nano* **6**, 7956–7965 (2012).
20. Zha, R. H., Sur, S. & Stupp, S. I. Self-assembly of Cytotoxic Peptide Amphiphiles into Supramolecular Membranes for Cancer Therapy. *Adv. Healthc. Mater.* **2**, 126–133 (2013).

21. Wu, M., Ye, Z., Liu, Y., Liu, B. & Zhao, X. Release of hydrophobic anticancer drug from a newly designed self-assembling peptide. *Mol. Biosyst.* **7**, 2040–2047 (2011).
22. Law, B., Weissleder, R. & Tung, C.-H. Protease-sensitive fluorescent nanofibers. *Bioconjug. Chem.* **18**, 1701–1704 (2007).
23. Yang, H., Fung, S.-Y., Pritzker, M. & Chen, P. Modification of hydrophilic and hydrophobic surfaces using an ionic-complementary peptide. *PloS One* **2**, e1325 (2007).
24. Li, J. *et al.* Enzyme-Instructed Intracellular Molecular Self-Assembly to Boost Activity of Cisplatin against Drug-Resistant Ovarian Cancer Cells. *Angew. Chem. Int. Ed.* **54**, 13307–13311 (2015).
25. Du, X. *et al.* In situ generated D-peptidic nanofibrils as multifaceted apoptotic inducers to target cancer cells. *Cell Death Dis.* **8**, e2614–e2614 (2017).
26. Zhou, Z. *et al.* Enzyme-instructed self-assembly with photo-responses for the photo-regulation of cancer cells. *Org. Biomol. Chem.* **15**, 6892–6895 (2017).
27. Liang, C. *et al.* Enzyme-assisted peptide folding, assembly and anti-cancer properties. *Nanoscale* **9**, 11987–11993 (2017).
28. Bellat, V. *et al.* Functional Peptide Nanofibers with Unique Tumor Targeting and Enzyme-Induced Local Retention Properties. *Adv. Funct. Mater.* **28**, (2018).
29. Jeena, M. T. *et al.* Heterochiral Assembly of Amphiphilic Peptides Inside the Mitochondria for Supramolecular Cancer Therapeutics. *ACS Nano* **13**, 11022–11033 (2019).
30. Kim, S. *et al.* Intra-mitochondrial biomineralization for inducing apoptosis of cancer cells. *Chem. Sci.* **9**, 2474–2479 (2018).

31. Jeena, M. T. *et al.* Mitochondria localization induced self-assembly of peptide amphiphiles for cellular dysfunction. *Nat. Commun.* **8**, 26 (2017).
32. Wang, D. *et al.* pH-Responsive Self-Assemblies from the Designed Folic Acid-Modified Peptide Drug for Dual-Targeting Delivery. *Langmuir* **37**, 339–347 (2021).
33. Luo, S. *et al.* Targeting self-assembly peptide for inhibiting breast tumor progression and metastasis. *Biomaterials* **249**, 120055 (2020).
34. Ettinger, D. S. *et al.* Non–Small Cell Lung Cancer, Version 5.2017, NCCN Clinical Practice Guidelines in Oncology. *J. Natl. Compr. Canc. Netw.* **15**, 504–535 (2017).
35. Ettinger, D. S. *et al.* NCCN Guidelines Insights: Non–Small Cell Lung Cancer, Version 5.2018. *J. Natl. Compr. Canc. Netw.* **16**, 807–821 (2018).
36. Goldstraw, P. *et al.* Non-small-cell lung cancer. *The Lancet* **378**, 1727–1740 (2011).
37. Rossi, A. & Di Maio, M. Platinum-based chemotherapy in advanced non-small-cell lung cancer: optimal number of treatment cycles. *Expert Rev. Anticancer Ther.* **16**, 653–660 (2016).
38. Santabarbara, G., Maione, P., Rossi, A. & Gridelli, C. Pharmacotherapeutic options for treating adverse effects of Cisplatin chemotherapy. *Expert Opin. Pharmacother.* **17**, 561–570 (2016).
39. Perera, R. M. & Zoncu, R. The Lysosome as a Regulatory Hub. *Annu. Rev. Cell Dev. Biol.* **32**, 223–253 (2016).
40. Sagné, C. *et al.* Identification and characterization of a lysosomal transporter for small neutral amino acids. *Proc. Natl. Acad. Sci.* **98**, 7206–7211 (2001).
41. Piao, S. & Amaravadi, R. K. Targeting the lysosome in cancer. *Ann. N. Y. Acad. Sci.* **1371**, 45–54 (2016).

42. Kallunki, T., Olsen, O. D. & Jäättelä, M. Cancer-associated lysosomal changes: friends or foes? *Oncogene* **32**, 1995–2004 (2013).
43. Safaei, R. *et al.* Abnormal lysosomal trafficking and enhanced exosomal export of cisplatin in drug-resistant human ovarian carcinoma cells. *Mol. Cancer Ther.* **4**, 1595–1604 (2005).
44. Chi, C. *et al.* Disruption of lysosome function promotes tumor growth and metastasis in Drosophila. *J. Biol. Chem.* **285**, 21817–21823 (2010).
45. Nilsson, C., Roberg, K., Grafström, R. C. & Öllinger, K. Intrinsic differences in cisplatin sensitivity of head and neck cancer cell lines: Correlation to lysosomal pH. *Head Neck* **32**, 1185–1194 (2010).
46. Dielschneider, R. F., Henson, E. S. & Gibson, S. B. Lysosomes as Oxidative Targets for Cancer Therapy. *Oxid. Med. Cell. Longev.* **2017**, 3749157 (2017).
47. Dielschneider, R. F., Henson, E. S. & Gibson, S. B. Lysosomes as Oxidative Targets for Cancer Therapy. *Oxid. Med. Cell. Longev.* **2017**, 3749157 (2017).
48. Zhitomirsky, B. & Assaraf, Y. G. Lysosomes as mediators of drug resistance in cancer. *Drug Resist. Updat.* **24**, 23–33 (2016).
49. Bolotin, A., Quinquis, B., Sorokin, A. & Ehrlich, S. D. Clustered regularly interspaced short palindrome repeats (CRISPRs) have spacers of extrachromosomal origin. *Microbiol. Read. Engl.* **151**, 2551–2561 (2005).
50. Mojica, F. J. M., Díez-Villaseñor, C., García-Martínez, J. & Soria, E. Intervening sequences of regularly spaced prokaryotic repeats derive from foreign genetic elements. *J. Mol. Evol.* **60**, 174–182 (2005).

51. van Erp, P. B., Bloomer, G., Wilkinson, R. & Wiedenheft, B. The history and market impact of CRISPR RNA-guided nucleases. *Curr. Opin. Virol.* **12**, 85–90 (2015).
52. Barrangou, R. *et al.* CRISPR Provides Acquired Resistance Against Viruses in Prokaryotes. *Science* **315**, 1709–1712 (2007).
53. van der Oost, J., Westra, E. R., Jackson, R. N. & Wiedenheft, B. Unravelling the structural and mechanistic basis of CRISPR–Cas systems. *Nat. Rev. Microbiol.* **12**, 479–492 (2014).
54. Jinek, M. *et al.* A programmable dual RNA-guided DNA endonuclease in adaptive bacterial immunity. *Science* **337**, 816–821 (2012).
55. Mali, P. *et al.* RNA-guided human genome engineering via Cas9. *Science* **339**, 823–826 (2013).
56. Cong, L. *et al.* Multiplex genome engineering using CRISPR/Cas systems. *Science* **339**, 819–823 (2013).
57. Yin, H. *et al.* Genome editing with Cas9 in adult mice corrects a disease mutation and phenotype. *Nat. Biotechnol.* **32**, 551–553 (2014).
58. Khorsandi, S. E. *et al.* Minimally invasive and selective hydrodynamic gene therapy of liver segments in the pig and human. *Cancer Gene Ther.* **15**, 225–230 (2008).
59. Weaver, J. C. & Chizmadzhev, Yu. A. Theory of electroporation: A review. *Bioelectrochem. Bioenerg.* **41**, 135–160 (1996).
60. Kaneko, T., Sakuma, T., Yamamoto, T. & Mashimo, T. Simple knockout by electroporation of engineered endonucleases into intact rat embryos. *Sci. Rep.* **4**, 6382 (2014).

61. Wilson, R. C. & Gilbert, L. A. The Promise and Challenge of In Vivo Delivery for Genome Therapeutics. *ACS Chem. Biol.* **13**, 376–382 (2018).
62. Verdera, H. C., Kuranda, K. & Mingozzi, F. AAV Vector Immunogenicity in Humans: A Long Journey to Successful Gene Transfer. *Mol. Ther.* **28**, 723–746 (2020).
63. Ding, Q. *et al.* Permanent Alteration of PCSK9 With In Vivo CRISPR-Cas9 Genome Editing. *Circ. Res.* **115**, 488–492 (2014).
64. Gaudelli, N. M. *et al.* Programmable base editing of A•T to G•C in genomic DNA without DNA cleavage. *Nature* **551**, 464–471 (2017).
65. Koblan, L. W. *et al.* In vivo base editing rescues Hutchinson–Gilford progeria syndrome in mice. *Nature* **589**, 608–614 (2021).
66. Widge, A. T. *et al.* Durability of Responses after SARS-CoV-2 mRNA-1273 Vaccination. *N. Engl. J. Med.* **384**, 80–82 (2021).
67. Musunuru, K. *et al.* In vivo CRISPR base editing of PCSK9 durably lowers cholesterol in primates. *Nature* **593**, 429–434 (2021).
68. Paulusma, C. C. & Bosma, P. J. Therapeutic base editing in the adult liver. *Nat. Rev. Gastroenterol. Hepatol.* **18**, 597–598 (2021).
69. Lipofectamine™ CRISPRMAX™ Cas9 Transfection Reagent. https://www.thermofisher.com/order/catalog/product/CMAX00001.
70. Zhang, H., Leal, J., Soto, M. R., Smyth, H. D. C. & Ghosh, D. Aerosolizable Lipid Nanoparticles for Pulmonary Delivery of mRNA through Design of Experiments. *Pharmaceutics* **12**, 1042 (2020).

71. Cheng, Q. *et al.* Selective organ targeting (SORT) nanoparticles for tissue-specific mRNA delivery and CRISPR–Cas gene editing. *Nat. Nanotechnol.* **15**, 313–320 (2020).
72. Seki, A. & Rutz, S. Optimized RNP transfection for highly efficient CRISPR/Cas9-mediated gene knockout in primary T cells. *J. Exp. Med.* **215**, 985–997 (2018).
73. Suresh, B., Ramakrishna, S. & Kim, H. Cell-Penetrating Peptide-Mediated Delivery of Cas9 Protein and Guide RNA for Genome Editing. *Methods Mol. Biol. Clifton NJ* **1507**, 81–94 (2017).
74. Chen, G. *et al.* A biodegradable nanocapsule delivers a Cas9 ribonucleoprotein complex for in vivo genome editing. *Nat. Nanotechnol.* **14**, 974–980 (2019).
75. Hamilton, J. R. *et al.* Targeted delivery of CRISPR-Cas9 and transgenes enables complex immune cell engineering. *Cell Rep.* **35**, 109207 (2021).

2. Cell Penetrating Transformable Nanoparticles for Lysosomal Disruption

2.1. Introduction

Since the lysosome's discovery in 1955 by Christian de Duve, it has traditionally been conceptualized as the proteolytic 'garbage bag' of the cell.[1] However, current research demonstrates that the lysosome is central to various cellular processes, including nutrient scavenging, tissue remodeling, and metabolic regulation.[2] Interestingly, lysosomal aberrations such as changes in lysosomal volume, autophagic dysregulation,[3] and cellular distribution of lysosome-associated proteins have been observed in many cancer lines.[1] These lysosomal alterations correlate well with angiogenesis and cancer metastasis,[4] and are mediated via down-regulation in lysosomal-associated membrane protein 1 & 2 (LAMP1,2), up-regulation of oncogenes Src and Ras, and alteration of the localization of HSP70.[5] While changes centered around lysosomal metabolism and exocytosis confer a proliferative advantage to cancer cells,[3,6–8] they also promote instability of the lysosomal membrane, making lysosomal membrane permeation (LMP) a promising cancer therapeutic target.[9] Several lysosomal inhibitors have been reported to induce LMP in cancer cells explicitly selectively.[10] Salinomycin selectively targets cancer stem cells by inducing lysosomal sequestration of iron and inducing ferroptosis.[11] Other agents such as oleocanthal, a compound found in olive oil, selectively cause cancer cell death by inhibiting acid sphingomyelinase, thereby selectively inducing LMP.[12] Chloroquine, an anti-malarial drug currently being

studied in several human cancer trials for its synergistic effect with common chemotherapies, is traditionally thought of as an autophagy inhibitor, although some evidence suggests that it also induces LMP at high doses.[13,14] Nanomaterials with autophagic inhibitory activity are also being investigated.[15] Despite showing promise, these drugs all suffer from low selectivity for the lysosome and low potency. Therefore novel LMP inducing therapeutic agents with improved targeting and potency are needed.

Supramolecular chemistry involves the self-assembly of subunits by non-covalent interactions. Our group and others have explored the development of beta-amyloid mimetic peptide amphiphiles.[16–20] The nanoparticles self-assembled from peptide amphiphiles transform into nanofibers with β-sheet structure, which may be triggered by either ligand-receptor interactions,[21–23] pH,[24] or hydrophobic-hydrophilic modulation. Other groups have developed triggerable nanofiber forming peptides that target the cytosol[25] and the mitochondria[20]. However, no triggerable peptide nanoparticle has been designed to target the lysosome, despite the lysosome's promise as a cancer therapeutic target.[2,3,26] Here, we explore the development of a pH-sensitive transformable peptide nanoparticle comprised of beta-amyloid mimetic peptide amphiphiles. These cell-penetrating transformable peptide nanoparticles (CPTNPs) are designed to be up-taken by NSCLC cells, localize to the lysosome and transform into high aspect ratio nanofibers (**Figure 1**) due to acidic pH shift. These nanofibers induce LMP and lysosomal disruption which facilitates necrotic cell death. The nanoplatform contains three distinct motifs. First, a hydrophilic, cell-penetrating, poly-*D*-Arg motif (8-mer). Poly-arginine is a well-known cationic cell-penetrating peptide which has

previously been demonstrated to target the lysosome when associated with macromolecules.[27,28] Second, an all *D*-amino acid-containing β-sheet forming motif (kffvlk). *D*-amino acids containing peptides are expected to resist proteolytic degradation inside the lysosome. This sequence (in L-amino acids) has previously been explored by us and by others as a nanoparticle-nanofiber forming motif.[23] Third, bis-pyrene (BP) which acts as both a strong hydrophobic group and a dye for tracking of the nanoparticles. The transformation of CPTNPs may be explained by the shift in π-π interaction between phenylalanine side chains, as explored by others.[29] In this study, we demonstrate the capacity of CPTNPS to be taken up by clathrin-mediated endocytosis (CME), lysosomal delivery, and intra-lysosomal transformation of the nanomaterial, resulting in permeation of the lysosomal membrane. In addition, we were able to demonstrate that CPTNP could induce cancer cell death in the low μM range, and reduce tumor burden of xenograft model *in vivo*, with limited toxicity.

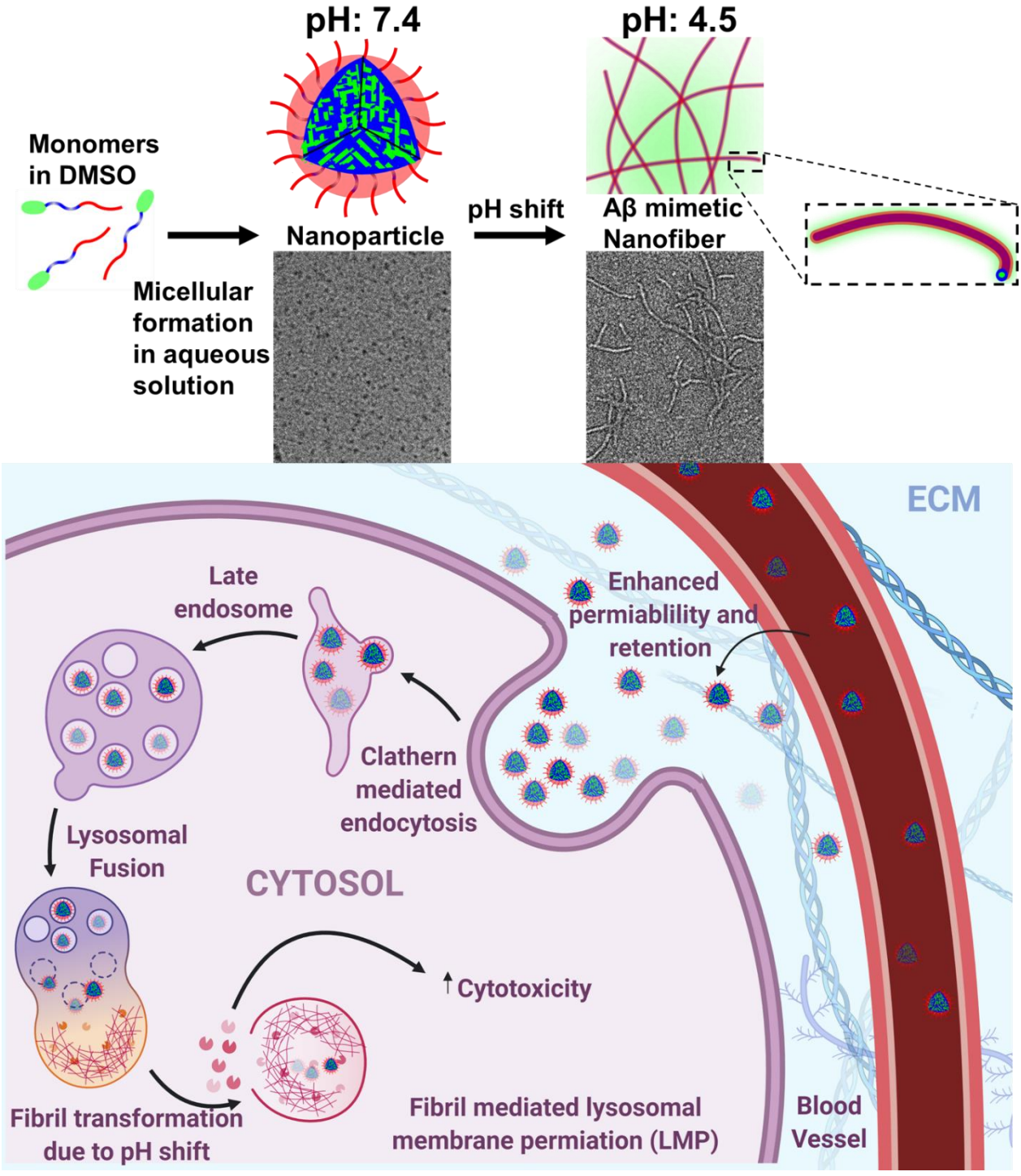

Figure 1. Schematic of CPTNP action *in vitro* and *in vivo*. Nanomaterials are made by first dissolving peptide amphiphiles in DMSO at high concentration, and then rapidly

diluted in pH7.4 aqueous buffer to create nanoparticles. The pH may then be reduced to induce the formation of high aspect ratio nanofibers. Peptide nanoparticles may be incubated with cells or injected IV, which circulate and preferentially locate to the tumor sites via the EPR effect. These nanoparticles are taken up by cancer cells and trafficked to the lysosome via CME. The Lysosomal pH shift induces nanofibril formation and lysosomal membrane permeation, thereby releasing the lysosomal contents into the cytoplasm and inducing LMP mediated cell death and cisplatin sensitization.

2.2. Methods

Peptide synthesis:

Peptide monomers were synthesized via solid-phase peptide synthesis using standard fluorenylmethyloxycarbonyl (Fmoc) chemistry and Ethyl cyano(hydroxyimino)acetate (Oxyma)/1,3-Diisopropylcarbodiimide (DIC) coupling as described in previous publications.[30] Rink amide MBHA resin (loading 0.503 mmol/g, P3 BioSystems, Louisville, KY) was used as solid support. A 6-fold molar excess of Fmoc-protected amino acids to resin was used for coupling. The reaction was monitored with ninhydrin test. The Fmoc group was de-protected with 20% 4-methylpiperidine in N,N-dimethylformamide (DMF) (first 5 min, then 15 min). After the last cycle of amino acids coupling and Fmoc-deprotection, the linear biotinylated peptide was cleaved with a trifluoroacetic acid (TFA) cocktail containing 90% TFA, 5% thioanisole, and 5% H_2O. The liquid was collected and precipitated in cold -20ºC diethyl ether and subsequently

washed 3 times. The powder was re-dissolved in small amount of 50% ACN/water and analyzed by reversed-phase high performance liquid chromatography (RP-HPLC) on a preparative Vydac C18 column. The purity was determined to be >95%. The identities of peptides were confirmed Matrix-Assisted Laser Desorption/Ionization-Time of Flight (MALDI-TOF) and ^{1}H Nuclear Magnetic Resonance (NMR) using a 400 MHz Bruker spectrometer, with samples prepared in *d_6*-DMSO. CPTNP-FF (**Figure 2, A**): ^{1}H NMR (400 MHz, DMSO-*d_6*) δ 8.44 – 8.08 (m, 18H), 8.00 (s, 7H), 7.89 (s, 6H), 7.74 (s, 4H), 7.69 (s, 2H), 7.61 (s, 3H), 7.51 (s, 1H), 7.48 – 6.70 (m, 48H), 4.61 (s, 1H), 4.48 (s, 2H), 4.38 – 3.94 (m, 23H), 3.51 (s, 12H), 2.99 (s, 3H), 2.89 (s, 2H), 2.83 – 2.61 (m, 10H), 2.42 – 1.82 (m, 12H), 1.40 – 1.29 (m, 7H), 1.23 (s, 9H), 1.15 (t, J = 6.9 Hz, 2H), 1.10 (d, J = 2.3 Hz, 2H), 0.85 (d, J = 14.2 Hz, 17H); (**Figure S2).** HRMS (MALDI-TOF) m/z: $[M+H]^+$ Calc'd for $C_{135}H_{191}N_{41}O_{18}H$ 2675.53; Found 2675.649, (**Figure S1**). CPTNP-GG (**Figure 2, B**): ^{1}H NMR (400 MHz, DMSO) δ 8.39 (dd, *J* = 14.7, 7.6 Hz, 4H), 8.33 – 8.22 (m, 8H), 8.18 (s, 1H), 8.16 (s, 3H), 8.15 – 8.09 (m, 6H), 8.09 – 7.94 (m, 9H), 7.93 – 7.73 (m, 8H), 7.70 (s, 2H), 7.64 (s, 2H), 7.51 (s, 1H), 7.21 (s, 44H), 4.22 (s, 13H), 4.11 (s, 4H), 3.87 – 3.68 (m, 9H), 3.51 (s, 9H), 2.99 (s, 2H), 2.89 (s, 2H), 2.73 (d, *J* = 17.5 Hz, 5H), 2.16 (p, *J* = 7.3 Hz, 3H), 2.03 – 1.92 (m, 3H), 1.38 (s, 5H), 1.23 (s, 12H), 1.17 – 1.13 (m, 3H), 1.11 (d, *J* = 2.3 Hz, 1H), 0.91 – 0.74 (m, 20H).HRMS (MALDI-TOF) m/z: $[M+H]^+$ Calc'd for $C_{121}H_{179}N_{41}O_{18}H$ 2495.44; Found 2495.960, (**Figure S1**).

Nano-formulation:

Peptide powder was dissolved in DMSO at concentration 20mM and allowed to sonicate for approximately one hour or until all solids were dissolved and the solution was clear, similar to our other publications.[21,23] To form nanoparticles, DMSO

solubilized monomers were rapidly pipetted into PBS (or a phosphate-citrate) solution buffered at pH 7.4. The solution is then vigorously vortexed for 30 seconds. To form nanofibers, the nanoparticle solution is diluted into an acidic phosphate-citrate buffer solution to achieve a final pH < 5.0.

Characterization of Nanomaterials:

The size distribution of nanoparticles was carried out via dynamic light scattering instrument (DLS, Nano ZS, Malvern) at 25 ºC. The concentrations of the nanoparticles were 40µM for DLS measurements. Transmission Electron Microscopy (TEM, Philips CM-120) samples were prepared by dipping a copper grid into a 40µM solution of nanomaterials. Grids were allowed to dry at room temperature, and morphology was observed. Absorbance and fluorescence spectra were measured on a microplate reader (SpectraMax M3, USA).

In Vitro studies:

All cells were cultured in DMEM (Thermo Fisher: 11960044) with 10% FBS and penicillin/streptomycin, except for HPAepic cells, which were cultured similarly with the addition of 1X Insulin-Transferrin-Selenium (ITS, Thermo Fisher: 41400045). All cells were procured from American Type Culture Collection (ATCC) with the exception of HPAepic, which were procured from ScienCell.

To evaluate the *in vitro* cytotoxicity of CPTNPS, nanomaterial was incubated with various cancer cell lines for 72 h and analyzed by 3-(4,5-dimethylthiazol-2-yl)-5-(3-carboxymethoxyphenyl)-2-(4-sulfophenyl)-2H-tetrazolium) (MTS) assay.

All microscopy was carried out on a Zeiss LSM 800 confocal microscope unless otherwise specified. Image quantification was performed using ImageJ. For all studies, at least five images were quantified per well with at least 40 cells per well. The five images were averaged (1 replicate), and at least three wells were averaged. Statistics were analyzed via GraphPad Prism 6.0. For FITC dextran assays, the protocol from Aits *et al.*, January 2015, with little modification, was followed.[31] For Galectin Puncta assays, the protocol outlined in Aits *et al.*, August 2015, was used.[32] In this case, the galectin-1 antibody from Abcam (ab25138) was used with secondary Goat anti-Rabbit IgG, Alexa Flour 568 procured from Thermo Fisher (A11011). Lysotracker red (Ex/Em:577/590nm) and green (Ex/Em:504/511nm) were procured from Thermo Fisher (Catalog number: L7528 and L7526, respectively). Texas Red labeled cisplatin (TR-Cisplatin, Ex/Em: 568/603nm) was procured from Ursa Biosciences. To detect Cisplatin DNA adducts, a rat Anti-cisplatin monoclonal antibody was procured from Sigma-Aldrich (MABE416). Anti-clathrin. For Annexin V/PI flow cytometry, the Dead Cell Apoptosis Kit from Thermo Fischer (V13241) was used. Flow cytometry was performed on a desktop Guava easyCyte. For Caspase 3 western blot, the anti-caspase three antibody from Abcam was used (ab4051).

In Vivo studies:

Nude mice, 4~5 weeks of age, were ordered from the Jackson Laboratory (Sacramento, CA). All animal procedures were performed under the requirements of institutional guidelines and according to protocol No.19724 approved by the Use and Care of Animals Committee at the University of California, Davis. A549 cells in PBS and Matrigel suspension (1:1 vol/vol) were injected subcutaneously into the right flank of

nude mice. The tumor sizes for all nude mice were monitored and recorded at least bi-weekly. Tumors reaching the dimensions of >100 mm^3 were used for biodistribution and treatment study.

Athymic mice bearing A549 NSCLC xenografts were used for the *in vivo* therapeutic studies (n=3/group). Nanomaterials and PBS were injected via tail vein, three doses, every other day. Tumor volume and body weight were measured several times per week. Once the humane endpoint was reached, tumor volume greater than 2000 $mm^{3,}$ the mice were sacrificed, and blood was harvested for evaluation.

Blood was additionally harvested one day after the cessation of treatment via submandibular collection. Briefly, while holding the mouse via a firm scruff hold, a single-use lancet was used to puncture the submandibular vein. Blood was dropped into a small test tube coated with heparin to prevent clotting of the blood, and the complete blood count was conducted using a Heska HemaTrue system.

Cryosection:

Tissues were harvested from mice and washed in ice-cold phosphate-buffered saline (PBS). Once washed, the tissues are immersed in 4% paraformaldehyde for 16hr or overnight. The tissues are then submerged in 30% sucrose in PBS solution for 24 hours. The tissue is then placed in a block mold and submerged in optimal cutting temperature (OCT) solution (Thermo Fisher 23-730-571). The tissue may then be cut into 10 µm thick slices and fixed onto poly-L-lysine coted slides. The tissue slices are allowed to thaw and dry at room temperature for 15 minutes, after which time they are washed in PBS 3 times, five minutes each wash. The samples may then be stained with

Hoecesht 3332232 for 15 minutes. Subsequently, the tissues are washed three times in PBS, for five minutes each, with a final wash in ultrapure water. 10 µL of 70% glycerol solution is then deposited onto the slide, and a coverslip is mounted and sealed with clear nail polish. The sample is allowed to dry and is imaged on a Zeiss LSM 800.

Statistical analysis:

All data were analyzed using Graphpad Prism 6.0 software. All results were presented as mean ± standard deviation unless otherwise noted. Comparisons between two groups were analyzed with an unpaired student's T-test. In the case of multiple comparisons, the Analysis of Variance test was used with with post hoc Tukey test as appropriate, $P < 0.05$ were considered statistically significant. IC_{50} values were generated using Graphpad Prism's curve fitting feature.

2.3. Results and Discussion

Characterization of peptide nanomaterials

Two peptide amphiphiles, containing all *D*-amino acids, BP-k-f-f-v-l-k-$(r)_8$ (CPTNP-FF, fibril competent) and BP-k-G-G-v-l-k-$(r)_8$ (CPTNP-GG, fibril incompetent negative control) were synthesized on Rink-amide resin via standard Fmoc-based peptide chemistry (**Figure 2, A, B**).

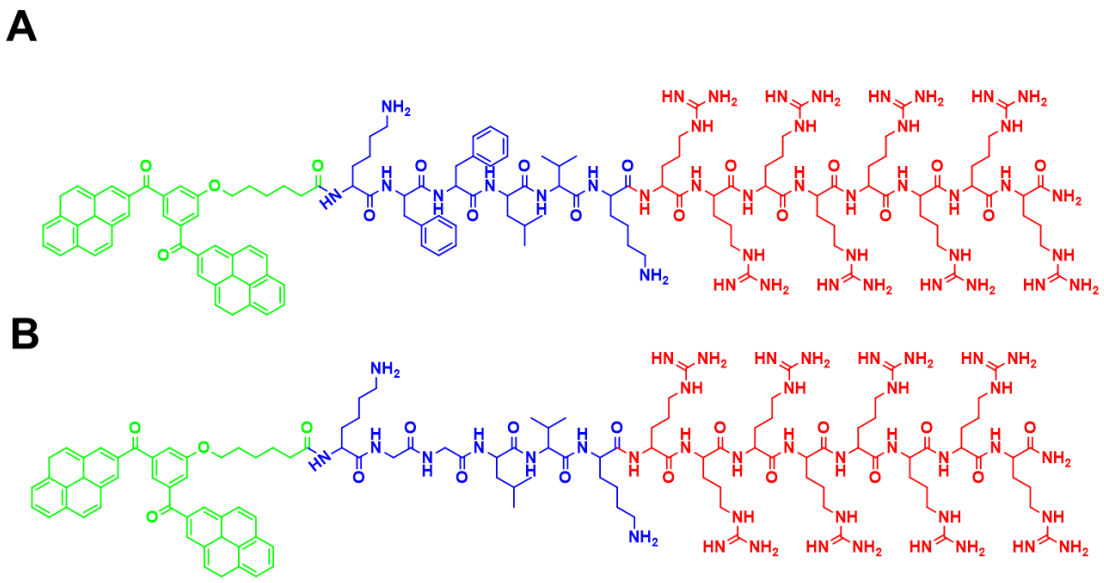

Figure 2. **A**. Chemical structure of CPTNPs (BP-k-f-f-v-l-k-$(r)_8$) wherein green depicts bis-pyrene; blue depicts ß-sheet forming motif; red depicts cell-penetrating peptide. **B**. Negative control GG-CPTNP (BP-k-G-G-v-l-k-$(r)_8$) is similar to A except that the Phe-Phe motif was replaced with the Gly-Gly motif.

D-amino acids were used to increase proteolytic stability in the lysosome and blood plasma. This strategy is effective as the majority of proteolytic enzymes are selective for peptide bonds formed by L-amino acids.[33] Synthesized peptides were cleaved from resins with 95% TFA, 2.5% H_2O, and 2.5% triisopropylsilane for 16 hours. The identity of the peptide product was verified by MALDI-TOF (**Figure 3A**) and ^1H NMR (**Figure 3B**).

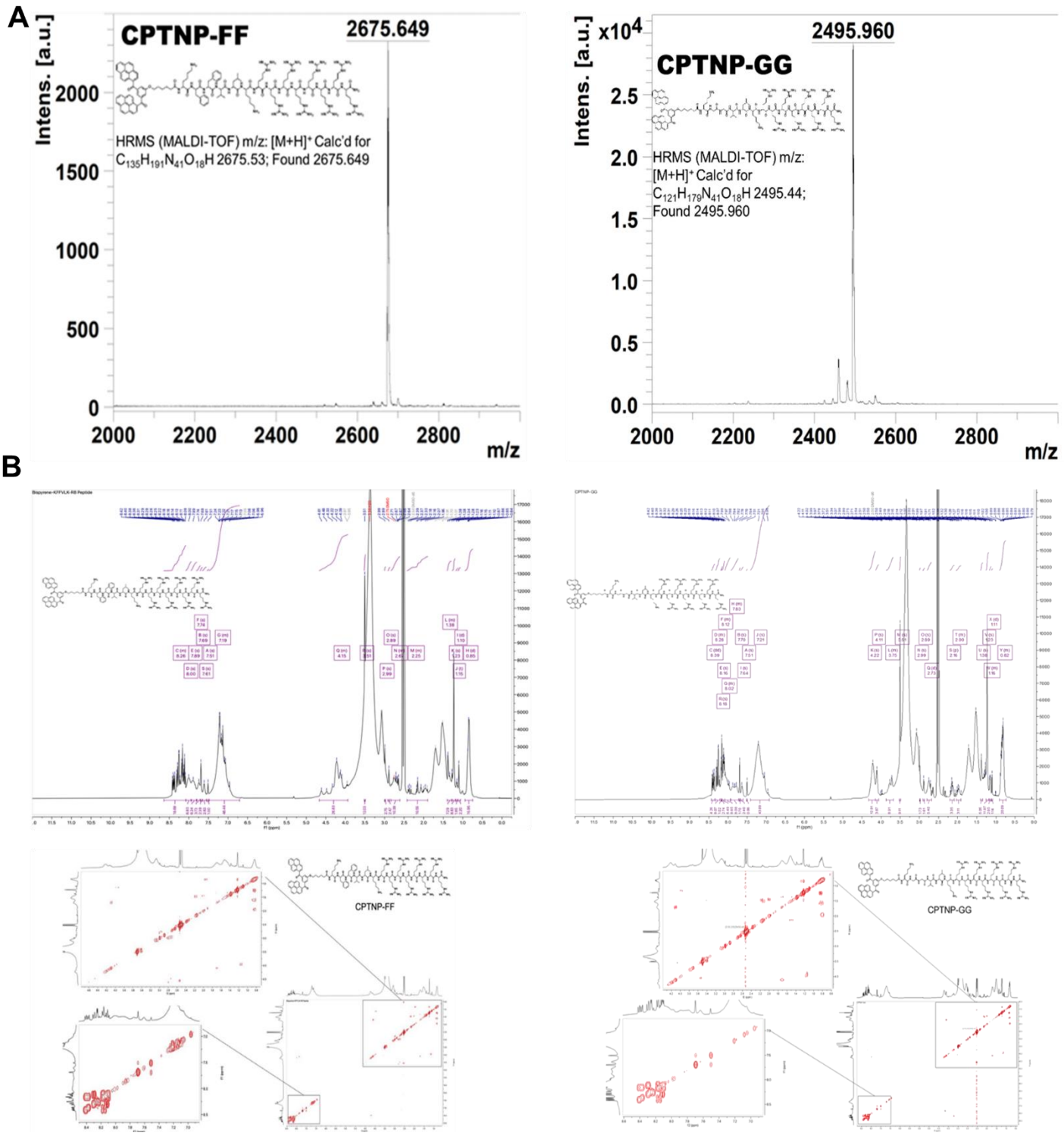
A
CPTNP-FF
2675.649
Intens. [a.u.]
HRMS (MALDI-TOF) m/z: [M+H]+ Calc'd for
C135H191N41O18H 2675.53; Found 2675.649
m/z
x10^4
2495.960
CPTNP-GG
HRMS (MALDI-TOF) m/z:
[M+H]+ Calc'd for
C121H179N41O18H 2495.44;
Found 2495.960
B
CPTNP-FF
CPTNP-GG

Figure 3: **A:** Mass spectra as acquired by MALDI-TOF using α-Cyano-4-hydroxycinnamic acid (CTA) matrix. **B:** 1H NMR and COSY of peptide CPTNP-FF (Left) and CPTNP-GG (Right)

To observe peptide amphiphile self-assembly, we first dissolved peptide in DMSO at a concentration of 20 mM. To form nanoparticles, DMSO-peptide solution was pipetted into ultra-pure water, phosphate-buffered saline or other pH balanced aqueous solution and quickly vortexed for 30 seconds at the appropriate concentration. To form nanofibrils, an acidic buffer was added to pre-formed nanoparticles in an aqueous solution. Nanoparticles remain stable at as low as pH 5.5. Using the above method, we formed peptide nanoparticles and nanofibrils at a 40 μM concentration and measured the particle size via dynamic light scattering (**Figure 4, A**). Importantly, bis-pyrene is an aggregation-induced emission enhanced (AIEE) dye. Because of the AIEE effect, the fluorescence of the CPTNP monomer in DMSO is notably blue-shifted when compared to the nanomaterial formulation, as shown in **Figure 4, B**.

To demonstrate the pH mediated nanoparticle-nanofiber transformation, DLS measurements were taken at pH 7.4 and pH 4.0. At pH 7.4, the size of CPTNPs was determined to be 15.35 nm at 27 °C, with a poly-dispersity index of 0.194. When the pH was adjusted to 4.0, a secondary peak was detected at 170 nm and a tertiary peak in the μm range, a characteristic DLS signal shift which indicates nanofibril formation as seen previously in Yang et al.[34] It can be noted here that while the fibril competent

particles show a substantial shift in the DLS signal indicative of fibril formation, none was seen with the fibril incompetent CPTNP-GG negative control nanoparticle, confirming that FF domain is critical for fibril formation.

The surface charge of CPTNPs was measured using a Malvern Zetasizer. While fibril incompetent CPTNP-GGs exhibited a zeta potential of 13 mV at both pH 7.4 and 4.0. CPTNP-FFs demonstrated a zeta potential of ~13mV at pH 7.4, but the zeta potential was modulated to 26 mV when exposed to a pH of 4.0. This may be due to a shift in exposed arginine groups on the nanomaterial surface. (**Figure 4, C**)

The critical micelle concentration (CMC) of CPTNP-FFs was calculated to be 0.63μM using the Nile red method.[35] Nile red fluorescence is increased nearly 20 fold in the presence of the hydrophobic core of micellular nanomaterials and may thereby be used to determine the concentration at which nanomaterials are formed. Here, we observed the fluorescence of Nile red (Ex/Em: 485/636nm) on a Spectra Max, M3 plate reader in serially diluted concentrations of CPTNP-FF. We then curve fit the data using Prism's sigmoidal curve fitting function (R^2 =0.9928) and utilized the second derivative method to determine the CMC (**Figure 4, D**). This data suggests CPTNPs have excellent stability.

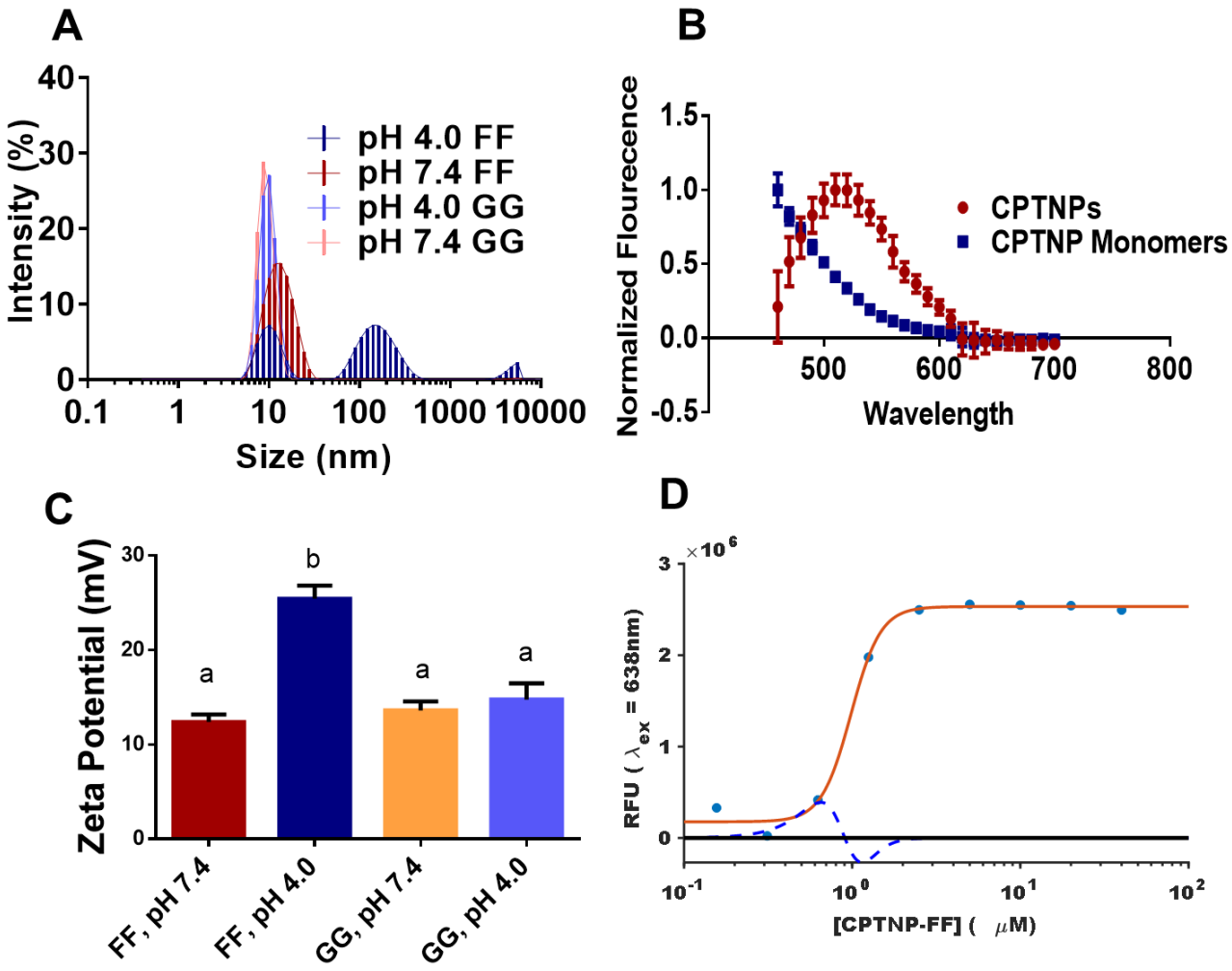

Figure 4: A. Particle sizes of CPTNPs (FF) and GG-CPTNPs (GG) under various pH, as determined by DLS. **B.** Zeta potential of FF- and GG-CPTNPs measured at 50 µM. (a:b, p< 0.0005) **C.** Critical micelle concentration as calculated via Nile red fluorescence using the second derivative method. The red line indicates a curve fitted to the fluorescence at 638nm excitation, where the blue line is the second derivative of the red curve. CMC = 0.63µM D. Fluorescence of CPTNP monomer in DMSO was found to shift to red when CPTNP nanoparticles were formulated in PBS due to the AIEE effect of BP

Transmission electron microscopy validated that nanofiber was formed when the acidity of the aqueous solution was increased to pH 4.0. The *D*-Phe-*D*-Phe dipeptide motif appeared to be critical for nanofibril formation, as when substituted with a Gly-Gly motif, nanofibrils were not observed, as expected (**Figure 5**).

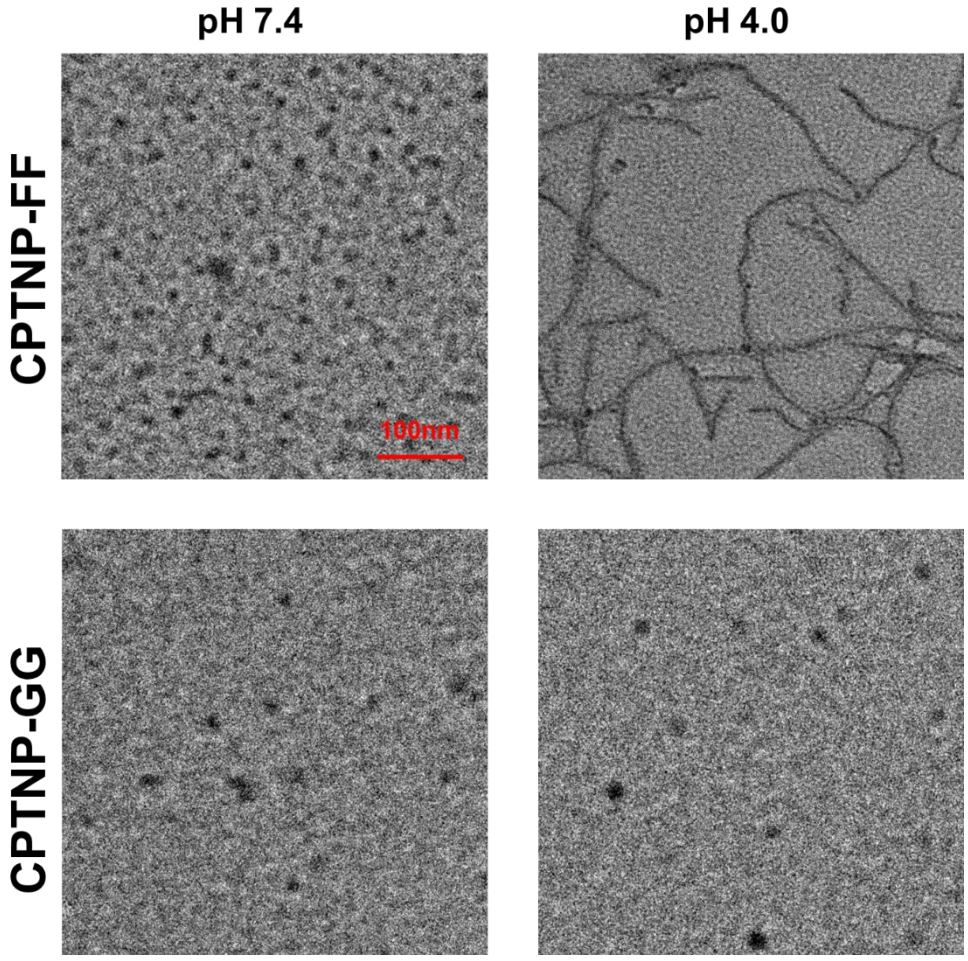

Figure 5: TEM images of CPTNPs incubated at pH7.4 and 4.0. Scale bar is 100 nm in each image.

Cellular localization of CPTNPs and mechanism of uptake

We suspected that CPTNP nanomaterials would localize into the lysosome as other poly-arg conjugates have been known to do so.[27,28] So, to determine the intracellular localization of CPTNPs, A549 cells were incubated with both CPTNP and LysoTracker Red DND-99, a dye which, when protonated by an acidic environment, becomes membrane-impermeable and is thereby trapped in the acidic lysosome. It was found that CPTNP-FF and CPTNP-GG colocalized with LysoTracker Red DND-99, as seen in **Figure 6, A.** An intensity heat map of CPTNP and LysoTracker Red was generated using ImageJ and the Pearson's colocalization coefficient was found to be 0.94 in each case (**Figure 6, B**). To validate that CPTNP-FF was up-taken by the cell, a Z-stack of a single A549 cell was performed. Indeed, BP fluorescence was observed inside the cell, co-localized with the LysoTracker Red signal (**Figure 6, C)**.

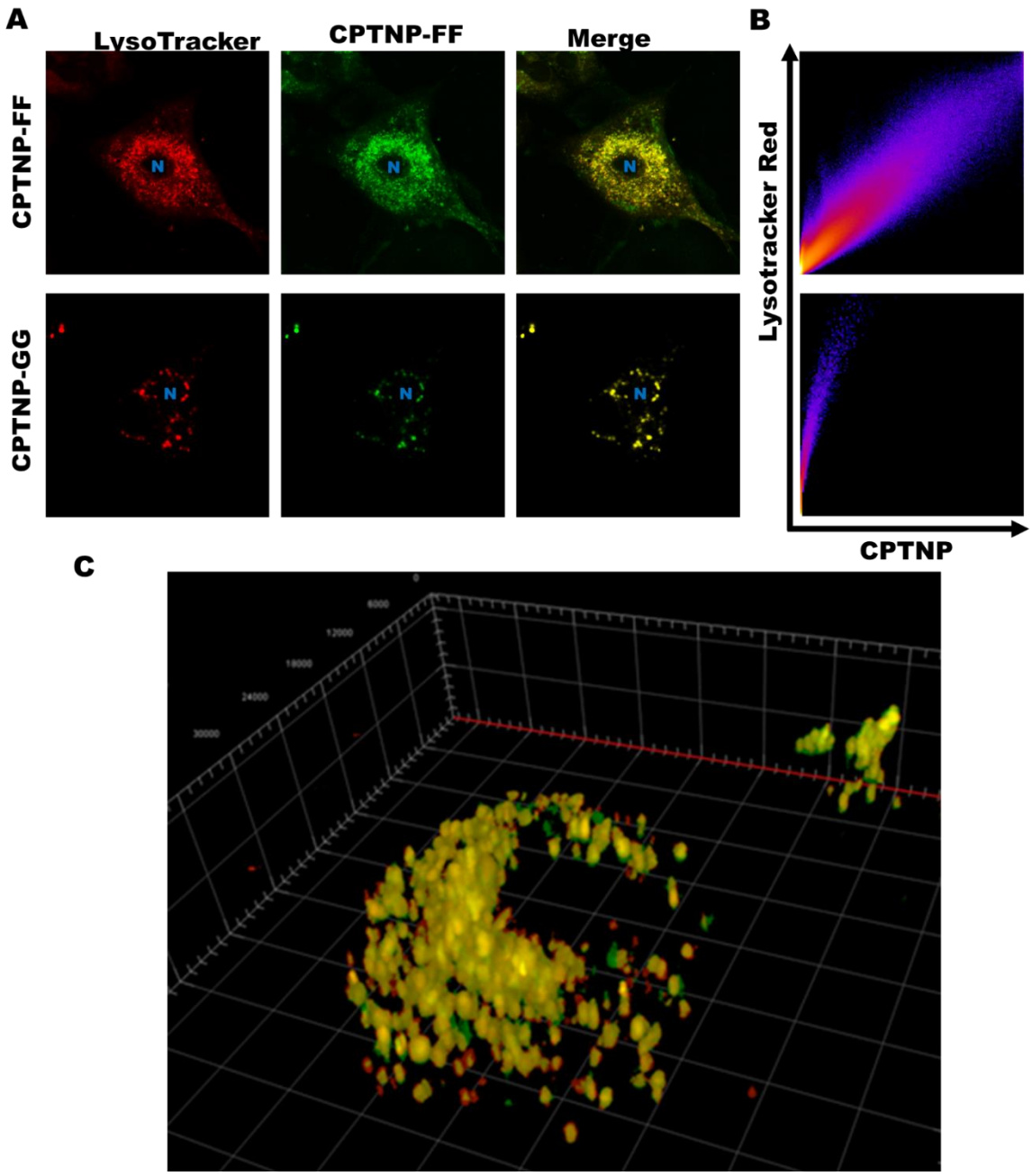

Figure 6. A. Single A549 cell treated with one µM CPTNP-FF and CPTNP-GG stained with 0.75 nM LysoTraker Red DND-99, the nucleolus is represented by a blue N. **B.** Intensity heat map of the pixel intensity distribution of cells imaged after treatment with CPTNP-FF and CPTNP-GG fluorescence and compared via LysoTracker Red fluorescence giving rise to a Pearson's coefficient of 0.94 in each case. **C**. Z stack of a

single A549 cell treated with CPTNP-FF (Green) and LysoTraker Red (Red) rendered in 3D, indicating true uptake in the cell's interior.

Through the course of these uptake studies, an interesting effect was observed whereby after approximately 3 hours of treatment with high concentration CPTNP-FF, the LysoTracker Red signal would rapidly dissipate. To investigate this further, a time-lapse study was conducted using a confocal Zeiss LSM-800 microscope equipped with an incubator system to keep a constant temperature of 37°C, by first treating A549 cells with 75 nM LysoTracker Red DND-99 for 30 mins, and subsequent treatment with 50 µM CPTNP for 1 hr. Cells were then washed and imaged every minute beginning at 2.5 hrs—enough time to allow for the endocytosis of CPTNP-FFs and the initial formation of nanofibers. Here, several punctate LysoTracker Red DND-99 signals were observed to disperse over time rapidly. A single lysosome (red) can be observed to first co-locate with CPTNP (green) then disperse over the course of 30 minutes (**Figure 7, A**). This is indicative of lysosomal disruption and led us to study LMP further, as discussed later in the text.

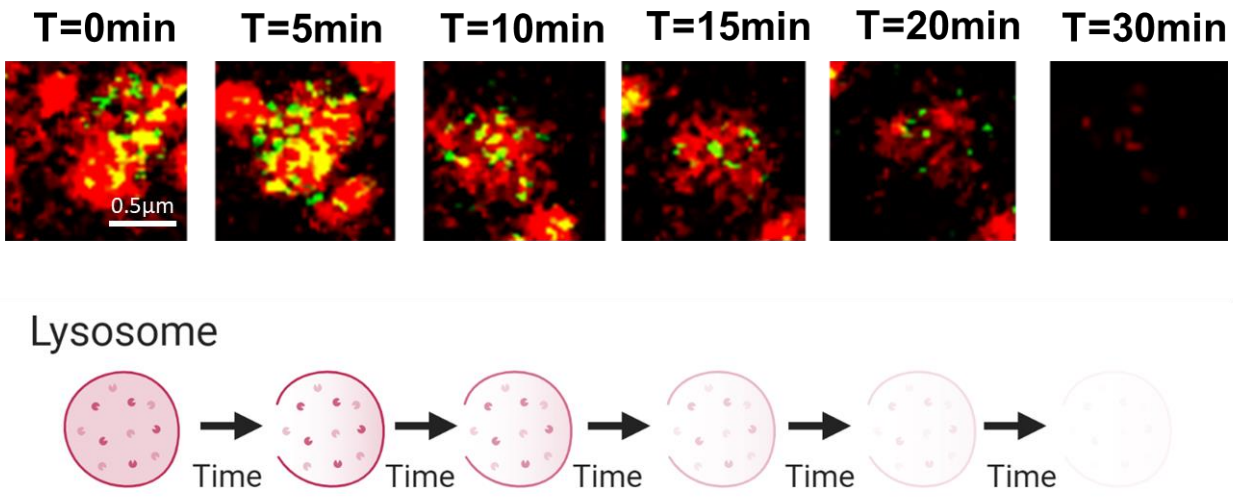

Figure 7: Live-cell confocal image of a single lysosome stained with LysoTraker Red DND-99 and treated with CPTNP with accompanying illustration. Imaging starts at 2.5 hours after removal of 50 µM CPTNP treatment, the characteristic time point at which lysosomal dysfunction was observed. The lysosome can be seen to disperse over the course of 30 minutes. Video of whole cells undergoing this process is shown in the supplementary data.

To observe the effect of CPTNPs on cell viability, CPTNP-FF and CPTNP-GGs, at various concentrations, were incubated with the cells for 72 hours. After incubation, proliferation was measured via MTS assay, and absorbance was measured at 490 nm via plate reader. While no cytotoxicity was observed for CPTNP-GGs, CPTNP-FF was found to be cytotoxic with an IC_{50} of 2.49 µM (**Figure 8**), indicating that nanofibril formation is required for cytotoxicity.

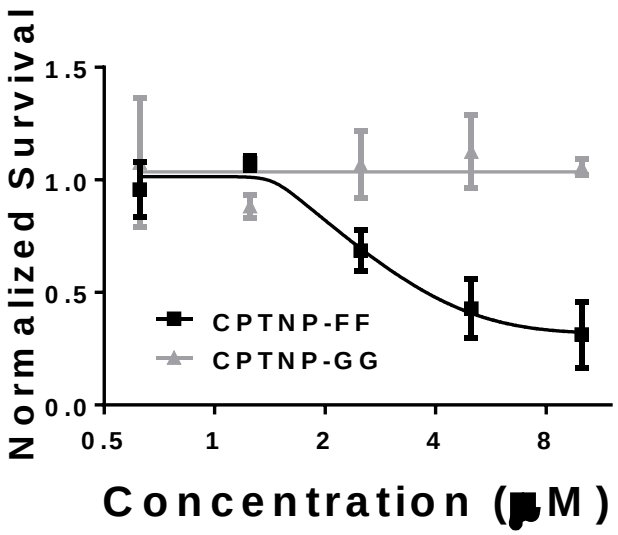

Figure 8: Normalized cytotoxicity of A549 cells after treatment with CPTNP-FF and CPTNP-GG, indicating fibril formation is needed for cell death.

To determine the cytotoxicity of CPTNPs against various cancer cell lines, MTS assays were performed on A549 lung carcinoma cells, A427, H460 non-small cell lung cancer lines, and HPAepic (human primary alveolar cells). The IC_{50} of CPTNP-FF was found to be significantly lower in A549, A427, and H460 cancer cells than the primary HPAepic cells **Figure 9**.

Table 1: IC_{50} of CPTNPs with A549, H460, A427, non-small cell lung cancer liniages alongside HPAepic. Calculation of IC_{50} preformed using the curvefitting function of Prism 6.

Cell Line	IC_{50}:CPTNP-FF (μM)
A549	2.49
H460	9.54
A427	9.96
HPAEPIC	25.37

It has previously been reported that NSCLC cells have upregulated clathrin-mediated endocytosis. We supposed that this effect might account for the differential in cytotoxicity observed. So, to determine the mechanism of CPTNP uptake, A549 cells were incubated with CPTNPs and separately with three different endocytic inhibitors: amiloride, an inhibitor of micropinocytosis; β-cyclodextrin, an inhibitor of caveolae-mediated endocytosis; and hypertonic sucrose, an inhibitor of clathrin-mediated endocytosis (CME). Hypertonic sucrose was found to inhibit the cytotoxic effect of CPTNPs, indicating that CME might be required for CPTNP activity (**Figure 9, A**). Indeed, **Figure 9, B** suggests that clathrin is upregulated in A549 cells when compared to primary HPAepic cells. The importance of CME is reinforced by **Figure 9, C**, which demonstrates that while amiloride and β-cyclodextrin did not inhibit the uptake of

CPTNP-FF, hypertonic sucrose, a CME inhibitor greatly reduces CPTNP in A549 cells. It has previously been reported that clathrin expression is upregulated in NSCLC. Together, this data suggests that upregulated CME may play a major role in CPTNP

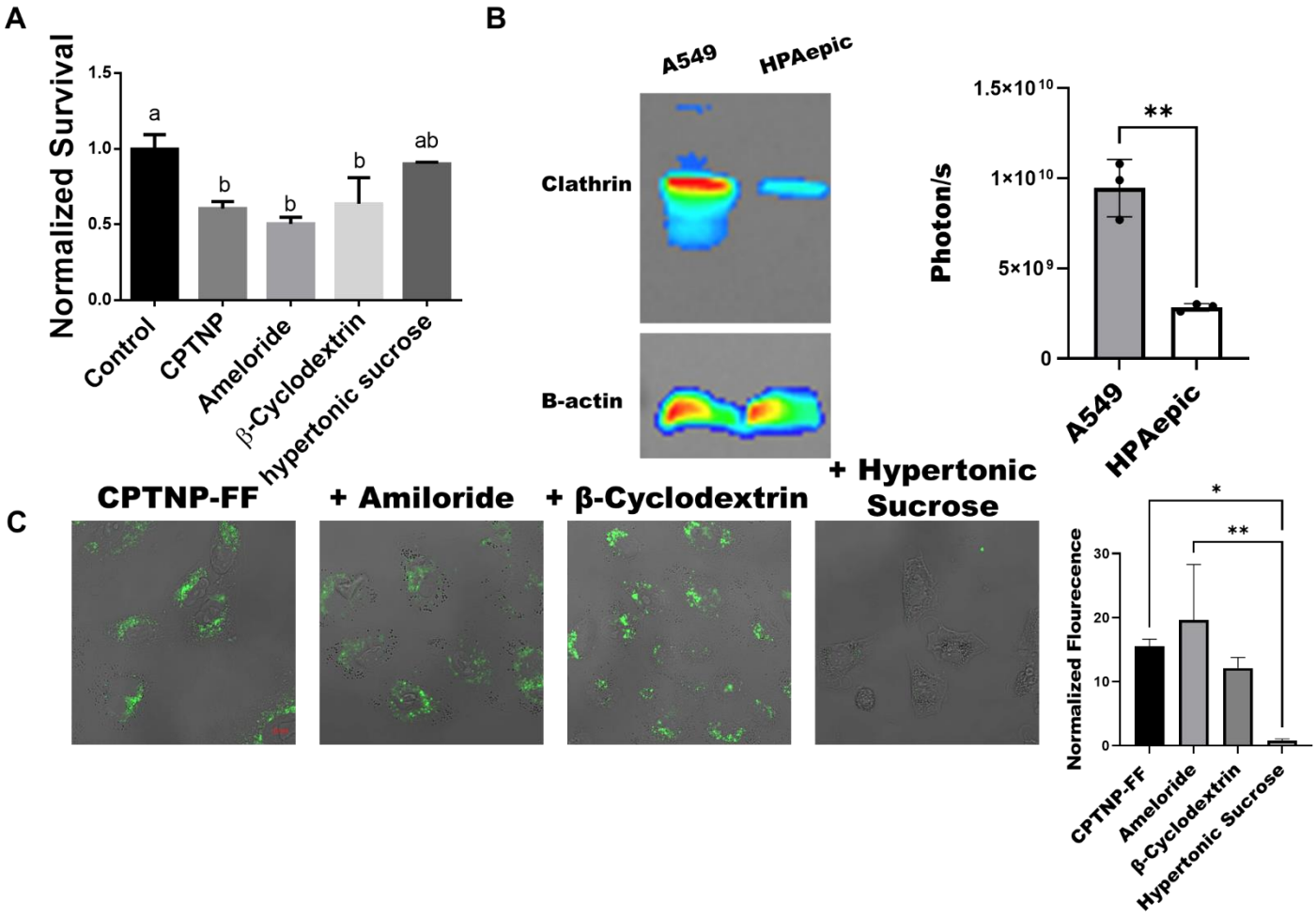

selectivity.

Figure 9: A. Cell survival normalized to control (untreated) as measured by MTS assay; all other samples were treated with five µM CPTNP-FF for 24 hr when combined with three endocytosis inhibitors. Cytotoxicity is inhibited by hypertonic sucrose, an inhibitor of CME. a>b ($p<0.05$), ab>b except for β-cyclodextrin and is not significantly different than a ($p< 0.05$). B. Expression of clathrin in A549 non-small cell lung cancer cells and

HPAepic primary cells. The blot was repeated three times, and luminescence was measured to generate the bar graph to the right. Clathrin can be seen to be over-expressed in A549 cells. C. Confocal scanning laser microscopy of A549 cells treated with CPTNP-FF and various endocytosis inhibitors. Results were quantified, and only hypertonic sucrose was found to be significantly different from CPTNPs alone. These results match the survival data shown in A above.

This may explain the discrepancy in CPTNP uptake and IC_{50} values between the two cell lineages documented in **Table 1** and **Figure 10**. **Figure 10** demonstrates that while CPTNP uptake was readily observed in A549 lung carcinoma cells, much less uptake was measured in primary human pulmonary alveolar epithelial cells (HPAepic). The IC_{50} value of HPAepic cells was found to be much higher than A549 cells (25.23μM vs. 2.49μM), which is further indicative of the role of CME in CPTNP-FF cytotoxicity.

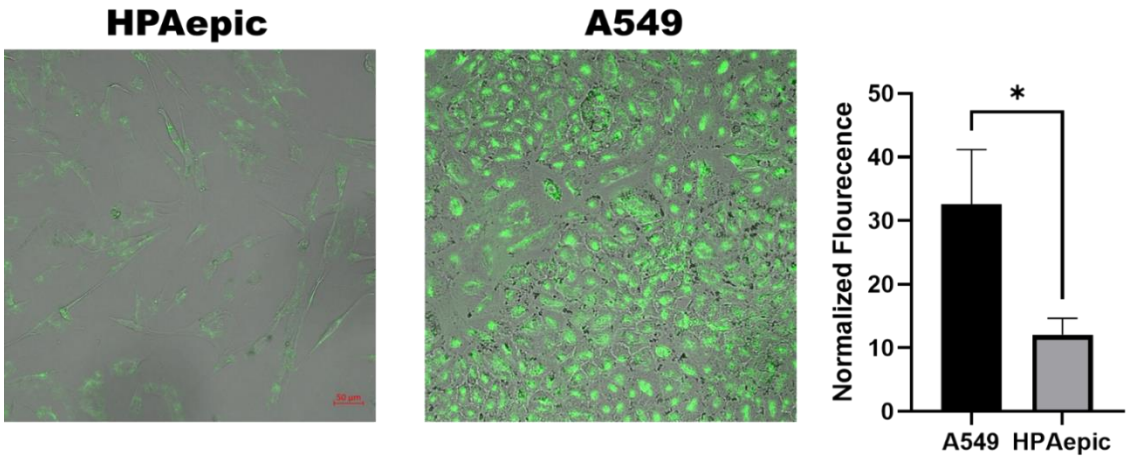

Figure 10: Comparative images of HPAepic primary cells and A549 NSCLC cells. A549 cells have increased fluorescence vs. HPAepic cells. The graph represents the average of 3 wells at 5µM, with a 6hr incubation. The average value of each well was determined by acquiring three images and using ImageJ to segment each cell, then measuring the average fluorescence intensity.

Other factors may play a role in the unequal cytotoxicity, however. Lysosomal

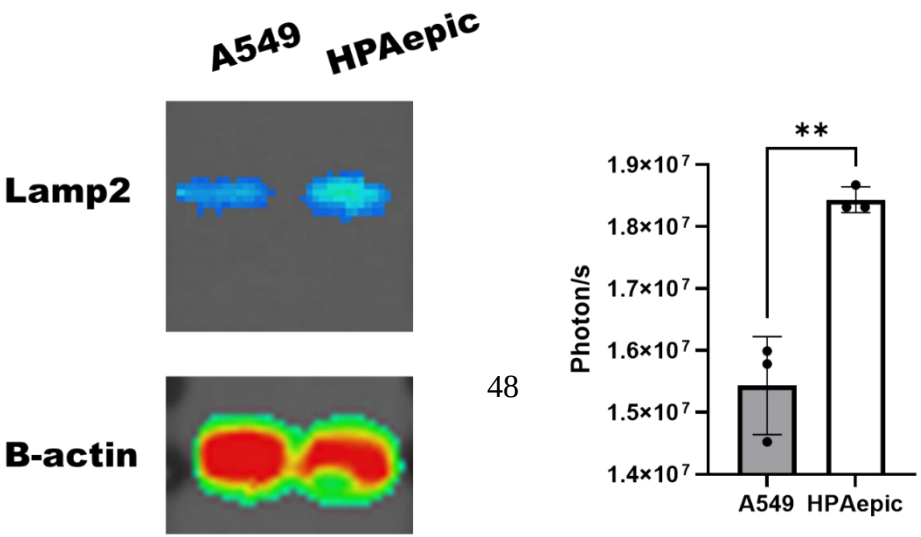

associated membrane protein 2 (LAMP2) was also found to be downregulated in A549 cells vs. HPAepic cells (**Figure 11**). Downregulation of LAMP2 has previously been associated with susceptibility to LMP.[5] More data is needed to find all contributors to CPTNP selectivity.

Figure 11: Representative western blot staining for Lamp2 in untreated A549 non-small cell lung cancer cells and HPAepic cells. The experiment was repeated three times and A549 cells were found to have lower Lamp2 expression. Replicates were compared using a students T test ($p < 0.01$) executed in ImageJ.

CPTNPS induce lysosomal disruption *in vitro* and *in vivo*

The rapid dissipation of the lysotracker signal as seen in **Figure 7** suggested that CPTNPs were inducing lysosomal membrane permeation. To probe the nature of lysosomal disruption, A549 cells were incubated with 200 μg/mL FITC-Dextran (10 kD) for 12 h and subsequently washed and incubated in untreated media for two hour. Next, these pretreated cells were incubated with varying concentrations of CPTNP-FF for four hour. In untreated cells, we expected FITC-Dextran to be endocytosed and sequestered in the lysosome, giving a punctate signal. Should the lysosomal membrane be permeated, FITC signal would escape the lysosome and be cytosolically distributed. Because FITC is self-quenched at high local concentrations and quenched in acidic

environments, an increase in FITC signal may be used to quantify lysosomal leakage, as depicted in **Figure 12, A**.[31] This is reflected in our data which shows CPTNP dose-dependent FITC signal, an indication of LMP (**Figure 12, B**). While the FITC-Dextran assay demonstrates that CPTNP-FF induces LMP, the assay sensitivity is limited. To probe the LMP effect of CPTNP-FFs at lower concentrations (1μM in this case) more sensitive galectin puncta assay, previously reported in the literature, was utilized.[32] Briefly, in untreated cells, galectin-1 is cytosolically distributed. However, when the lysosomal membrane is permeabilized, galectin-1 binds to the glycosylated termini of lysosomal membrane-associated protein-1 (LAMP-1), and upon fixation and antibody staining for galectin-1, reveals a punctate pattern as compared to the uniform cytosolic distribution of galectin-1 in cells with intact lysosomes (**Figure 12, C**). **Figure 12, D** shows punctate galectin-1 in A549 cells treated with one μM CPTNP-FF for 24 hours but not CPTNP-GG (fibril incompetent nanoparticle) or control. Puncta were tabulated by enumerating the number of puncta and number of cells per image with a minimum of 40 cells per image. Five images were taken per well and averaged. Three wells were averaged to arrive at the final value, demonstrating more puncta/cell in the CPTNP-FF case. This indicates that CPTNP-FFs induced LMP in a fibril-dependent manner, at low dosages (1μM) (**Figure 12, D**). To determine the LMP activity of CPTNP-FF *in vivo*, athymic mice bearing A549 flank tumors were treated with either 5 mg/kg CPTNP-FF or PBS. Mice were sacrificed 24 hours later, and tumors were harvested, embedded in paraffin, sectioned, and stained for galectin-1 (**Figure 12, E**). Immunohistochemistry (IHC) revealed a punctate pattern in the treated tumor, but a uniform distribution pattern in the PBS control, indicating LMP was induced *in vivo*.

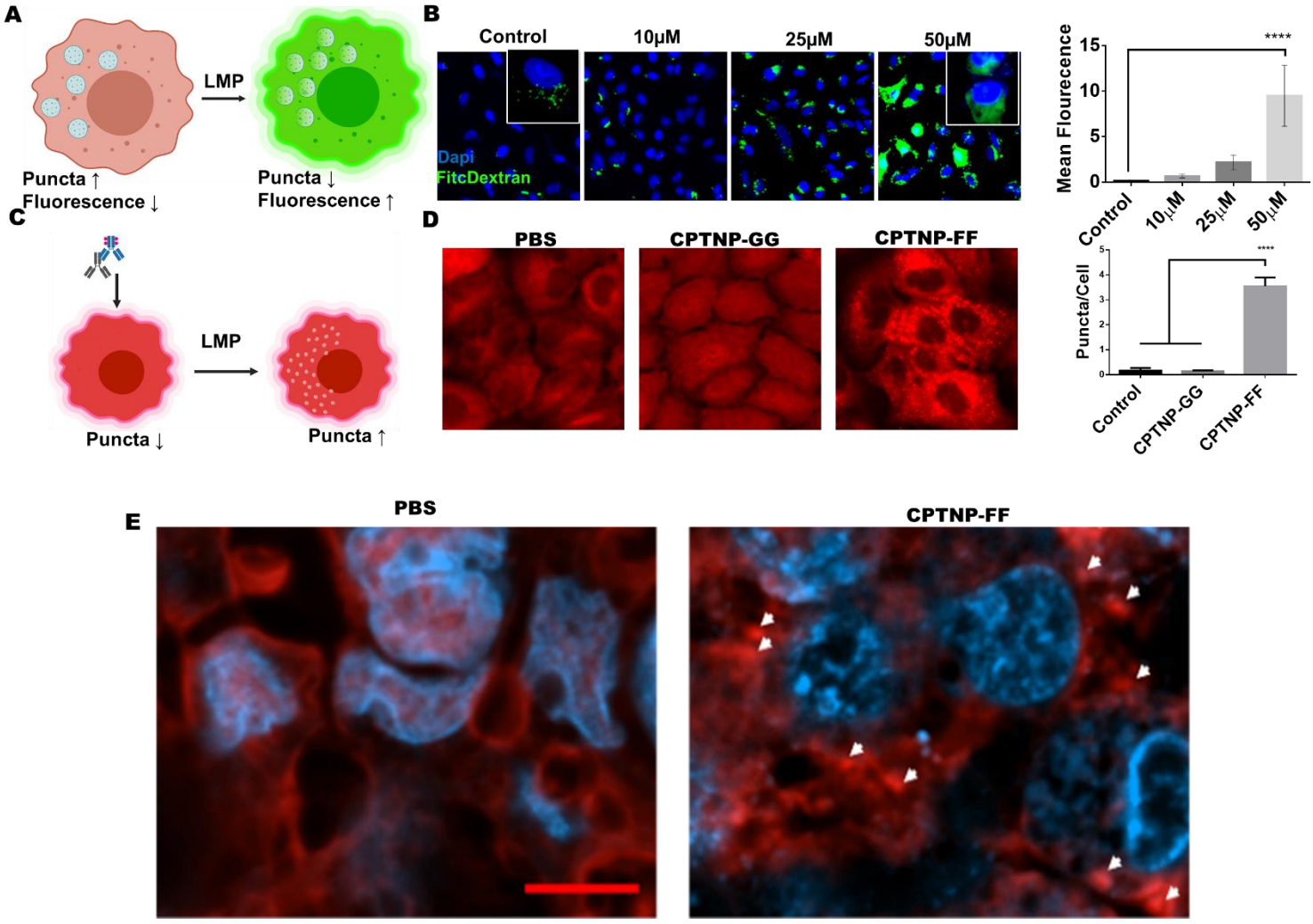

Figure 12. **A**. Depiction of expected results from FITC-dextran assay. Briefly, when cells are incubated with a high concentration 10kDa FITC-dextran, the FITC-dextran is sequestered in the lysosome, where the acidic conditions and high concentration of dye quench the fluorescence of FITC. When subsequently subjected to lysosomal membrane permeation, the punctate pattern is lost, and fluorescence increases. **B.** FITC-dextran assay at varying concentrations, with A549 cells where Green depicts FITC-dextran and blue depicts DAPI. The graph represents the average of 3 wells at

various concentrations. The average value of each well was determined by acquiring five images and using ImageJ to segment each cell, then measuring the average fluorescent intensity. **C**. Illustration of galectin puncta assay where cells may be stained with anti-galectin antibody to reveal either a cytosolic distribution of galectin-1, indicating no LMP or a punctate distribution of galectin-1, indicating LMP was induced. Galectin-1 has an affinity to the glycosylated terminal of lysosome-associated membrane protein 1 (LAMP 1), which is only exposed when the lysosome is permeated, creating the punctate pattern. **D**. Representative image of a galectin-1 puncta assay with DMSO control and treatment with CPTNP-FF and CPTNP-GG at one µM for 24 hr, revealing that lysosomal membrane permeation is fibril dependent. Average puncta/cell was determined by enumerating the number of puncta and number of cells per image with a minimum of 40 cells per image. Five images were taken per well and averaged. Three wells were averaged to arrive at the final value. With accompanying illustration. **E**. Representative images of galectin-1 stained (IHC) tumors 24 hours after treatment with 5 mg/kg CPTNP-FF or PBS. Puncta may be seen in the treated case, highlighted by white arrows Indicating CPTNPs induce LMP in vivo. The scale bar is 5 µm.

To further observe fibril formation *in situ*, transmission electron microscopy was performed. TEM was carried out by treating A549 cells with 10 µM CPTNP for 24 hours, followed by fixation with Karnovsky's fixative for 1 hour and subsequent fixation with 1% osmium tetroxide and 1.5% potassium ferrocyanide in ddH_2O. Samples were dried in

progressively increasing concentrations of ethanol. Resin was allowed to infiltrate the sample for 24 hours and to polymerize. **Figure 13, A**, displays control and CPTNP-FF treated lysosome. Nanofibers may be seen inside of A549 cell lysosomes (labeled with red arrows). The membrane of the lysosome was disrupted, as seen in the lower right quadrant of the image. Additional high magnification TEM images of treated and control lysosomes may be seen in **Figure 13, B**. A wide-field image is shown in **Figure 13, A** below, where many lysosomes with abnormal morphology were seen in the treated case, compared to control. This abnormal morphology is a result of the nanoparticle-to-high aspect nanofiber transformation in the side of the NSCLC lysosome.

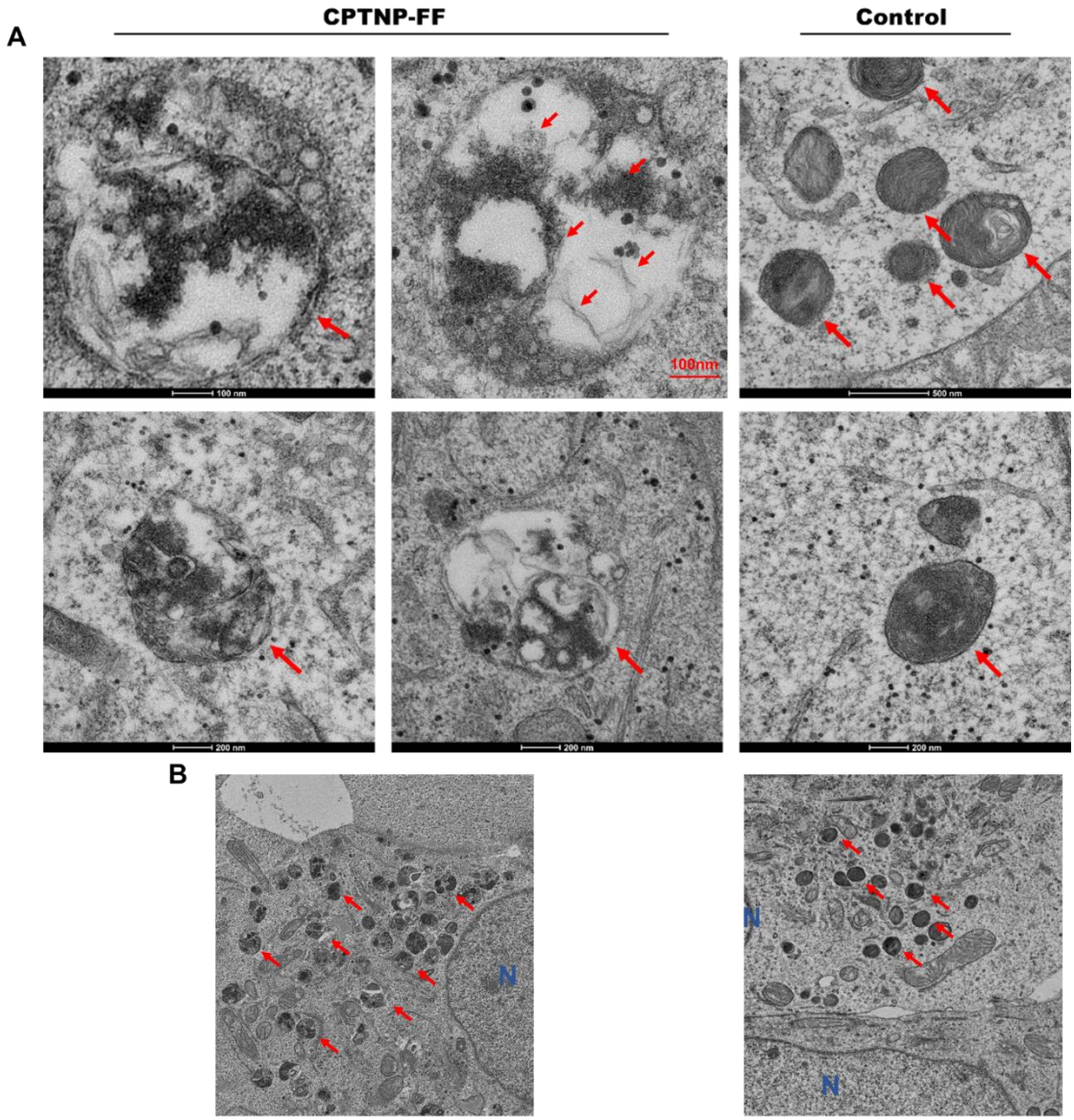

Figure 13: A. Transmission electron micrographs of A549 cells after treatment with 10 µM CPTNP for 24 hrs. Nanofibers are labeled with red arrows. Scale bar is 100 nm in each image. **B**. Low magnification TEM image of the same sample, lysosomes are labeled with red arrows while the nucleolus is labeled with a blue N.

Previous literature has suggested that nanoparticle platforms induce the formation of reactive oxygen species (ROS) at levels corresponding to their hydrodynamic radii, leading to lysosomal dysfunction.[36] A dihydrofluorescein diacetate assay was used to detect ROS formation resulting from CPTNP treatment. Cells were pre-treated with a non-fluorescent FITC precursor, dihydrofluorescein diacetate. When in contact with ROS species, it is modified into the fluorescent FITC. Then cells were treated and placed in a plate reader for continuous monitoring over 12 hours. No increase in fluorescence was observed after treatment with CPTNP-FF, indicating that CPTNP-FFs did not induce LMP by introducing ROS species in the lysosome. Therefore, we suggest CPTNPs did induce LMP via an orthogonal mechanism to previously reported nanomaterials.

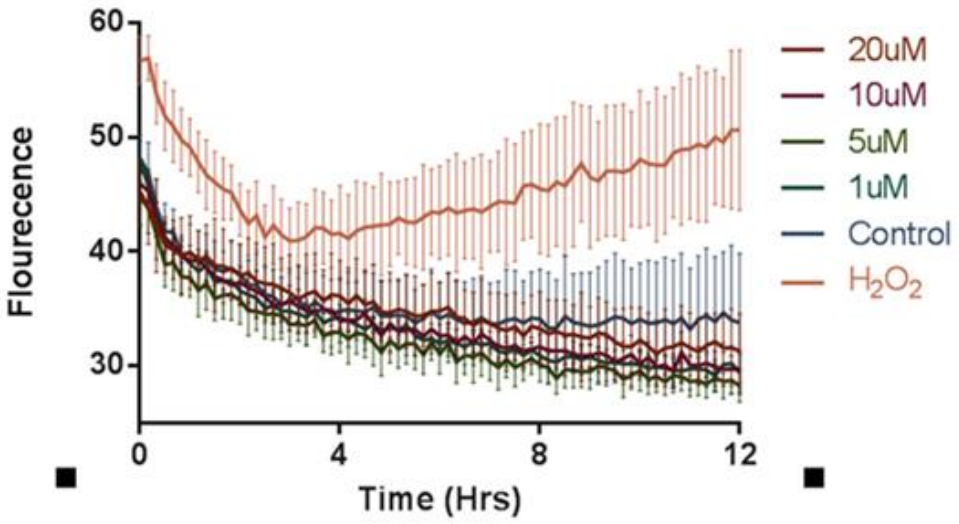

Figure 14: Contribution of Reactive oxygen species (ROS) to LMP. It has previously been reported that nanomaterial endocytosis may lead to ROS-mediated LMP.[37] To

test this theory in our case, we incubated A549 cells with Dichloro-dihydro-fluorescein diacetate (DCFH-DA) for 1 hour before replacing the media with CPTNP at variable concentrations. DCFH-DA is a pro-FITC molecule that fluoresces after exposure to ROS. We observed fluorescence every 10 minutes for 12 hours on a plate reader (temperature: 37ºC) and charted relative fluorescence above as a function of time. Interestingly, CPTNP treated cells had no signal increase, indicating that ROS plays no significant role in lysosome rupture.

Due to the LMP action of CPTNP-FFs, we suspected that CPTNPs might induce non-apoptotic cell death mechanisms. To validate this hypothesis, we performed an annexin V/PI assay using a desktop flow cytometer. The results indicate an increase in PI+ cells when treated with CPTNP-FF but not Annexin V+ cells (**Figure 15**). This suggests that CPTNPs kill cells by inducing necrotic cell death. To further validate this conclusion, we again treated cells with CPTNP and obtained lysate from treated and untreated cells. We then stained for active caspase 3; no active caspase was observed, which reinforces our conclusion that CPTNP-FF induces non-apoptotic cell death.

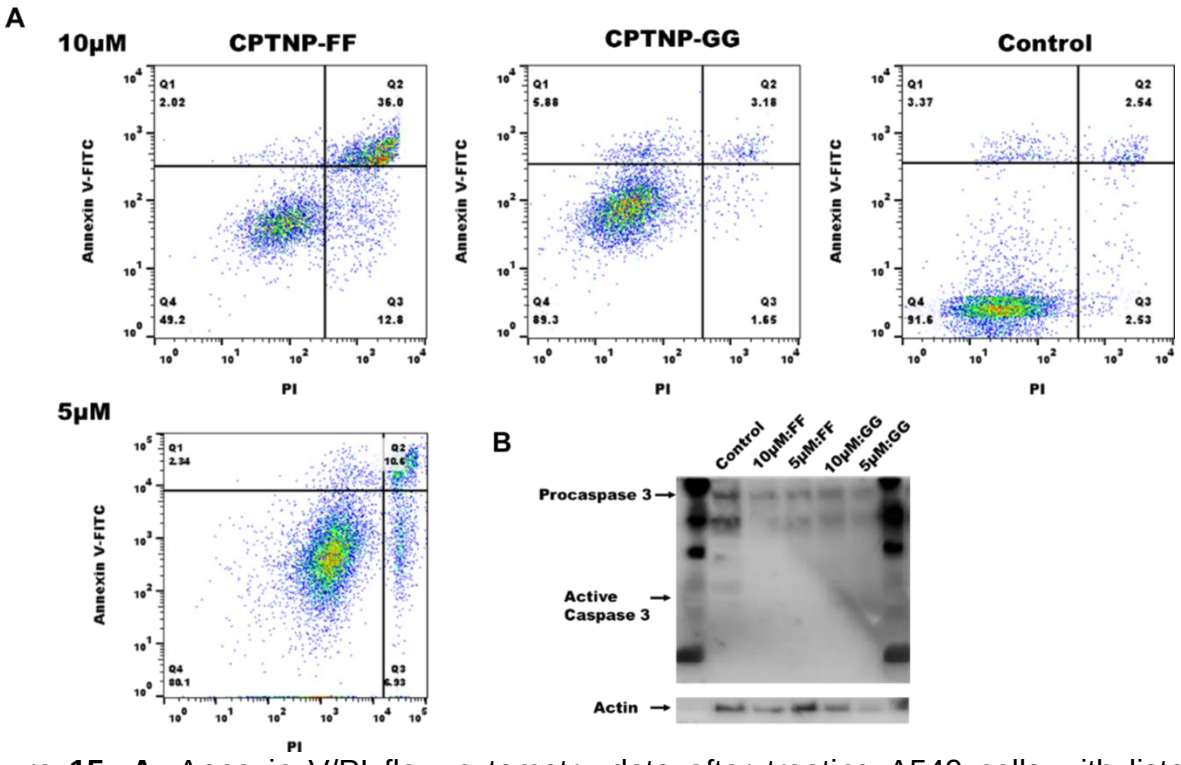

Figure 15: A. Annexin V/PI flow cytometry data after treating A549 cells with listed concentrations of material for 12 hours. FITC fluorescence was increased due to BP background in the cells. In the 5 and 10 uM CPTNP-FF case an increase in necrotic cells may be seen but not apoptotic cells. This suggests that CPTNP-FF induces necrosis. **B**. Western blot staining for pro and active caspase 3 after treatment with CPTNPs. No active caspase 3 was detected indicative of non-apoptotic cell death.

In vivo tumor response and localization

To determine the *in vivo* anti-tumor effect and to measure any toxicity of CPTNPs, six athymic mice were injected subcutaneously with 12 × 10^6 A549 NSCLC

cells in the right flank. When tumor burden reached 100 mm^3 the mice were separated into two groups: CPTNP-FF (2mg/kg) and PBS control. Three doses of each treatment were administered every other day for six days. Mice were monitored tri-weekly for four weeks. Tumor volume was monitored via digital caliper (**Figure 16, A**). Tumor growth in mice treated with CPTNP-FF was significantly slower, compared to PBS treated group. Bodyweight was monitored on an electronic scale. Some reduction in weight was observed in CPTNP-FF vs. PBS. 24hrs after the cessation of treatment, blood was collected from the submandibular vein, and a complete blood count was conducted on a Heska HemaTrue blood analyzer. No significant differences were observed between the CPTNP and PBS treated groups, indicating limited toxicity **(Figure 16, C).**

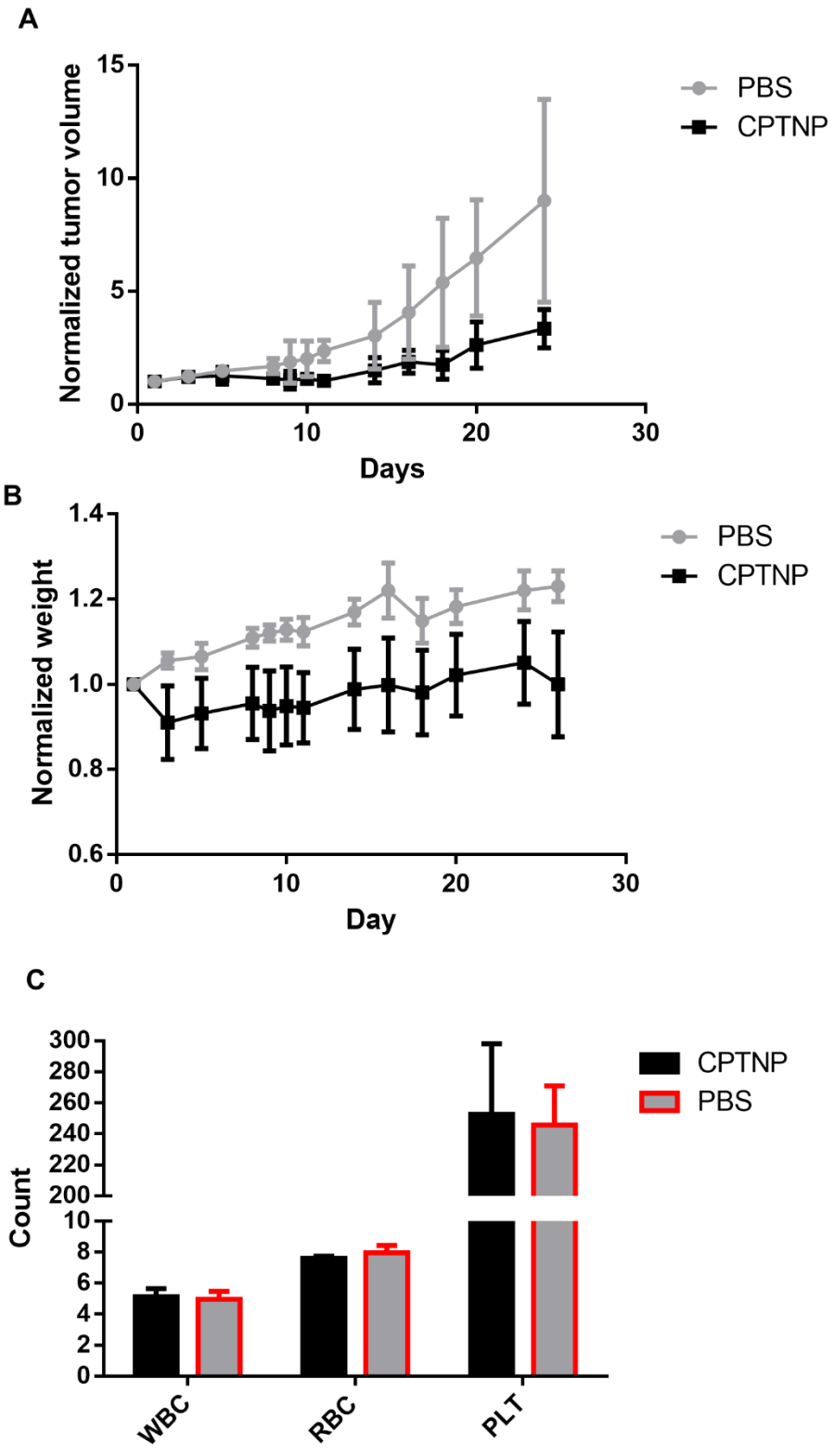

Figure 16: A. tumor volume of three mice per treatment group, treated with three doses of 5 mg/kg CPTNP and PBS via tail injection. Mouse tumor size was measured along

two dimensions using a digital caliper. **B.** Normalized weight of the same mice measured every other day via digital scale. Some weight loss was observed in the treated case. **C.** complete blood count of mice one day after the final treatment. Blood extracted via submandibular collection. No significant differences in blood count were observed between groups. Units: WBC, $10^3/mm^3$: RBC, $10^6/mm^3$: PLT, $10^3/mm^3$

To study CPTNP-FF biodistribution and uptake of CPTNPs *in vivo* we injected one mouse with 5 mg/kg nanomaterial and a second mouse with equal volume PBS. Indeed, bis-pyrene fluorescence was observed to be higher in the tumor site than in other tissues (**Figure 17, A, B**). This is consistent with earlier results, indicating A549 cell preferential uptake. Enhanced permeability and retention, which suggests nanomaterials preferentially locate to the tumor site due to leaky tumor vasculature, may also be an essential factor.

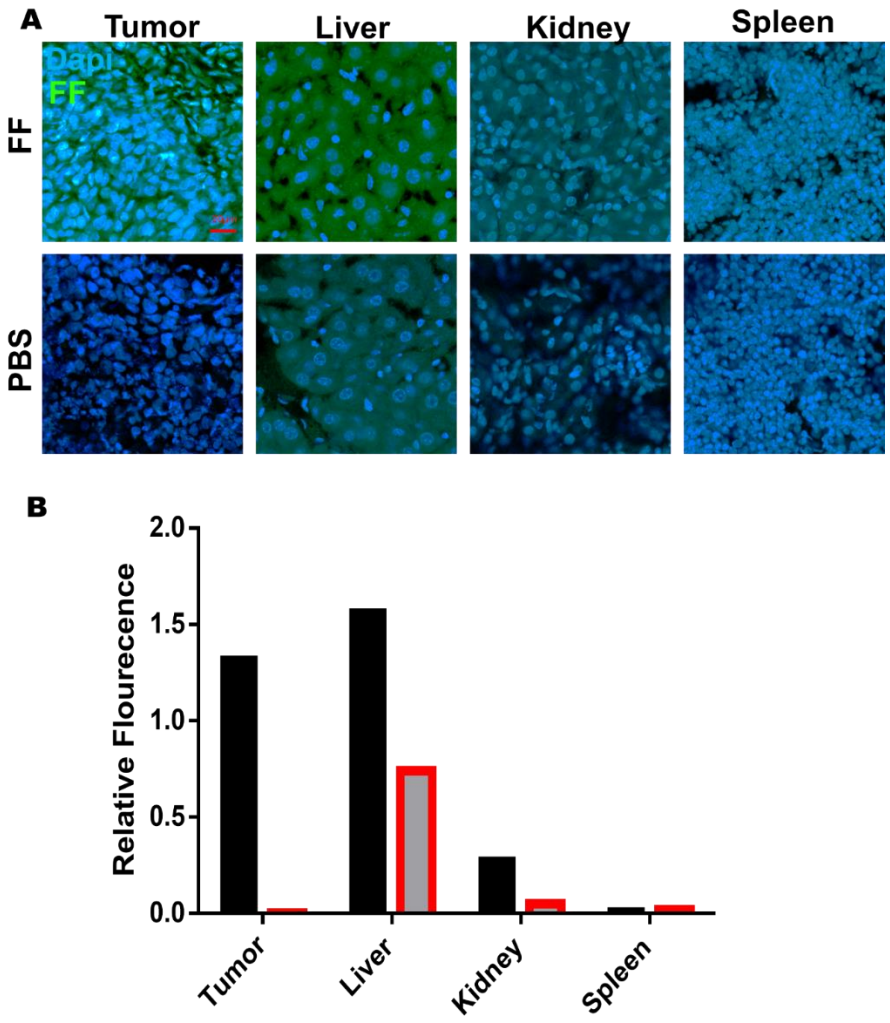

Figure 17: **A**. Confocal scanning laser microscopy of in vivo tissue samples 24hrs after treatment with 5 mg/kg. CPTNP-FF or PBS-Control. Tissues were cryosectioned. Tumor sections were found to have high uptake of CPTNP. **B.** Relative fluorescence of comparative samples indicating tumor localization of CPTNPs.

Given the high liver uptake of CPTNP, we were interested to see if we could decern any morphological changes in the liver indicative of fibril-induced damage. To

access this we performed a series of hemoxylin and eosin stains on the tumor, liver, spleen and kidney, common organs for nanomaterial uptake. No difference in liver morphology could be observed; however, tumor cell death was readily detectable. (**Figure 18**)

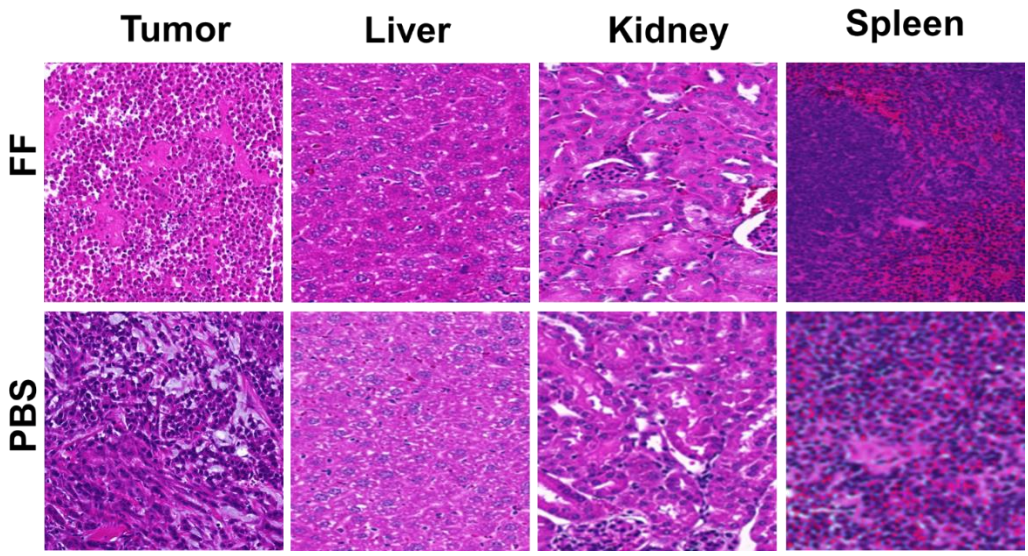

Figure 18: H & E micrographs of critical organs after treatment with CPTNP or PBS.

2.4. Conclusion

In the above study, we developed cell-penetrating transformable peptide nanomaterials (CPTNPs). We show that these CPTNPs are endocytosed via clathrin-mediated endocytosis, where they then localize in the lysosome. Once in the lysosome, these materials are triggered by the lysosomal acidic pH and transform into high aspect ratio nanofibrils. These nanomaterials then rupture the lysosomal membrane in a fibril-

dependent manner. The induced lysosomal membrane permeabilization can then cause the necrosis of non-small cell lung cancer cells at low micromolar concentrations. In a xenograft model of CPTNPs were shown to affect tumor burden. While some weight loss was observed, the complete blood count remained stable after treatment, and H&E staining did not reveal liver damage, despite some accumulation. CPTNPs are the first example of molecular self-assembly used as a lysosomal permeating agent and cisplatin sensitizer. In the future, modifications to this nanoplatform can be developed, which improve biodistribution and tumor targeting via the incorporation of stealth peptides and targeting ligands, and chemotherapeutic loading. Such modification will minimize uptake by the liver and other organs and increase tumor uptake, thereby increasing the potency of CPTNPs. In addition, platinum conjugated CPTNPs can be developed for co-delivery of cisplatin with enhanced synergistic effect, such that a lower dose of CPTNP will be needed. We believe CPTNP will evolve into an effective intra-cellular molecular self-assembly therapeutic nanoplatform that will have an impact on the future treatment of NSCLC.

2.5. References

1. Perera, R. M. & Zoncu, R. The Lysosome as a Regulatory Hub. *Annu. Rev. Cell Dev. Biol.* **32**, 223–253 (2016).
2. Serrano-Puebla, A. & Boya, P. Lysosomal membrane permeabilization as a cell death mechanism in cancer cells. *Biochem. Soc. Trans.* **46**, 207–215 (2018).
3. Dielschneider, R. F., Henson, E. S. & Gibson, S. B. Lysosomes as Oxidative Targets for Cancer Therapy. *Oxid. Med. Cell. Longev.* **2017**, 3749157 (2017).
4. Piao, S. & Amaravadi, R. K. Targeting the lysosome in cancer. *Ann. N. Y. Acad. Sci.* **1371**, 45–54 (2016).
5. Kallunki, T., Olsen, O. D. & Jäättelä, M. Cancer-associated lysosomal changes: friends or foes? *Oncogene* **32**, 1995–2004 (2013).
6. Safaei, R. *et al.* Abnormal lysosomal trafficking and enhanced exosomal export of cisplatin in drug-resistant human ovarian carcinoma cells. *Mol. Cancer Ther.* **4**, 1595–1604 (2005).
7. Chi, C. *et al.* Disruption of lysosome function promotes tumor growth and metastasis in Drosophila. *J. Biol. Chem.* **285**, 21817–21823 (2010).
8. Nilsson, C., Roberg, K., Grafström, R. C. & Öllinger, K. Intrinsic differences in cisplatin sensitivity of head and neck cancer cell lines: Correlation to lysosomal pH. *Head Neck* **32**, 1185–1194 (2010).
9. Dielschneider, R. F., Henson, E. S. & Gibson, S. B. Lysosomes as Oxidative Targets for Cancer Therapy. *Oxid. Med. Cell. Longev.* **2017**, 3749157 (2017).

10. Rowson-Hodel, A. R. *et al.* Hexamethylene amiloride engages a novel reactive oxygen species-and lysosome-dependent programmed necrotic mechanism to selectively target breast cancer cells. *Cancer Lett.* **375**, 62–72 (2016).
11. Mai, T. T. *et al.* Salinomycin kills cancer stem cells by sequestering iron in lysosomes. *Nat. Chem.* **9**, 1025–1033 (2017).
12. LeGendre, O., Breslin, P. A. & Foster, D. A. (-)-Oleocanthal rapidly and selectively induces cancer cell death via lysosomal membrane permeabilization. *Mol. Cell. Oncol.* **2**, e1006077 (2015).
13. Park, D. & Lee, Y. Biphasic Activity of Chloroquine in Human Colorectal Cancer Cells. *Dev. Reprod.* **18**, 225–231 (2014).
14. Circu, M. *et al.* Modulating lysosomal function through lysosome membrane permeabilization or autophagy suppression restores sensitivity to cisplatin in refractory non-small-cell lung cancer cells. *PLoS ONE* **12**, (2017).
15. Raj, E. N., Lin, Y.-W., Chen, C.-H., Liu, K.-K. & Chao, J.-I. Selective Autophagy Pathway of Nanoparticles and Nanodrugs: Drug Delivery and Pathophysiological Effects. *Adv. Ther.* **3**, 2000085 (2020).
16. Feng, Z. *et al.* Enzymatic Assemblies Disrupt the Membrane and Target Endoplasmic Reticulum for Selective Cancer Cell Death. *J. Am. Chem. Soc.* **140**, 9566–9573 (2018).
17. Yang, P.-P. *et al.* Host Materials Transformable in Tumor Microenvironment for Homing Theranostics. *Adv. Mater.* **29**, 1605869 (2017).
18. Gao, Y., Shi, J., Yuan, D. & Xu, B. Imaging enzyme-triggered self-assembly of small molecules inside live cells. *Nat. Commun.* **3**, 1033 (2012).

19. Yang, Z. M., Xu, K. M., Guo, Z. F., Guo, Z. H. & Xu, B. Intracellular Enzymatic Formation of Nanofibers Results in Hydrogelation and Regulated Cell Death. *Adv. Mater.* **19**, 3152–3156 (2007).
20. Jeena, M. T. *et al.* Mitochondria localization induced self-assembly of peptide amphiphiles for cellular dysfunction. *Nat. Commun.* **8**, 26 (2017).
21. Zhang, L. *et al.* Tumor Receptor-Mediated In Vivo Modulation of the Morphology, Phototherapeutic Properties, and Pharmacokinetics of Smart Nanomaterials. *ACS Nano* **15**, 468–479 (2021).
22. Luo, S. *et al.* Targeting self-assembly peptide for inhibiting breast tumor progression and metastasis. *Biomaterials* **249**, 120055 (2020).
23. Zhang, L. *et al.* Transformable peptide nanoparticles arrest HER2 signalling and cause cancer cell death in vivo. *Nat. Nanotechnol.* **15**, 145–153 (2020).
24. Wang, D. *et al.* pH-Responsive Self-Assemblies from the Designed Folic Acid-Modified Peptide Drug for Dual-Targeting Delivery. *Langmuir* **37**, 339–347 (2021).
25. Feng, Z., Wang, H., Chen, X. & Xu, B. Self-Assembling Ability Determines the Activity of Enzyme-Instructed Self-Assembly for Inhibiting Cancer Cells. *J. Am. Chem. Soc.* **139**, 15377–15384 (2017).
26. Giraldo, A. M. V., Appelqvist, H., Ederth, T. & Öllinger, K. Lysosomotropic agents: impact on lysosomal membrane permeabilization and cell death. *Biochem. Soc. Trans.* **42**, 1460–1464 (2014).
27. Fuchs, S. M. & Raines, R. T. Pathway for Polyarginine Entry into Mammalian Cells †. *Biochemistry* **43**, 2438–2444 (2004).

28. Gross, A. *et al.* Vesicular disruption of lysosomal targeting organometallic polyarginine bioconjugates. *Metallomics* **7**, 371–384 (2015).
29. Nir, S. *et al.* Tailoring the self-assembly of a tripeptide for the formation of antimicrobial surfaces. *Nanoscale* **11**, 8752–8759 (2019).
30. Yang, F. *et al.* One-bead one-compound combinatorial library derived targeting ligands for detection and treatment of oral squamous cancer. *Oncotarget* **10**, 5468–5479 (2019).
31. Aits, S., Jäättelä, M. & Nylandsted, J. Chapter 13 - Methods for the quantification of lysosomal membrane permeabilization: A hallmark of lysosomal cell death. in *Methods in Cell Biology* (eds. Platt, F. & Platt, N.) vol. 126 261–285 (Academic Press, 2015).
32. Aits, S. *et al.* Sensitive detection of lysosomal membrane permeabilization by lysosomal galectin puncta assay. *Autophagy* **11**, 1408–1424 (2015).
33. Van Breemen, R. B. & Davis, R. G. Rates of peptide proteolysis measured using liquid chromatography and continuous-flow fast atom bombardment mass spectrometry. *Anal. Chem.* **64**, 2233–2237 (1992).
34. Yang, P.-P. *et al.* Host Materials Transformable in Tumor Microenvironment for Homing Theranostics. *Adv. Mater.* **29**, 1605869 (2017).
35. M. Peterson, A., Tan, Z., M. Kimbrough, E. & M. Heemstra, J. 3,3′-Dioctadecyloxacarbocyanine perchlorate (DiO) as a fluorogenic probe for measurement of critical micelle concentration. *Anal. Methods* **7**, 6877–6882 (2015).
36. Sabella, S. *et al.* A general mechanism for intracellular toxicity of metal-containing nanoparticles. *Nanoscale* **6**, 7052–7061 (2014).

3. Cell Penetrating Transformable Peptide Nanoparticles Induce Cisplatin Sensitization

3.1. Introduction

Lung cancer accounts for the plurality of cancer instances and deaths both in the US and abroad.[1] Despite the advent of immune checkpoint blockade and other targeted therapies, platinum-based chemotherapy is still the most common therapeutic regimen for patients with stage II to stage IV non-small cell lung cancer (NSCLC).[2] Unfortunately, high-dose cisplatin therapy is poorly tolerated and only moderately improves the 5-year survival rate of patients.[3] As such, there is a need for novel therapeutics which synergize with traditional cytotoxic chemotherapies; thus, allowing for the use of lower chemotherapeutic doses and a reduction in adverse side effects.

Cisplatin plays an essential role in the management of NSCLC and other cancer types such as testicular, ovarian, head and neck, bladder, lung, cervical cancer, melanoma, lymphomas.[4] Cisplatin induces cancer cell apoptosis by crosslinking purine bases and creating DNA lesions.[5] However, two significant challenges to modern platinum-based chemotherapy are toxic off-target effects and cisplatin resistance, thereby limiting the efficacy of the therapy. Lysosomal sequestration of cisplatin plays a major role in resistance in some cancer types.[6,7]

Indeed other lysosomal inhibitors are known to synergize with Cisplatin via the inhibition of autophagy.[8] Hydroxychloroquine, an anti-malarial drug and potent inhibitor of autophagy, has been extensively studied in the clinic for its synergism with various chemotherapies.[9,10] However, at least one clinical trial has failed due to the dosing

limitations of the combinatorial treatment.[11] This may be because while hydroxychloroquine increases the efficacy of chemotherapies in the tumor space, it can also increase the toxicity in chemotherapeutic sensitive organs like the kidney via similar mechanisms.[12] Nanomaterials offer a promising solution to this challenge as kidney uptake may be readily controlled by nanomaterial size, shape, and surface chemistry.[13]

We previously determined that CPTNPs are capable of disrupting the lysosome of non-small cell lung cancer cells.[14] The lysosome plays an essential role in autophagy as it is the final stop on the pathway to degradation of the autophagic substrates.[15] We, therefore, reasoned that as CPTNPs disrupt a crucial organelle involved in autophagy, CPTNPs may inhibit autophagy. If true, CPTNPs could play a role similar to drugs like hydroxychloroquine while utilizing a unique mechanism. We, therefore, explored the capacity for CPTNPs to inhibit autophagy by developing NSCLC cell lines stably expressing an autophagic flux probe.[16] We further developed a protocol that would allow us to measure autophagic flux in vivo in real-time utilizing a murine optical coherence tomography and scanning laser ophthalmoscope system[17] and xenografts of the NSCLC cell lines expressing the autophagic flux probe. This system demonstrated that autophagic flux might not play a significant role in the *in vivo* CPTNP therapeutic effect. However, the system proved to be highly useful as an in vivo autophagy monitoring tool.

In the previous chapter, we discussed the development of transformable amyloid mimetic peptide amphiphiles for lysosomal disruption in non-small cell lung cancer. This regime led to the reduction of tumor burden in vivo with some toxicity. It has been reported in the literature that cisplatin-based chemotherapeutics are sequestered in the

lysosome of cancer cells and thus inhibited from activity in their active site, nuclear DNA.[18] We hypothesized that the induction of lysosomal membrane permeabilization via CPTNPs would lead to increased nuclear concentration of chemotherapeutics like cisplatin and, therefore, cytotoxicity and tumor regression. We further hypothesized that the combination of cisplatin and nanomaterial could allow for lower doses of both therapeutics, thereby lowering the toxicity of both treatments when combined. This was the case in our in vivo studies which showed very little toxicity with low dose cisplatin and nanomaterial alongside good tumor response.

Finally, given the findings regarding cisplatin sensitization and off-target material localization observed previously[14], we determined to develop an improved version of CPTNPs. This updated version would be loaded with oxaliplatin. The updated CPTNP would be crosslinked to reduce liver uptake and improve circulation. Finally, the updated material would have reduced surface charge, as high surface charge has been linked to increased liver uptake. [19]

Here we will demonstrate the synergistic effects of cell-penetrating transformable peptide nanoparticles in conjuncture with Cisplatin. Moreover, we will illustrate the mechanism of cisplatin sensitization. We will also explain the combinatorial effect of Cisplatin and CPTNP therapy in vivo. We will demonstrate the effect of CPTNP therapy on autophagic flux both in vitro and in vivo, utilizing the eyepod system in combination with an internally controlled autophagic flux probe.[16,17] Finally, we will demonstrate the activity of crosslinked, Cisplatin-loaded CPTNP 2.0s in vitro.

3.2. Methods

Peptide synthesis:

Peptide monomers were synthesized via solid-phase peptide synthesis using standard fluorenylmethyloxycarbonyl (Fmoc) chemistry and Ethyl cyano(hydroxyimino)acetate (Oxyma)/1,3-Diisopropylcarbodiimide (DIC) coupling as described in previous publications.[20] Rink amide MBHA resin (loading 0.503 mmol/g, P3 BioSystems, Louisville, KY) was used as solid support. A 6-fold molar excess of Fmoc-protected amino acids to resin was used for coupling. The reaction was monitored with ninhydrin test. The Fmoc group was de-protected with 20% 4-methylpiperidine in N,N-dimethylformamide (DMF) (first 5 min, then 15 min). After the last cycle of amino acids coupling and Fmoc-deprotection, the linear biotinylated peptide was cleaved with a trifluoroacetic acid (TFA) cocktail containing 90% TFA, 5% thioanisole, and 5% H_2O. The liquid was collected and precipitated in cold (-20ºC) diethyl ether and subsequently washed 3 times. The powder was re-dissolved in small amount of 50% ACN/water and analyzed by reversed-phase high performance liquid chromatography (RP-HPLC) on a preparative Vydac C18 column. The purity was determined to be >95%. The identities of peptides were confirmed Matrix-Assisted Laser Desorption/Ionization-Time of Flight (MALDI-TOF) and ^{1}H Nuclear Magnetic Resonance (NMR) using a 400 MHz Bruker spectrometer, with samples prepared in d_6-DMSO. CPTNP-FF (**Figure 2, A**): ^{1}H NMR (400 MHz, DMSO-d_6) δ 8.44 – 8.08 (m, 18H), 8.00 (s, 7H), 7.89 (s, 6H), 7.74 (s, 4H), 7.69 (s, 2H), 7.61 (s, 3H), 7.51 (s, 1H), 7.48 – 6.70 (m, 48H), 4.61 (s, 1H), 4.48 (s, 2H), 4.38 – 3.94 (m, 23H), 3.51 (s, 12H), 2.99 (s, 3H), 2.89 (s, 2H), 2.83 – 2.61 (m, 10H), 2.42 – 1.82 (m, 12H), 1.40 – 1.29 (m, 7H), 1.23 (s, 9H), 1.15 (t, J = 6.9 Hz, 2H), 1.10 (d,

J = 2.3 Hz, 2H), 0.85 (d, J = 14.2 Hz, 17H)**.** HRMS (MALDI-TOF) m/z: $[M+H]^+$ Calc'd for $C_{135}H_{191}N_{41}O_{18}H$ 2675.53; Found 2675.649. CPTNP-GG ^{1}H NMR (400 MHz, DMSO) δ 8.39 (dd, *J* = 14.7, 7.6 Hz, 4H), 8.33 – 8.22 (m, 8H), 8.18 (s, 1H), 8.16 (s, 3H), 8.15 – 8.09 (m, 6H), 8.09 – 7.94 (m, 9H), 7.93 – 7.73 (m, 8H), 7.70 (s, 2H), 7.64 (s, 2H), 7.51 (s, 1H), 7.21 (s, 44H), 4.22 (s, 13H), 4.11 (s, 4H), 3.87 – 3.68 (m, 9H), 3.51 (s, 9H), 2.99 (s, 2H), 2.89 (s, 2H), 2.73 (d, *J* = 17.5 Hz, 5H), 2.16 (p, *J* = 7.3 Hz, 3H), 2.03 – 1.92 (m, 3H), 1.38 (s, 5H), 1.23 (s, 12H), 1.17 – 1.13 (m, 3H), 1.11 (d, *J* = 2.3 Hz, 1H), 0.91 – 0.74 (m, 20H).HRMS (MALDI-TOF) m/z: $[M+H]^+$ Calc'd for $C_{121}H_{179}N_{41}O_{18}H$ 2495.44; Found 2495.960.

DBCO Oxaliplatin synthesis:

Oxaliplatin was added to a mixture of H2O: 30% H2O2 (3:7) and stirred overnight. Oxaliplatin slowly dissolved and crashed out of solution. After the reaction was completed, the mixture was further diluted and cooled to 4˚C. The solution was then centrifuged, and the resulting solid was washed with water three times. The resulting solid was dried and used for conjugation to DBCO COOH without purification.

Oxidized oxaliplatin was stirred in DMF with DBCO-COOH (3 eq), triethylamine (3 eq), and TBTU (3 eq) overnight in the dark. The mixture was precipitated with diethyl ether, centrifuged, and washed three times. After drying under nitrogen, the mixture was dissolved in ethanol and precipitated with water. The product was used without further purification. LCMS: expected m/z = 1004.24 (M + H)+ found 1004.25. The procedure was adapted from Zhang et al., 2013.[21]

Nano-formulation:

Peptide powder was dissolved in DMSO at concentration 20mM and allowed to sonicate for approximately one hour or until all solids were dissolved and solution was clear, similar to our other publications.[22,23] To form nanoparticles, DMSO solubilized monomers were rapidly pipetted into PBS (or a phosphate-citrate) solution buffered at pH 7.4. The solution is then vigorously vortexed for 30 seconds. To form nanofibers, the nanoparticle solution is diluted into an acidic phosphate-citrate buffer solution to achieve a final pH < 5.0.

To form crosslinked CPTNP 2.0s, nanoparticles were formed as mentioned above at a concentration of 0.2mM and allowed to stabilize for at least two hours at 37ºC. DBCO-Oxaliplatin was then solubilized in a minimal amount of DMSO and rapidly added to the nanomaterial solution to avoid oxaliplatin deactivation via DMSO. DBCO-Oxaliplatin was added to CPTNP 2.0 at a 1.1:1 DBCO-Oxaliplatin: CPTNP 2.0 molar ratio. The sample was then allowed to incubate at 27ºC for two hours on an Eppendorf thermomixer at 1000RPM. Subsequently, the sample was dialyzed three-fold, two hours, two hours, 16 hours, utilizing a 20kda float-a-lyzer dialysis system (Spectrum™ G235035) and 4L of water for each dialysis. Dialysis is critical here to remove DMSO, which can inactivate cisplatin-based drugs.

Characterization of Nanomaterials:

The size distribution of nanoparticles was carried out via dynamic light scattering instrument (DLS, Nano ZS, Malvern) at 25 ºC. The concentrations of the nanoparticles were 40µM for DLS measurements. Subsequent measurements were carried out using transmission electron microscopy, utilizing a Thermo Fisher FEI Talos system. Samples

were prepared by carefully dipping G200 copper grids, procured from electron microscopy sciences, into 40µM solutions of nanomaterials. Samples were allowed to dry upright in the copper grid holder.

In vitro studies:

A549 cells were procured from American type tissue culture (ATCC) and cultured in Dulbecco's Modified Eagle Medium (DMEM) supplemented with 10% Fetal Bovine Serum penicillin and streptomycin.

3-(4,5-dimethylthiazol-2-yl)-5-(3-carboxymethoxyphenyl)-2-(4-sulfophenyl)-2H-tetrazolium (MTS) assays were carried out using the kit procured from Promega (G1111). A549 cells were seeded into 96 well plates at 1000 cells/well after straining through a 40µM mesh to ensure a single cell solution and allowed to incubate overnight. The plate was checked to ensure even cell growth in all wells and treated with the appropriate dosage of material. After incubation for 72 hours, media was removed, and new media containing 20% MTS and 1% phenazine ethosulfate was added to each well. Wells were allowed to incubate at 37ºC for 1hr, covered in foil. Absorbance was then measured at 490nm using a standard plate reader. Curves were then fit using GraphPad prism, and IC 50s plotted to generate an isobologram.

All microscopy was carried out on a Zeiss LSM 800 confocal microscope unless otherwise specified. Image quantification was performed using ImageJ. For all studies, at least five images were quantified per well with at least 40 cells per well. The five images were averaged (1 replicate), and at least three wells were averaged. Statistics were analyzed via GraphPad Prism 6.0. Lysotracker green (Ex/Em:504/511nm) was

procured from Thermo Fisher (Catalog number: L7526). Texas Red labeled cisplatin (TR-Cisplatin, Ex/Em: 568/603nm) was procured from Ursa Biosciences. For the detection of Cisplatin DNA adducts, a rat Anti-cisplatin monoclonal antibody was procured from Sigma-Aldrich (MABE416). Anti-clathrin. For Annexin V/PI flow cytometry, the Dead Cell Apoptosis Kit from Thermo Fischer (V13241) was used. Flow cytometry was performed on a desktop Guava easyCyte. For Caspase 3 western blot, the anti-caspase three antibodies from Abcam were used (ab4051).

For the development of the GFP-LC3-RFP expressing A549 cells, a custom retrovirus was developed by ABM incorporating the GFP-LC3-RFP plasmid procured from add gene (pMRX-IP-GFP-LC3-RFP, Plasmid #84573) derived from Kaizuka et. Al. [16]. To transduce A549 cells, $1X10^5$ cells were seeded into each well of a six well plate and allowed to incubate overnight at 37ºC and 5% CO_2. $5X10^5$ IU of retrovirus was introduced to each well and allowed to incubate for three days. The media was then replaced, and cells were then incubated with puromycin to select transduced cells. The properly transduced cells were then selected for on an Astria fluorescence-activated cell sorter under starvation conditions to ensure complete incorporation of the plasmid into the host. To measure autophagic flux of the cells, GFP-LC3-RFP A549 cells were seeded on a 96 well plate and treated as documented below. Five images per well were acquired and averaged for each replicate. Three replicates were averaged for the final value. An increase of GFP relative to RFP indicates the inhibition of autophagy, while the decrease of GFP relative to RFP indicates the inducement of autophagy.

In Vivo studies:

Nude mice, 4~5 weeks of age, were ordered from the Jackson Laboratory (Sacramento, CA). All animal procedures were performed under the requirements of institutional guidelines and according to protocol No.19724 approved by the Use and Care of Animals Committee at the University of California, Davis. A549 cells were grown at scale in corning Cellstack 10 layer flask (Corning 3270); cells were incubated utilizing 2L of media. Cells were harvested utilizing 300mL of 0.05% trypsin (25300054). Cells were subsequently washed two times in PBS after centrifugation at 200g. A549 cells were then suspended in a PBS and Matrigel solution (1:1 vol/vol). The slurry was then injected subcutaneously into the right and left flank of nude mice. $1.2X10^7$ cells per flank were injected. The tumor sizes for all nude mice were monitored and recorded at least bi-weekly. Tumors reaching the dimensions of >100 mm^3 were used for the treatment study.

Athymic mice bearing A549 NSCLC xenografts were used for the *in vivo* therapeutic studies (n=6/group). Nanomaterials and PBS were injected via tail vein. Eight doses, one dose every third day, along with IP cisplatin, were administered as reported. Tumor volume and body weight were measured several times per week utilizing a digital caliper and digital scale. Once the humane endpoint was reached, tumor volume exceeding 2000 $mm^{3,}$ the mice were sacrificed, and blood was harvested for evaluation via extraction through the heart. Mouse blood was allowed to clot at 4ºC for 24hours, and the sample was centrifuged at 12,000G for 30 minutes. The supernatant blood plasma was then removed, and blood chemistry was analyzed in a Heska Dri Chem 7000.

In vivo real-time monitoring of autophagic flux:

NSCLC A549 cells expressing GFP-LC3-RFP adherent to the bottom of a T75 flask were trypsinized with 0.05% trypsin-EDTA, which was subsequently neutralized with culture medium. Floating cells were collected and washed twice, resuspended in phosphate-buffered saline (PBS) at 10^7/ml, and maintained on ice for immediate ocular injection. Aliquots of the cells were routinely imaged with a Zeiss LSM800 confocal microscope at 20X and 40X for quality control, including assessment of GFP/RFP fluorescence and cell size (diameter 10.3 ± 3.2 μm, mean ± s.d., 120 cells from 4 preparations). Ocular transplantation of cells between the retinal pigment epithelium (RPE) and the neural retina and was performed under visual guidance of a 2-3X dissection microscope using the method of Matsumoto et al. [24]. Mice were anesthetized with 2% isoflurane, and pupils dilated with 1% tropicamide and 2.5% phenylephrine. A small scleral incision was made in the superior limbus (12 o'clock) with the bevel of 31G needle (BD Ultra-Fine Short Needle), with superficial penetration to drain aqueous humor and reduce intraocular pressure. A 34G needle (Retinal Pigment Epithelium Kit, WPI, Sarasota, FL) connected to a 10 μl syringe (NanoFiL-100, WPI) was then passed through the incision and slowly inserted into the subretinal space so that the blunt needle tip was within 1 to 1.5 mm of the optic nerve head in the superior retina. A small volume (0.5 or 1.0 μL) of the cell suspension was gently injected under the control of a microinjection pump (Nanoliter 2010 UMP3 controller, WPI) at a rate of 225-450 nL/s. The conjunctiva was repositioned with forceps, and a lubricant eye gel (GenTeal, Novartis, Switzerland) was applied to the cornea. A coverslip was gently pressed to the

cornea, and the fundus was evaluated with the microscope. Mice having retinal holes or subretinal or vitreous hemorrhages were excluded from the study.

To measure the shift in the autophagic flux of the eye, GFP-LC3-RFP A549 cells were implanted into the retina of athymic mice. Xenografts were allowed to grow for one week, then tumor fluorescence and size were monitored using a custom-built optical coherence tomography and Scanning laser ophthalmoscope miniaturized for the mouse eye, referred to elsewhere as the eyepod.[17]

Mice were anesthetized with 2% isofluorane and O2; the pupils were dilated and cycloplegic with tropicamide and phenylephrine. Gel Tears with 0.2% carbomer (Chem-Pharm Fabrik, Berlin, DE) was applied between the corneal surface and the custom 0 Dpt contact lens (Unicon Corporation, Osaka, Japan) to moisturize the eye. The mouse was positioned onto the anesthetic delivery system via a bite bar mounted on a micropositioner (Bioptigen, Morrisville, NC) with rotational and translational degrees of freedom such that the eyepod could be positioned with respect to the contact lens. Fluorescent light from the mouse was separated by two dichroic mirrors (FF509-FDi01 and FF640-FDi01, Semrock) into three channels: < 509 nm for back-reflection imaging henceforth referred to the as bright field. 509 nm-595 nm for fluorescence imaging (with an additional band-pass filter FF01-525/45 for GFP fluorescence). Greater than 595 nm further filtered (FL670-10, Thorlabs) for RFP fluorescence. The light from the back-reflection and fluorescence channels was collected by selectable optical fibers (typically, with an aperture of 4 Airy discs), and then passed to PMTs (H7422-50 for back-reflection, and H7422-40 for fluorescence, Hamamatsu Photonics), and amplified for the data acquisition system.

3.3. Results and Discussion

CPTNPs sensitize A549 cells to cisplatin *in vitro*

Based on previous studies indicating that cisplatin could be sequestered into the lysosome as a mechanism of cancer-chemotherapeutic escape, we were interested to see if the lysosomal perturbation of CPTNP could boost the activity of cisplatin. To demonstrate the synergistic cytotoxic effect of CPTNPs with cisplatin *in vitro*, we performed a series of MTS assays with varying levels of cisplatin and peptide and then developed a standard isobologram.[25] We found that while cisplatin alone had an IC_{50} >2μM, 100nM of CPTNP could lower the IC_{50} approximately 4-fold **(Figure 1, A**). At 100nM CPTNP, the combination index was determined to be 0.259 (**Figure 1, A**). This indicates that CPTNPs are highly synergistic with cisplatin in A549 cells. That is the combined effect of both treatments is more than additive.

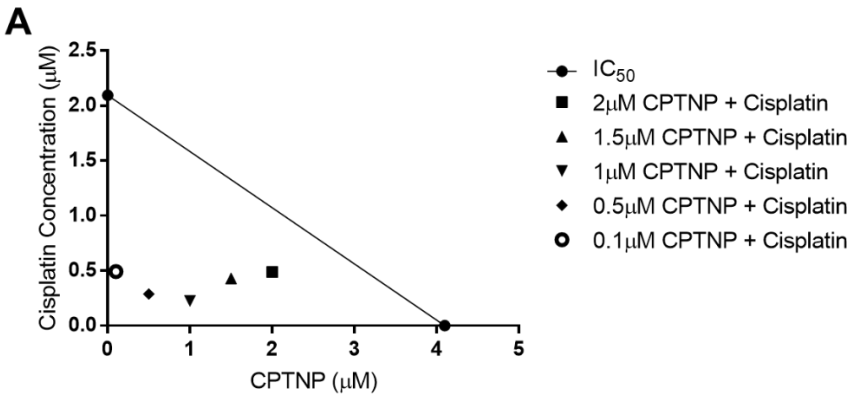

B

[CPTNP] (μM)	CI
2	0.721
1.5	0.571
1	0.352
0.5	0.260
0.1	0.259

Figure 1. A. An isobologram representing the IC50 of cisplatin and CPTNPs alone, and combination treatments (48 hr) of cisplatin and CPTNPs in combination with constant

CPTNP concentration with varied cisplatin concentration. **B**. the combination index (CI) of each treatment regime using the IC50 values documented.

Previous literature has pointed to several mechanisms of cisplatin sensitization via lysosomal inhibitors. To elucidate the mechanism by which cisplatin sensitization was achieved here, A549 cells were sequentially treated first with Texas Red-cisplatin (TR-cisplatin) conjugates for 24 hours at two µM, then CPTNPs at 10 µM for 4 hours. Cells were then stained with LysoTracker Green (a dye similar to LysoTracker Red), fixed, and observed at 63X on a Zeiss LSM 800 confocal microscope. While a punctate pattern was observed in the Texas Red signal of untreated cells, which colocalize with LysoTracker Green, CPTNP treated cells demonstrated a diffuse Texas Red signal (**Figure 2, B**), further confirmed by the decrease in Pearsons R coefficient (**Figure 2, C**). This indicates that CPTNPs facilitate the cytoplasmic distribution of cisplatin. We hypothesized that the increased cytoplasmic distribution of cisplatin would allow for increased cisplatin activity, as more cisplatin is free to bind with DNA and therefore increased cell death.

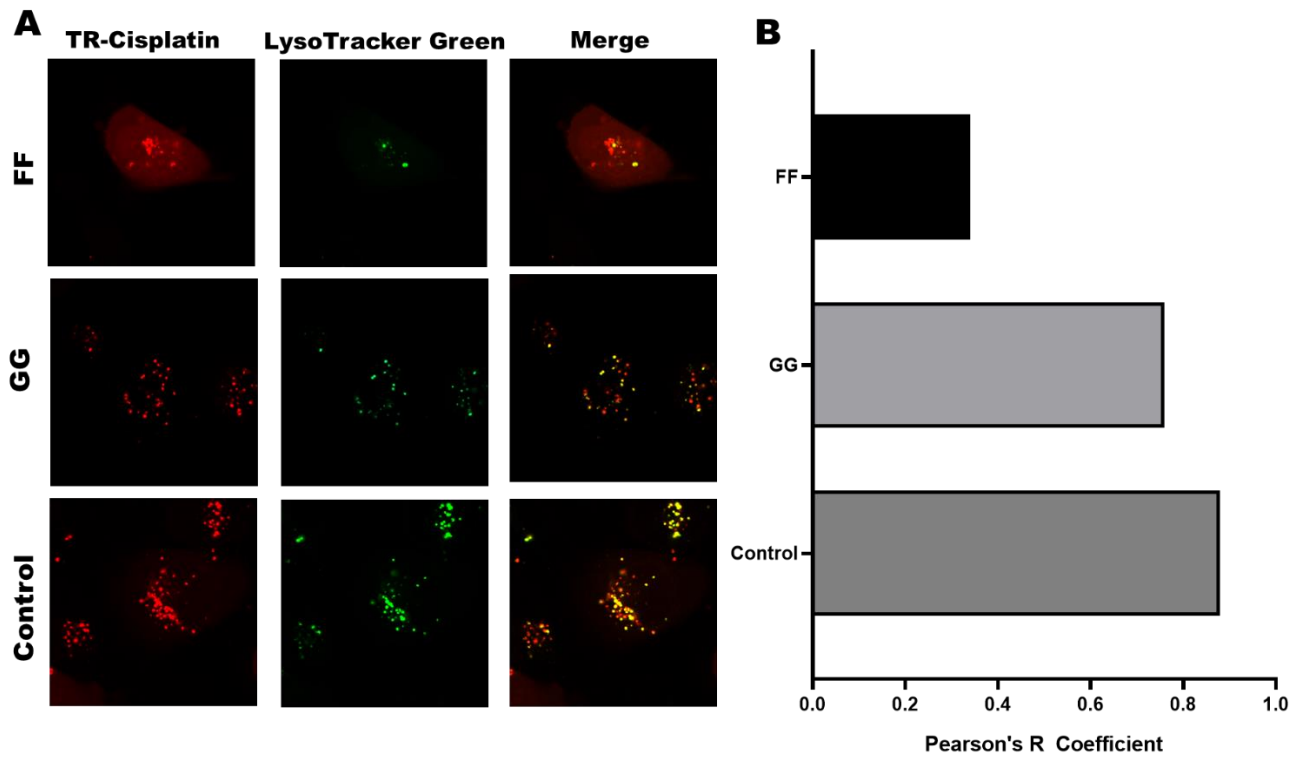

Figure 2: A. Representative image of TR-Cisplatin treated A549 cells (2 µM) stained with LysoTracker Green with or without CPTNP treatment (10 µM). Where red represents cisplatin, green represents lysotracker green. In the treated case cisplatin can be seen to be cytosolically located. **B.** Pearson's R coefficient between LysoTracker Green and TR-cisplatin derived from B utilizing ImageJ demonstrating decreased lysosomal sequestration of TR-cisplatin.

To test this hypothesis, we obtained an anti-cisplatin DNA adduct antibody (Sigma-Aldrich: MABE416) and treated A549 cells with cisplatin alone, CPTNP-FF alone, and CPTNP-FF and cisplatin as seen in **Figure 3, A**. Cisplatin DNA adducts are

clearly enhanced in the case of combined CPTNP-FF and cisplatin, confirming our hypothesis that CPTNP-FFs boost the available cisplatin for activity. Quantification of the increase in anti-cisplatin DNA adducts in the nucleus of A549 cells is shown in **Figure 3, B**.

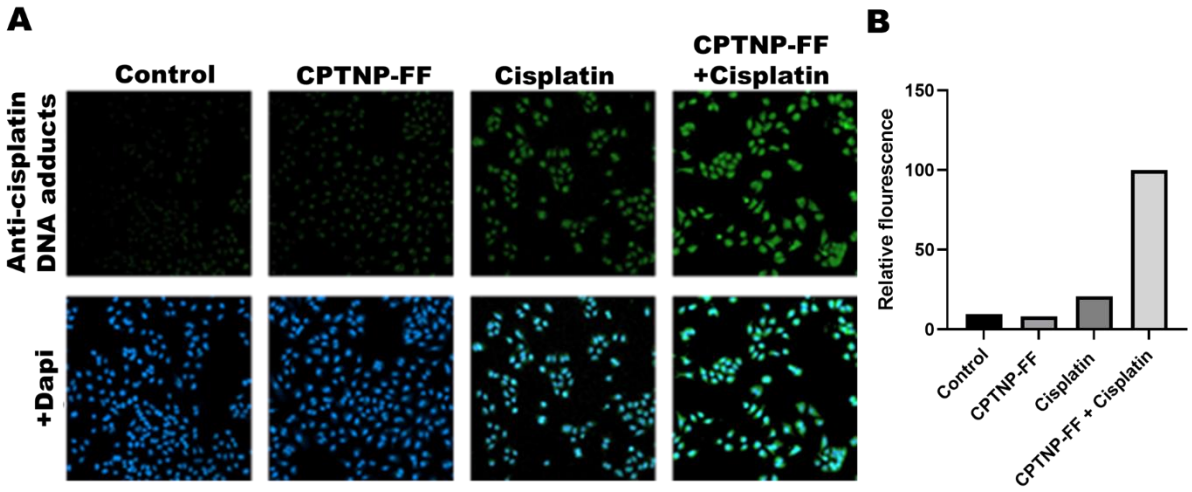

Figure 3: A To measure the effect of CPTNPs on cisplatin-DNA adducts, cells were treated with cisplatin, CPTNP-FF (2uM) or both and stained with anti-cisplatin DNA adducts. Representative images may be seen. **B**. Signal co-located with dapi signal was quantified. Fluorescence intensity was measured and was greatly enhanced in the cisplatin + CPTNP-FF case demonstrating the synergistic effect noted above.

This result suggests that the LMP activity demonstrated previously is responsible for cisplatin-lysosome escape and, therefore, CPTNP-cisplatin synergism. A schematic of this mechanism is summarized in **Figure 4**.

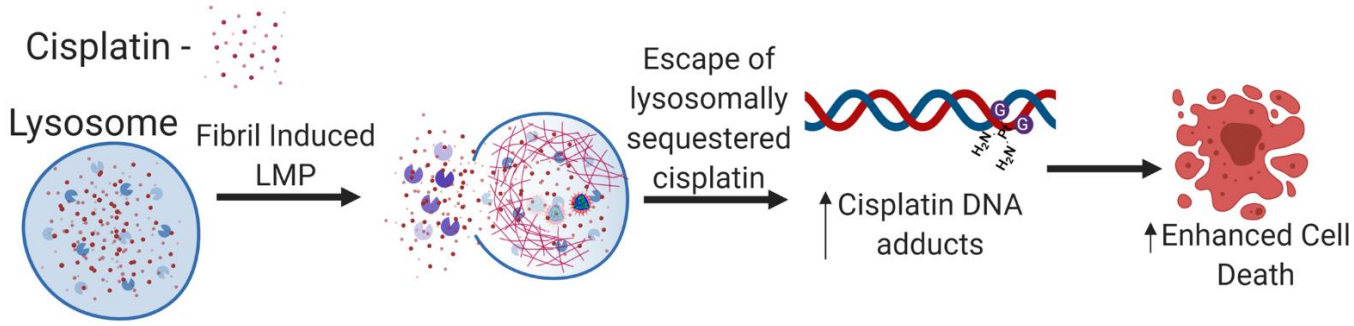

Figure 4: Proposed mechanism of cisplatin sensitization. Cisplatin, sequestered in the lysosome is freed by the LMP action of CPTNPs, allowing for increased availability of cisplatin and increased cell death.

CPTNP effect on autophagic flux in vivo and in vitro

We had initially hypothesized that CPTNP-cisplatin synergism was enabled by autophagic inhibition of A549 cells. Indeed, other lysosomal inhibitors, like chloroquine, have generated significant interest due to their inhibition of autophagy and, therefore their chemotherapeutic synergism in several tumor types.[26,27] We believed a similar autophagic inhibitory effect might be caused by CPTNP LMP. To test this hypothesis, we generated A549 cells transduced with an internally controlled autophagy probe as described in Kaizuka et. Al.[16] The probe consists of two fluorescent probes on opposite terminals of the autophagic substrate LC3. The RFP is cleaved off of the substrate by the autophagy related protease-ATG4, leaving GFP-LC3 which is subsequently degraded by autophagy. Because the GFP and RFP are expressed at once, they are

expressed in equimolar amounts. Therefore, the autophagic flux may be quantified by measuring the relative GFP/RFP signal. If the GFP/RFP signal is low, that is indicative of high autophagy. If the GFP/RFP signal is high, that is more GFP to stable RFP, that is indicative of low or inhibited autophagy. We chose to transduce A549 cells using a custom retrovirus procured from ABM to ensure stable expression of the probe. Stably expressing cells were selected for using puromycin, and later FACS under starvation conditions to ensure the correct behavior of the probe. Cells were further validated using the drug hydroxychloroquine to demonstrate GFP/RFP ratio increased with the inhibition of autophagy. To demonstrate the effect of CPTNPs on autophagy in the GFP-LC3-RFP model we treated GFP-LC3-RFP transduced A549 cells with 1µM CPTNP for 24 hours and observed measured the GFP/RFP ratio. To measure the GFP/RFP ratio, 5 images from different regions of a single well were averaged, to account for one replicate. Four replicates were acquired to give the final value. Here we show an increase in the GFP/RFP ratio when comparing control to CPTNP treated samples, 3.0 vs 7.4 respectively, indicative of inhibited autophagy.

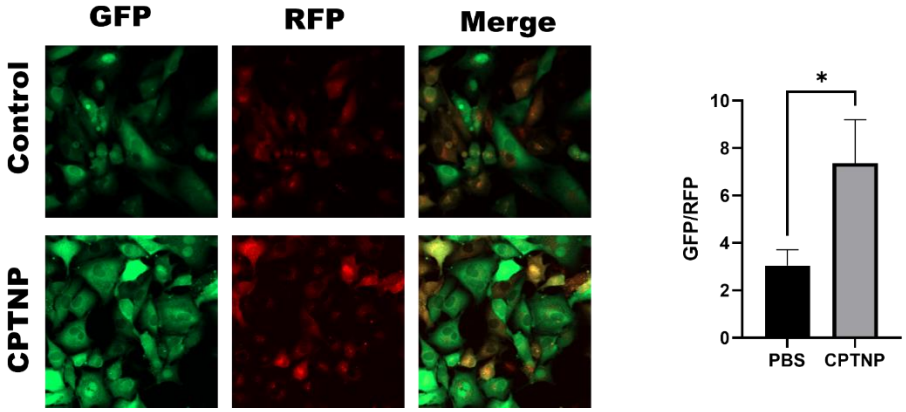

Figure 5: Representative images of GFP-LC3-RFP transduced cells treated with 1µM CPTNP for 24 hours (right). The quantified difference in GFP/RFP ratio between the two

images as enumerated via five images, in three separate wells. (left) the change in ratio is indicative of the inhibition of autophagy.

To test this mechanism in vivo we implanted subretinally into the nude mice GFP-LC3-RFP A549 human NSCLC cells. As a positive control we anesthetized mice with stable flow isoflurane using a nose cone and injected a single bolus of hydroxychloroquine via tail vein injection. We then monitored the GFP/RFP ratio of the subretinal xenograft every hour using the in-house developed EYEPOD murine SLO/OCT system[17] which would allow real time monitoring of tumor autophagic flux modulation in response to small molecule drugs. In the hydroxychloroquine treated mice, we were able to demonstrate a marked increase in tumor GFP/RFP ratio approximately 6 hours after drug dosing (**Figure 6, A)**. In contrast, no change in tumor GFP/RFP ratio was observed in mice treated with CPTNP. The lack of GFP signal was persistent in several trials with several CPTNP dosages. This led us to conclude that autophagy may play little role in the therapeutic capacity of CPTNPs in vivo, and suggests that other mechanisms, such as lysosomal mediated cell death may, and cisplatin sensitization may play more important roles in vivo.

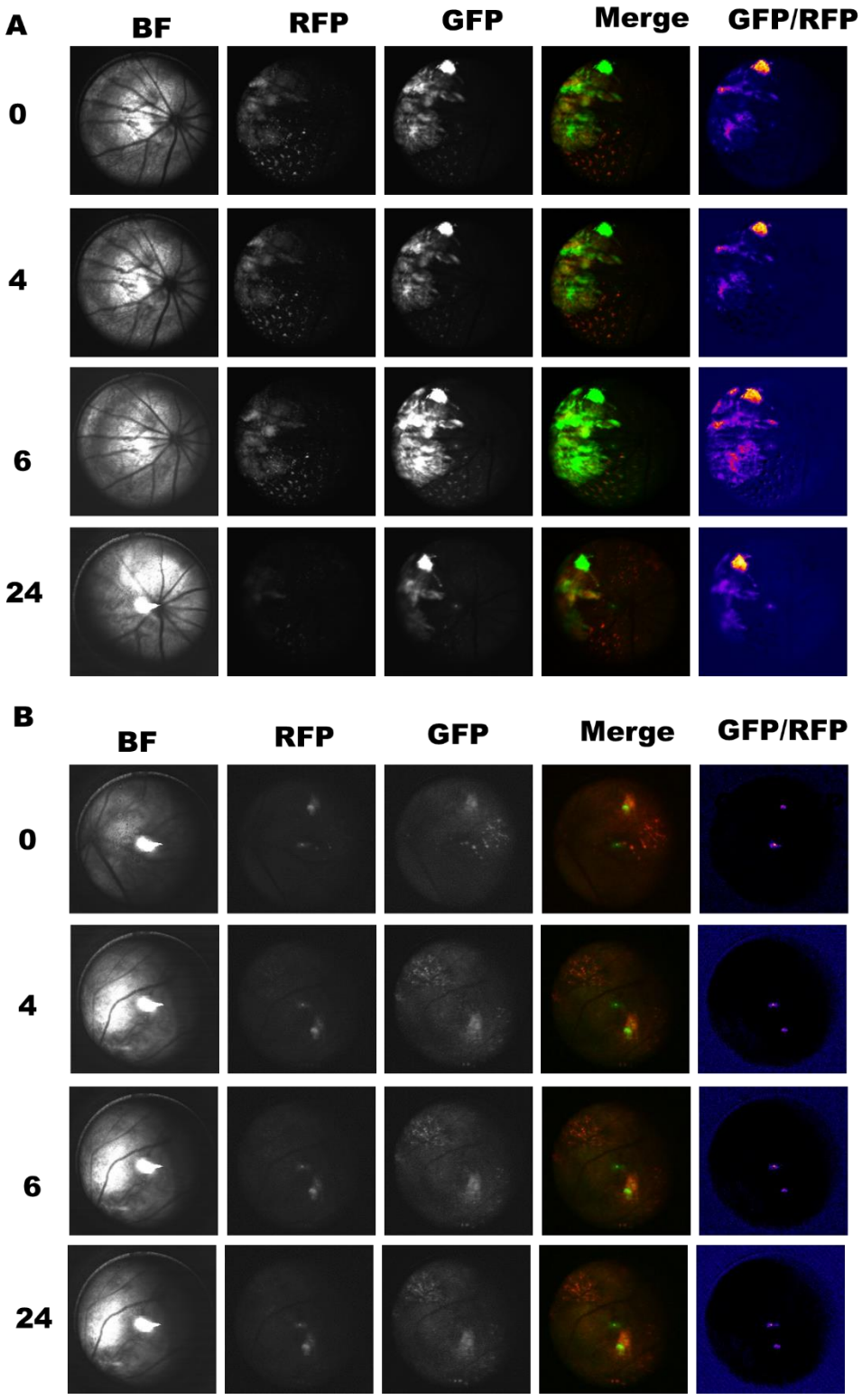
A
BF
RFP
GFP
Merge
GFP/RFP
0
4
6
24
B
BF
RFP
GFP
Merge
GFP/RFP
0
4
6
24

Figure 6: A. Mouse retina with implanted GFP-LC3-RFP A549 cell xenograft, as visible by the green and red fluorescence. The mouse was dosed with a bolus of hydroxychloroquine and immediately imaged to give the response seen above. The first panel is a bright-field image of the retina, while the second and third images represent fluorescence imaging, the fourth image represents the second and third image merged, while the final image is the second image divided by the third image in each pixel to give the localized autophagic flux. **B.** Similar imaging study was performed in mice treated with 5mg/kg CPTNP; no effect was observed.

***In vivo* tumor xenograft model**

To determine the *in vivo* anti-tumor effect and to measure any toxicity of CPTNPs and duel CPTNP-cisplatin therapy, 32 athymic mice were injected subcutaneously with 12×10^6 A549 NSCLC cells in each flank (two tumors per mouse). When tumor burden reached 100 mm^3 the mice were separated into 5 groups: CPTNP-FF (2mg/kg), CPTNP-FF (2mg/kg) + cisplatin (1mg/kg), CPTNP-GG (2mg/kg), CPTNP-GG (2mg/kg) + cisplatin (1mg/kg), and PBS control. Eight doses of each treatment (CPTNP: IV, cisplatin: IP, **Figure 7, A**) were administered every third day for 21 days, as depicted in **Figure 7, B**.

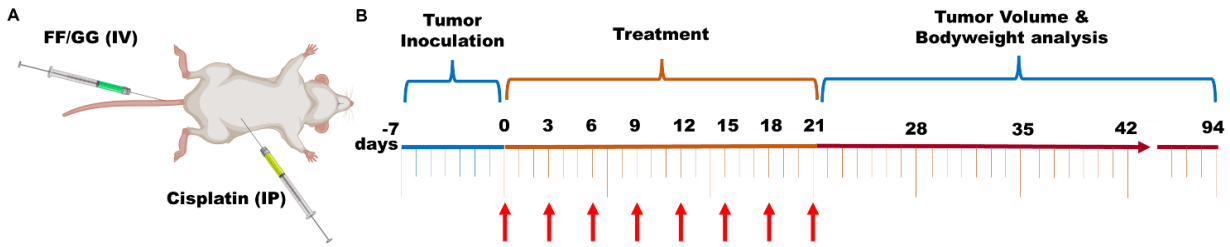

Figure 7: A. Schematic demonstrating the administration method for both CPTNP (tail vein injection) and cisplatin (intraperitoneal injection). **B**. Treatment regime for CPTNP and cisplatin.

Mice were monitored bi-weekly until the humane endpoint was reached (tumor volume >2000mm^3), tumor volume was monitored via digital caliper (**Figure 8, A**). Notably, mice treated with CPTNP-FF + cisplatin experienced significantly reduced tumor burden as compared to all other groups, indicating the synergistic action of the CPTNP-FF/cisplatin treatment. CPTNP-FF had little activity on its own, this is likely due to the lowered dosage (2mg/kg) vs. chapter one (5mg/kg). After 30 days, the tumor volume was measured using a digital caliper, and the volumes were analyzed via ANOVA with a post hoc Tukey test using GraphPad prism. The following adjusted P values were found, FF-Cisplatin P = 0.0003, FF-Cisplatin vs GG-cisplatin, P= 0.0076, FF-Cisplatin vs GG, P < 0.0001, FF-Cisplatin vs PBS, P = 0.0014. All other P values were not significant. This trend was reflected further in the mean survival rate of mice treated with CPTNP-FF + cisplatin, which was nearly two-fold greater than any other group (**Figure 8, B, C**). Here, the average survival of each group was similarly analyzed (n=6). The P values were as follows: FF-Cisplatin vs FF, GG, and PBS, P < 0.0001,

FF-cisplatin vs GG-cisplatin, P = 0.0008 all other comparisons were not significant. Bodyweight was monitored on an electronic scale. While some reduction in weight may be observed in CPTNP-FF + cisplatin vs. other groups, mice quickly recovered after the treatment was completed. Once the humane endpoint was reached, blood was collected from three of six animals, and a biochemistry panel was run on a Heska, DRI-CHEM 4000 (**Figure 8, D**). No significant differences were observed between the CPTNP and PBS treated groups, indicating limited toxicity. While some liver accumulation may be seen in biodistribution data, no changes in total bilirubin, alkaline phosphatase, nor ALT were seen, indicating limited toxicity. This conclusion is substantiated by murine bodyweight measurements, which trend down during cisplatin treatment (but not CPTNP alone) but recover quickly after treatment (**Figure 8, E**). Taken together, these results suggest that CPTNP-FF at a low dose, as compared to chapter one, in conjunction with low dose cisplatin treatment, can modulate tumor mass in a fibril-dependent manor. This is very encouraging for the future of the platform.

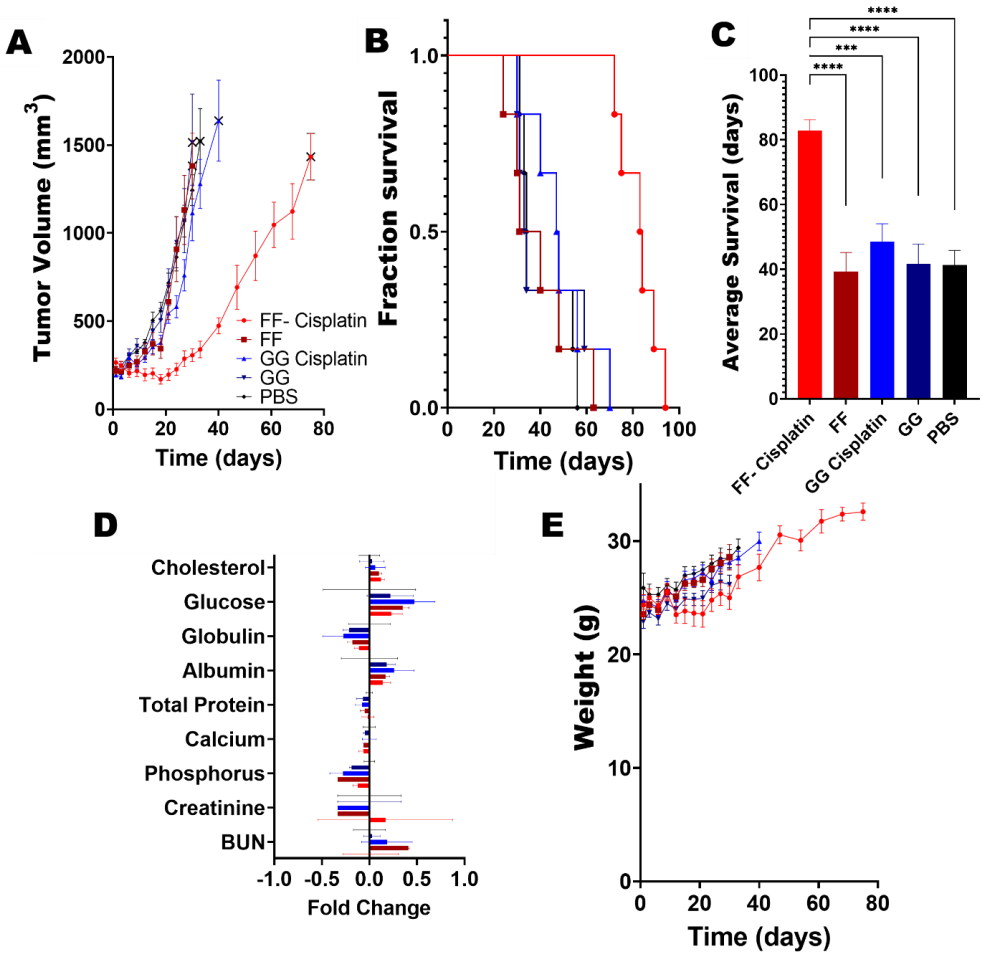

Figure 8: A. The documented tumor volume from the above study, once tumor volume exceeded 2000mm. Once one-third of one trial group reached the humane endpoint, trendlines are no longer reported (Day 30). Tumor volumes were subjected to ANOVA with post hoc Tukey test. No significant difference was observed between groups FF, GG, GG-cisplatin, and PBS. All groups were significantly differentiated from FF-cisplatin ($P < 0.01$), where FF-cisplatin – FF ($P = 0.0003$), FF-cisplatin – GG-cisplatin ($P = 0.0076$), FF-cisplatin – GG ($P < 0.0001$), FF-cisplatin – PBS ($P = 0.0014$). (N= 12) B. Kaplan-Meier plot of each group (N=6). C. Average survival of each group. (****, $P < 0.0001$; ***, $P<0.001$) Statistics were determined via ANOVA with post hoc Tukey test. D. Blood chemistry of mice from the above study (N=3) reported as a fold change from

PBS control. No results deviated significantly from the control. Analyzed on a Heska Dri-chem 7000. G. Weight of mice from the above study (N=6), reported here until the humane endpoint for 1/3 of mice was reached. E. Relative fluorescence of comparative samples indicating tumor localization of CPTNPs.

CPTNP 2.0

While the above results are promising, challenges surrounding the biodistribution, particularly liver uptake and the potential toxicity from the hydrophobic dye BP prompted the design of novel CPTNPs with several improvements. The novel CPTNPs similarly consist of three domains first, a hydrophobic domain composed of porphyrin, the amino acid sequence klvffK(N_3)K(N_3), and a shorter all D-amino acid polyarginine sequence $(r)_4$, as opposed to $(r)_8$, to reduce the particle's overall positive charge. The porphyrin domain is an improvement over bispyrene for eventual clinical applications as it is biocompatible and has already been studied as an effective and non-toxic phototherapeutic agent. Moreover, our group has previously demonstrated that it can be used to form similar nanomaterials.[28] The modified fiber-forming motif k-l-v-f-f-K(N_3)-K(N_3) allows for the incorporation of crosslinking agents via click chemistry. In this case, we developed acid liable duel DBCO oxaliplatin. The $(DBCO)_2$ oxaliplatin cross-links the pre-formed CPTNPs, and once exposed to the acidic environment of the lysosome; the oxaliplatin pro-drug is converted into oxaliplatin and released from the

nanomaterial. At the same time, the cross-linkages are broken, and nanofiber formation is allowed.

Oxaliplatin was synthesized via oxidation and conjugation with DBCO-COOH via TBTU overnight in the dark, where it was subsequently precipitated in ether and washed.

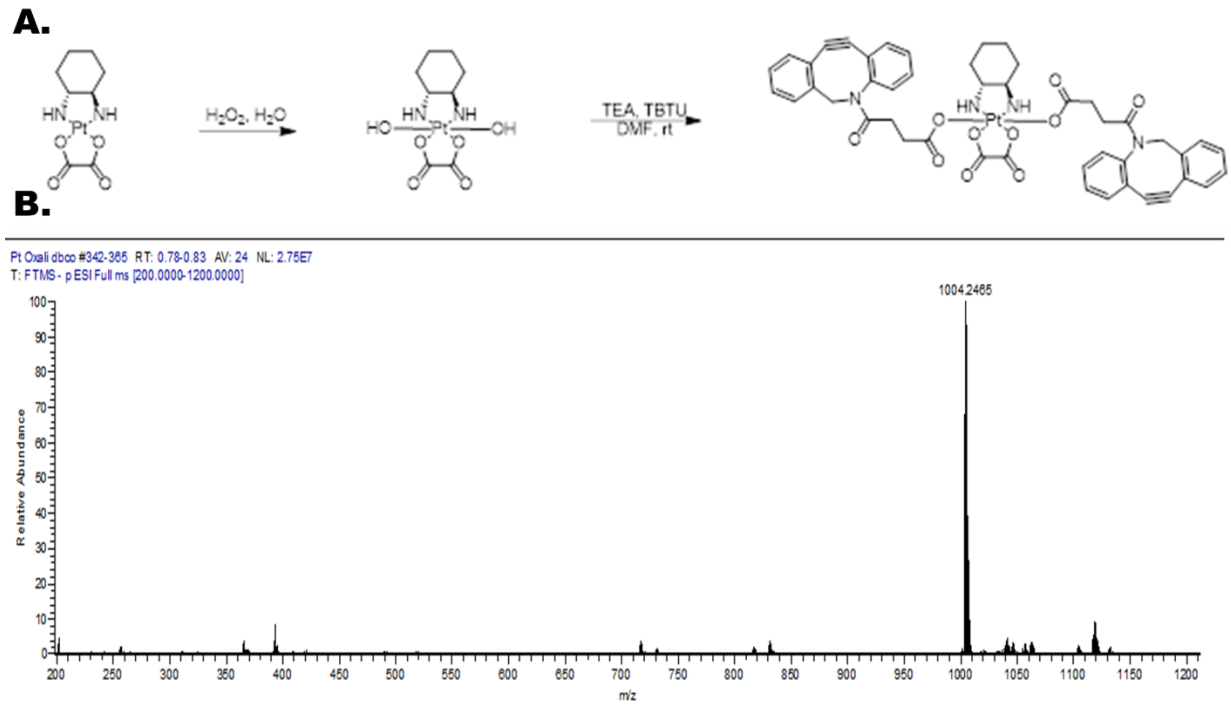

Figure 9: A. Synthesis of acid liable DBCO linked oxaliplatin. **B.** ESI mass spectra of the synthesized compound.

To form the DBCO-oxaliplatin crosslinked material, nanoparticle was first formed in ultrapure water as previously described. Briefly, peptide amphiphiles dissolved in DMSO were pipetted into the water at the appropriate concentration, then rapidly vortexed for 30 seconds. Next, DBCO-oxaliplatin was quickly dissolved in DMSO and quickly added to the aqueous nanomaterial solution, such that the total concentration of

DMSO was less than 2%. The solution was then mixed at room temperature for two hours and immediately dialyzed to remove excess DMSO and DBCO-oxaliplatin. The sample was then ready to use.

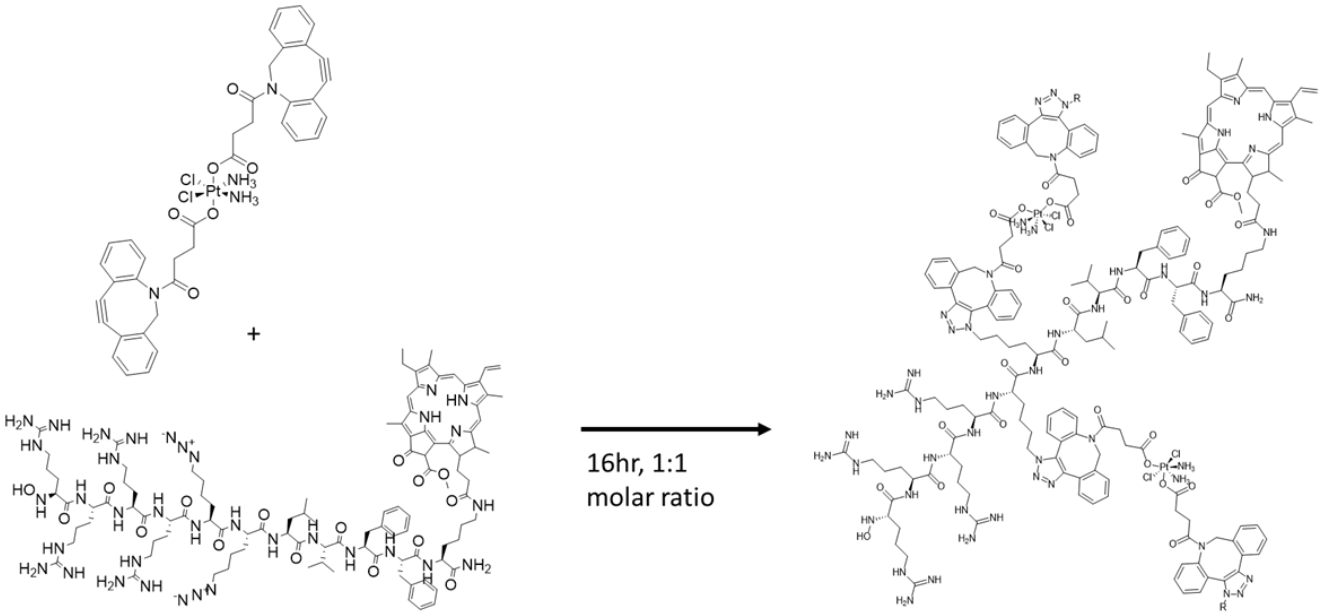

Figure 10: Crosslinking mechanism of CPTNP 2.0. Dual azides on the peptide amphiphile allow for two DBCO-oxaliplatin molecules to crosslink each peptide ampiphile to two additional peptide amphiphiles, thereby creating a crosslinked and oxaliplatin pro-drug.

To validate that crosslinked CPTNPs could form nanoparticles and transform into nanofibers when exposed to acidic pH, we measured the size via DLS, then lowered the

pH by diluting in acidic aqueous buffer. DLS measurement revealed an increase in size after exposure to acidic buffer, indicating fiber formation. **Figure 11**

To visualize this effect, both crosslinked and non-crosslinked samples were subjected to transmission electron microscopy (TEM). TEM micrographs revealed nanoparticles at pH seven and nanofibers at pH 4 in each case, indicating the material is able to form nanofibers.

In theory, crosslinked CPTNPs should have improved stability when compared to non-crosslinked CPTNPs. To investigate the stabilizing effect of crosslinking on CPTNPs, we diluted a concentrated nanomaterial solution in 5mg/mL sodium dodecyl sulfate (SDS), which we anticipate should hybridize with amphiphilic peptide monomers and break apart CPTNP micellular nanoparticles. We then monitored the material for 14 hours via DLS. While non-crosslinked material breaks apart quickly after the introduction of SDS, the crosslinked material persists for the duration of the experiment. Suggesting crosslinked materials are highly stable.

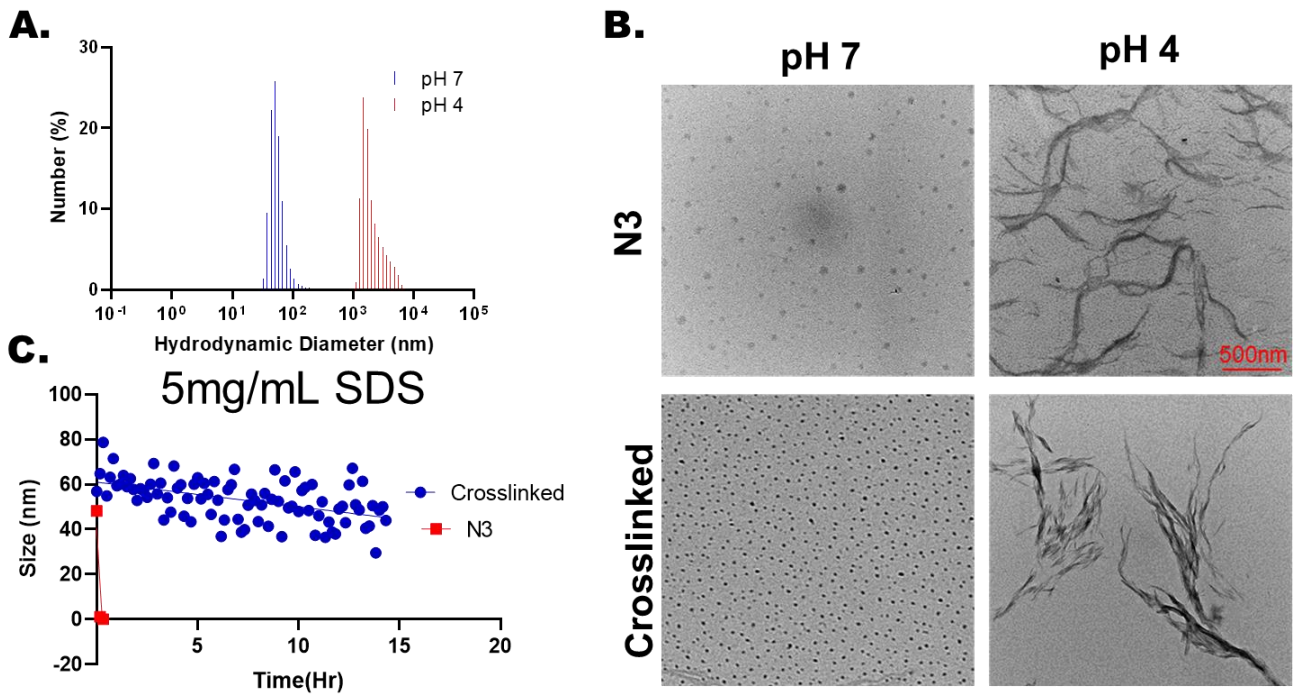

Figure 11: A. Dynamic light scattering data of DBCO-oxaliplatin crosslinked CPTNPs in pH 7 buffered PBS and particles from the same stock diluted into pH 4 buffer. Nanofibers result in the pH 4 buffer similar to previous formulations. **B.** Transmission electron micrographs of CPTNPs, both crosslinked and un-crosslinked buffered at pH 4 and pH 7. As previously indicated, acidic conditions induce fiber formation. **C.** Crosslinked and non-crosslinked material measured by DLS every 10 minutes for 14 hours or until DLS reading failed. Each point represents a discrete DLS reading (as opposed to three averaged readings as displayed in figure 11 A).

To determine the ability of crosslinked CPTNPs to localize to the lysosome of A549 cell lysosomes we treated cells with varying levels of CPTNP over 24 hours. While low doses show good lysosomal colocalization, higher doses show the loss of the lysotracker signal and cytosolic CPTNP signal. This is in alignment with CPTNP effects observed in Baehr et al. where the lysotracker signal dispersed over time; however, in this case, CPTNP fluorescence may be seen in the cytosol of treated cells. Because bispyrene is an aggregation-induced emission effect (AIEE) dye, it is likely that monomers escaping from the lysosome were not visible in the cytoplasm. Porphyrin is not an AIEE dye, and therefore it may be seen in the cytoplasm of treated cells. Overall, the effect of loss of lysotracker signal and cytosolic CPTNP at higher concentrations, but lysosomal colocalization at lower concentrations (0.2μM) is consistent with lysosomal membrane permeabilization, observed in chapter 1. This further suggests that the acid liable crosslinking does not inhibit the ability of CPTNPs to form nanofibers in the lysosome of NSCLC cells and induce LMP.

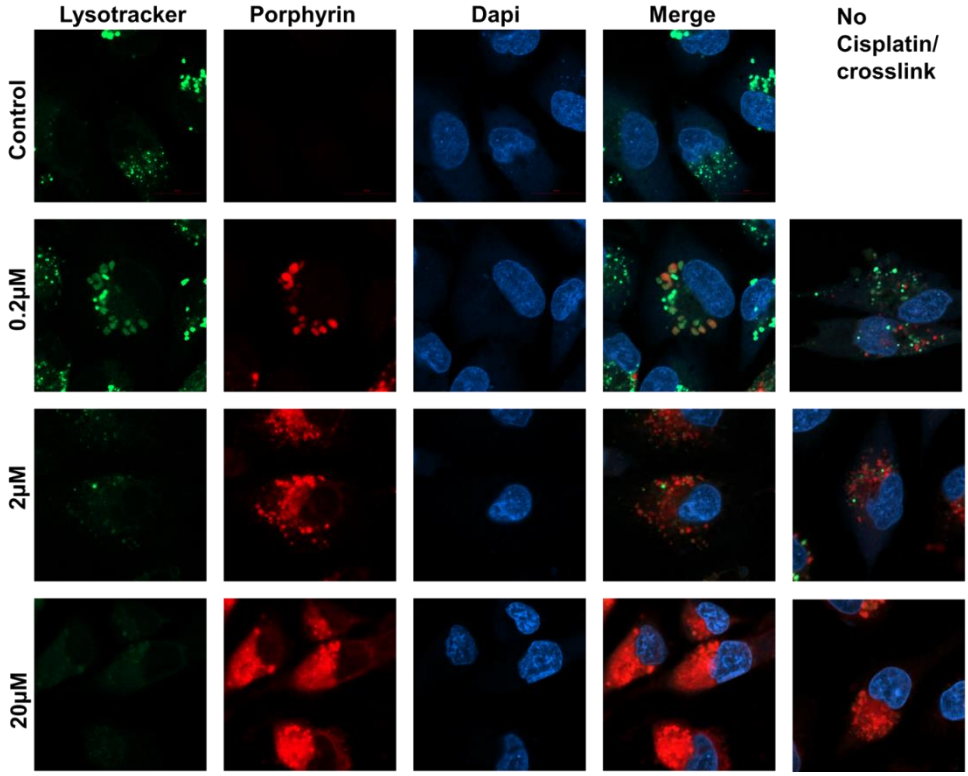

Figure 12. A549 cells treated CPTNPS, both crosslinked and un-crosslinked, and counterstained with DAPI and lysotracker green. Cells were treated with CPTNPs for 16 hours, stained with lysotracker 30 minutes before fixation, and immediate imaging on a Zeiss LSM 800 Confocal scanning laser microscope. Crosslinked CPTNPs demonstrate the similar activity to non-crosslinked CPTNPs

---

To further improve the biodistribution of CPTNP 2.0s, we desired to lower the surface charge of the material. Previous studies have demonstrated that high liver delivery is correlated with high zeta potential in nanomaterials.[19] To accomplish this, we incubated crosslinked or un-crosslinked CPTNP 2.0s with 20kDa heparin at 10u/μL (Thermo Fisher AAA16198MD). Heparin is typically used as an anticoagulant agent and can be used to coat tubing or other materials which come into contact with blood. It is also highly negatively charged. Therefore, we suspected that the negatively charged

heparin could coat the surface of CPTNP 2.0s and give the material a negative charge, thus escaping liver uptake and improving circulation time. Indeed, the zeta potential was found to change from +32mV to -27mV after heparin coating. Interestingly, after incubation with heparin, dialysis for over 72hr failed to revert the zeta potential, as reported in **Figure 13, B**.

The heparin coating did not impact CPTNP uptake as porphyrin fluorescence remained stable with and without coating, suggesting the heparin coating may be an attractive mechanism to enhance tumor uptake. But reduce liver uptake (**Figure 13, C**)

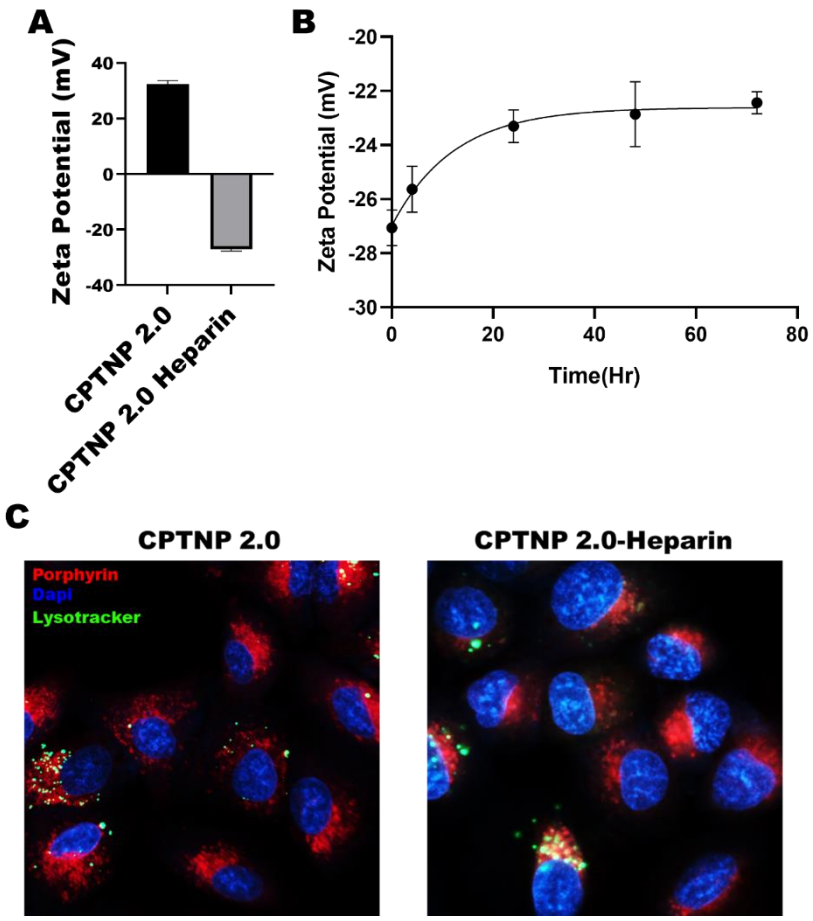

Figure 13. A. Zeta potential of crosslinked CPTNP 2.0s before and after incubation with heparin. **B.** Zeta potential was measured periodically during dialysis of CPTNP after heparin coating. The negative zeta potential is consistent, indicating the coating may persist in vivo. **C.** A549 cells treated with 10µM CPTNP 2.0 and 10µM CPTNP 2.0-Heparin for 24hr. Results are roughly the same between groups; lysotracker signal is disrupted in most cells.

To put the ideas of crosslinking and heparin coating to the test, in vivo biodistribution studies were conducted. Four nude xenograft mice were dosed with 5mg/kg CPTNP-2.0. in three different formulations. An non-crosslinked variant. A

crosslinked variant and a crosslinked variant coated with heparin. 48 hours later, major tissues were excised and imaged for porphyrin using an IVIS system. The un-crosslinked variant had very little tumor or liver uptake; this is likely due to the clearance of the compound. Both the crosslinked and the heparin-coated material had similar tumor uptake, however, the heparin-coated material had slightly less liver uptake. Indicating the heparin coating did indeed lower liver uptake. Combined with additional modifications such as PEGylation, CPTNPs could enjoy prolonged circulation and high tumor specificity.

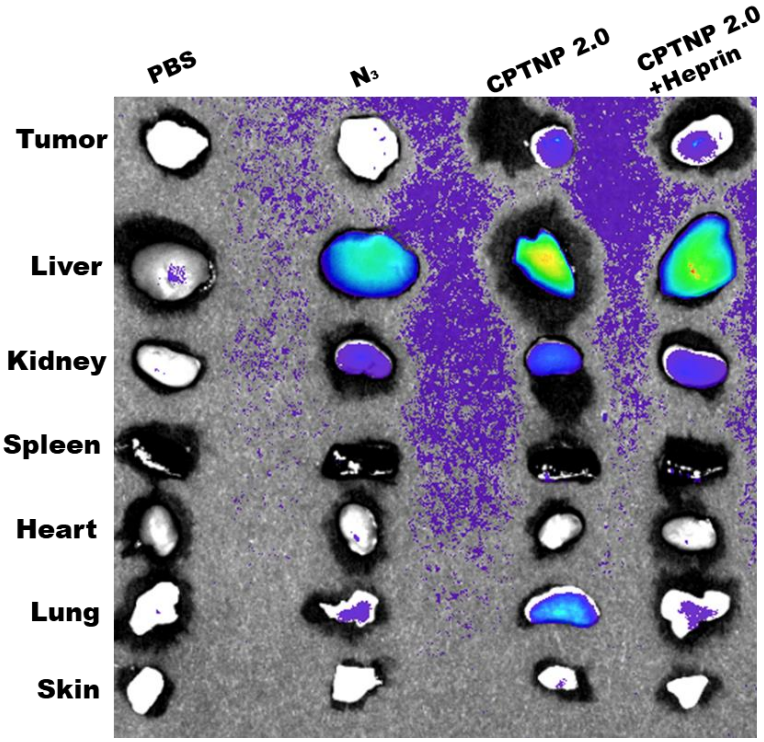

Figure 14: Gross tissue porphyrin fluorescence of animals 48 hours after treatment with 5mg/kg nanomaterial. The imaging indicates the tissue-specific localization of CPTNP 2.0 nanomaterial. PBS controls, while N_3 represents the non-crosslinked material, CPTNP 2.0 represents the crosslinked, uncoated nanomaterial, CPTNP 2.0 + heparin represents the heparin-coated and crosslinked nanomaterial.

3.4. Conclusion

Here we showed that CPTNPs synergizes with cisplatin in vitro by disrupting the lysosomal sequestration of cisplatin in NSCLC cells. When inoculated with CPTNPs, more cisplatin-DNA adducts may be observed. This cisplatin synergism translates in vivo xenograft models, which demonstrate a two-fold increase in survival when compared to CPTNP alone. While weight was modestly affected during the combination CPTNP-cisplatin treatment regime, it quickly recovered after the cessation of treatment. Biochemistry indicated no elevated levels at the end of the study, indicating the treatment was well tolerated at the given dose. While we hypothesized that this effect may be due to the inhibition of autophagic flux as caused by CPTNPs, and we demonstrated that CPTNPs could inhibit autophagic flux in vitro, this effect was not observed in vivo using the subretinal tumor xenograft model in mice and the OCT/SLO optical imaging system. However, modulation of autophagic flux in a tumor xenograft model expressing the GFP-LC3-RFP probe was observed after treatment with a bolus of Hydroxychloroquine, suggesting that a GFP-LC3-RFP system is a valuable tool for the real-time monitoring of autophagic flux in vivo. Finally, we developed a modified version of CPTNPs, which are able to load platinum-based chemotherapies, be reversibly crosslinked, and heparin-coated for improved biodistribution in vivo, with little effect on their LMP activity as evidenced by in vitro assays. Together, the CPTNP platform has a bright future as it is easily modifiable and can sensitize tumors to already existing chemotherapies.

3.5. References

1. Bray, F. *et al.* Global cancer statistics 2018: GLOBOCAN estimates of incidence and mortality worldwide for 36 cancers in 185 countries. *CA. Cancer J. Clin.* **68**, 394–424 (2018).
2. Ettinger, D. S. *et al.* Non–Small Cell Lung Cancer, Version 5.2017, NCCN Clinical Practice Guidelines in Oncology. *J. Natl. Compr. Canc. Netw.* **15**, 504–535 (2017).
3. Roth, J. A. *et al.* Long-term follow-up of patients enrolled in a randomized trial comparing perioperative chemotherapy and surgery with surgery alone in resectable stage IIIA non-small-cell lung cancer. *Lung Cancer* **21**, 1–6 (1998).
4. Chaft, J. E. *et al.* Evolution of systemic therapy for stages I-III non-metastatic non-small-cell lung cancer. *Nat. Rev. Clin. Oncol.* **18**, 547–557 (2021).
5. M., A. F., J., C., C., A. & J., M. P. Cisplatin Biochemical Mechanism of Action: From Cytotoxicity to Induction of Cell Death Through Interconnections Between Apoptotic and Necrotic Pathways. *Curr. Med. Chem.* **10**, 257–266 (2003).
6. Liang, X.-J. *et al.* Trafficking and localization of platinum complexes in cisplatin-resistant cell lines monitored by fluorescence-labeled platinum. *J. Cell. Physiol.* **202**, 635–641 (2005).
7. Safaei, R. *et al.* Abnormal lysosomal trafficking and enhanced exosomal export of cisplatin in drug-resistant human ovarian carcinoma cells. *Mol. Cancer Ther.* **4**, 1595–1604 (2005).
8. Choi, K. S. Autophagy and cancer. *Exp. Mol. Med.* **44**, 109–120 (2012).

9. HonorHealth Research Institute. *A Phase II Study of Paclitaxel Protein Bound + Gemcitabine + Cisplatin+ Hydroxychlororoquine as Preoperative Treatment in Patients With Untreated Resectable, Borderline Resectable and Locally Advanced Adenocarcinoma of the Pancreas*. https://clinicaltrials.gov/ct2/show/NCT04669197 (2020).
10. Li, Y. *et al.* Hydroxychloroquine induced lung cancer suppression by enhancing chemo-sensitization and promoting the transition of M2-TAMs to M1-like macrophages. *J. Exp. Clin. Cancer Res.* **37**, 259 (2018).
11. Abdel Karim, N. F. *et al.* Phase I trial of chloroquine (CQ)/hydroxychloroquine (HCQ) in combination with carboplatin-gemcitabine (CG) in patients with advanced solid tumors. *J. Clin. Oncol.* **37**, 3027–3027 (2019).
12. Kimura, T., Takabatake, Y., Takahashi, A. & Isaka, Y. Chloroquine in Cancer Therapy: A Double-Edged Sword of Autophagy. *Cancer Res.* **73**, 3–7 (2013).
13. Tong, R. & Langer, R. Nanomedicines Targeting the Tumor Microenvironment. *Cancer J.* **21**, 314–321 (2015).
14. Baehr, C. M. *et al.* Transformable amyloid-beta mimetic peptide amphiphiles for lysosomal disruption in non-small cell lung cancer. *Biomaterials* **277**, 121078 (2021).
15. Choi, K. S. Autophagy and cancer. *Exp. Mol. Med.* **44**, 109–120 (2012).
16. Kaizuka, T. *et al.* An Autophagic Flux Probe that Releases an Internal Control. *Mol. Cell* **64**, 835–849 (2016).
17. Zawadzki, R. J. *et al.* Adaptive-optics SLO imaging combined with widefield OCT and SLO enables precise 3D localization of fluorescent cells in the mouse retina. *Biomed. Opt. Express* **6**, 2191–2210 (2015).

18. Zhitomirsky, B. & Assaraf, Y. G. Lysosomes as mediators of drug resistance in cancer. *Drug Resist. Updat.* **24**, 23–33 (2016).
19. Xiao, K. *et al.* The effect of surface charge on in vivo biodistribution of PEG-oligocholic acid based micellar nanoparticles. *Biomaterials* **32**, 3435–3446 (2011).
20. Yang, F. *et al.* One-bead one-compound combinatorial library derived targeting ligands for detection and treatment of oral squamous cancer. *Oncotarget* **10**, 5468–5479 (2019).
21. Zhang, J. Z. *et al.* Facile Preparation of Mono-, Di- and Mixed-Carboxylato Platinum(IV) Complexes for Versatile Anticancer Prodrug Design. *Chem. – Eur. J.* **19**, 1672–1676 (2013).
22. Zhang, L. *et al.* Tumor Receptor-Mediated In Vivo Modulation of the Morphology, Phototherapeutic Properties, and Pharmacokinetics of Smart Nanomaterials. *ACS Nano* **15**, 468–479 (2021).
23. Zhang, L. *et al.* Transformable peptide nanoparticles arrest HER2 signalling and cause cancer cell death in vivo. *Nat. Nanotechnol.* **15**, 145–153 (2020).
24. Matsumoto, H., Miller, J. W. & Vavvas, D. G. Retinal detachment model in rodents by subretinal injection of sodium hyaluronate. *J. Vis. Exp. JoVE* (2013) doi:10.3791/50660.
25. Tallarida, R. J. Quantitative Methods for Assessing Drug Synergism. *Genes Cancer* **2**, 1003–1008 (2011).
26. Qin, L. *et al.* Chloroquine enhances the efficacy of cisplatin by suppressing autophagy in human adrenocortical carcinoma treatment. *Drug Des. Devel. Ther.* **10**, 1035–1045 (2016).

27. Zhao, X. *et al.* Chloroquine-Enhanced Efficacy of Cisplatin in the Treatment of Hypopharyngeal Carcinoma in Xenograft Mice. *PLoS ONE* **10**, (2015).
28. Zhang, L. *et al.* Tumor Receptor-Mediated In Vivo Modulation of the Morphology, Phototherapeutic Properties, and Pharmacokinetics of Smart Nanomaterials. *ACS Nano* **15**, 468–479 (2021).

4. Virus-Like Particles for the Oral delivery of Crispr-Cas9 Ribonucleoprotein

4.1. Introduction

The clustered regularly interspaced short-palindromic repeat (CRISPR)-associated protein 9 (CRISPR-Cas9) nuclease system is a promising tool utilized in a sweeping range of biomedical applications.[1,2] known in the popular imagination as “molecular scissors”, the CRISPR-Cas9 system utilizes a single guide RNA to direct the Cas9 enzyme to a complementary portion of DNA where a double-strand break may be induced. Double strand breaks may be repaired through homology-directed repair via template DNA or error-prone non-homologs end-joining, often resulting in deletions/additions and thereby gene knockout (KO). Despite the promise of the Crispr-Cas9 system, the delivery of gene-editing tools to adult tissue remains a challenge.

Moreover, many heritable diseases of the GI tract, including chronic inflammatory diseases such as Crohn‘s disease and ulcerative colitis, as well as familial adenomatous polyposis are poorly managed by contemporary treatments. CRISPR-Cas9 gene therapy offers promising solutions to these diseases in theory; however, to date, there is no system capable of delivering CRISPR-Cas9 gene-editing tools to somatic gut tissue.

Cas9 ribonucleoproteins (RNPs) offer distinct advantages to other gene-editing systems due to their low risk for insertional mutagenesis, production capacity, quick DNA cleavage activity, and relatively limited off-target activity.[3–5] However, as proteins,

RNPs are susceptible to digestion if delivered orally. Therefore, a vehicle capable of delivering RNPs to the intestinal epithelia is needed.

The discovery of Hepatitis E virus began with the Soviet invasion of Afghanistan in 1983. A group of soldiers had become ill with what was supposed to be a strain of hepatitis. However, the source of the infection could not be identified. So, a healthy volunteer with a serological history of hepatitis A ingested a pooled fecal sample from the infected soldiers, and the novel virus was identified from his stool. And thus Hepatitis E was discovered.[9]

Holland Cheng's group has developed Virus-like particles (VLPs) for the delivery of nucleic acids to the intestinal tissue.[6] Previously, this system has been used to deliver orally available plasmid vaccine and IV treatment of breast cancer. [6–8]

The virus-like particles derived from Hepatitis E were first studied by Dr. Cheng in the late 1990s and are modified from native HEP E virus truncated to just 500 Amino acids leaving a slightly smaller capsid, 27nm vs. 32nm for native HEP- E.[10] The capsid protein consists of important three domains, the middle and shell domains play an important structural role while the protrusion domain plays a role in dimerization, host cell receptor recognition.

The HEVNP platform exhibits broad tropism and are able to transfect a wide range of cells; previously Dr. Cheng's group has transfected a broad range of cell lines with plasmid-loaded HEVNPs. Cell lines include Vero, kidney epithelial cells, Hela, immortalized cancer cells, 3T3 mouse fibroblasts, HEP-G2 immortalized hepatocyte cells, and others.

Dr. Cheng's group has previously demonstrated the encapsulation of a number of different cargo, including plasmid and single-stranded DNA, Q dots for fluorescent detection, and ferrite particles for magnetic resonance imaging. Coupled with the ability to easily and quickly attach peptide ligands, HEVNP becomes an attractive platform for the oral delivery of cargo.[6,7]

Here in conjunction with the National Institute of Health's (NIH) Somatic Cell Genome Engineering (SCGE) initiative we develop Virus-like particles capable of delivering CRISPR-Cas9 RNPs to the small intestine and colon of adult mice via oral delivery. These findings are the first example of gene editing in an adult mouse given orally. Utilizing the hepatitis E VLP previously characterized by the Cheng group,[6] the platform performs with high editing efficiency and promising delivery characteristics.

4.2. Methods

RNP Preparation

All work surfaces, gloves, pipettes, tip boxes, ice boxes and other surfaces were sprayed liberally with RNAseaway, and without touching additional surfaces, supplies were moved into a sterile biosafety cabinet or laminar flow hood. 6.5mg/mL stock streptococcus pyogenes cas9 (24.92uL/nMol) was combined into a single RNAse free PCR tube (cas9 stock tubes may be used if desired) using a filtered RNAse free pipette tip. Next, the gRNA was added to the combined spCas9 at a 1.1:1 molar ratio, gRNA:spCas9. We carefully pipetted up and down until the solution mixed thoroughly and became clear. A cloudy solution of what is likely cas9:gRNA colloids can form when there is insufficient local RNA. We then allow the solution to stand at room temperature for 5 minutes. Meanwhile, we added SUPERase•In RNase inhibitor (Thermo Fisher:

AM2694) to the HEVNP monomer solution at a 1:20 dilution; inhibitor: final fluid volume of encapsulation run**.** We then ensured that the RNP solution was clear and added it to the HEVNP monomer solution for encapsulation using filtered RNAse free tips. If the RNP solution is not clear, we added an additional one nMol of RNA and allowed it to stand for an additional 5 minutes.

Peptide synthesis and surface conjugation

Peptides were synthesized via solid-phase peptide synthesis using standard fluorenylmethyloxycarbonyl (Fmoc) chemistry and ethyl cyano(hydroxylamine)acetate (Oxyma)/1,3-diisopropylcarbodiimide (DIC) coupling as described in previous publications.[11] Rink amide MBHA resin (loading 0.503 mmol/g, P3 BioSystems, Louisville, KY) was used as solid support. A 6-fold molar excess of Fmoc-protected amino acids to resin was used for coupling. The reaction was monitored with ninhydrin test. The Fmoc group was de-protected with 20% 4-methylpiperidine in N,N-dimethylformamide (DMF) (first 5 min, then 15 min). After the last cycle of amino acids coupling and Fmoc-deprotection, the linear biotinylated peptide was cleaved with a trifluoroacetic acid (TFA) cocktail containing 90% TFA, 5% thioanisole, and 5% H_2O. The liquid was collected and precipitated in cold -20ºC diethyl ether and subsequently washed 3 times. The powder was re-dissolved in a small amount of 50% ACN/water and analyzed by reversed-phase high-performance liquid chromatography (RP-HPLC) on a preparative Vydac C18 column. The purity was determined to be >95%. The identities of peptides were confirmed Matrix-Assisted Laser Desorption/Ionization-Time of Flight (MALDI-TOF) and ^1H Nuclear Magnetic Resonance (NMR) using a 400 MHz Bruker spectrometer.

In vitro delivery of cas9 RNPs and imaging

HT29 cells acquired from American Type Culture Collection (ATCC) were cultured in Dulbecco's Minimum Eagle medium (DMEM) supplemented with 10% FBS and penicillin and streptomycin. Cells were plated in an eight-well Ibidi µ-plate. Cells were treated with RNP-loaded HEVNPs, RNP alone or control. Samples were then fixed for 10 minutes in 4% paraformaldehyde in PBS. Samples were then washed three times with PBS, membrane permeabilized with Triton-X, and blocked with 10% BSA. Samples were then stained with anti-Cas9 antibody (Sigma ABS2202 and secondary antibody conjugated with Alexa fluor 555. Samples were then imaged via an LSM 800 Zeiss confocal microscope.

Ai9 Cell imaging

A 5 week old female Ai9 mouse was euthanized using 5% isofluorane as an anesthetic followed by cervical dislocation. Liver tissue was removed and minced in a biosafety cabinet using two sterile scalpels. Once minced to a fine paste, the tissue sample was incubated in an enzyme solution consisting of collagenase, dispase, and hyaluronidase, for four hours at 37ºC with agitation. Next, the slurry was strained through a 100µm nylon mesh (Thermo Fischer 352360) and then diluted with PBS and washed three times via centrifugation. Cells were then plated on a six well plate with Williams E medium supplemented with insulin, transferrin and selenium (Sigma I3146), 5% FBS and penicillin, and streptomycin. Cells were incubated at 37ºC for at least 48 hours before treatment.

Cells were treated with various concentrations of RNP-HEVNP, RNP-CrisprMax, or control, then observed for TD-Tomato expression 48 hours after treatment on an LSM 800 Zeiss confocal microscope.

Flow cytometry

eGFP expressing HEK cells were acquired from genetarget and cultured in Dulbecco's minimum essential media, supplemented with 10% fetal bovine serum alongside penicillin and streptomycin. GFP knockout sequence was derived from Cong et al.[12] RNPs were formed by combining 1.1:1, gRNA:spCas9 in all cases. Cells were plated on a six-well plate, and three wells were treated with the lipofectamine product Crispr max loaded with RNP, HEVNP-RNP, and negative control. 48 hours after treatment, cells were detached from the plate via 5% trypsin. Once harvested, cells were washed twice with PBS using a microcentrifuge, 200xGs. Cells were then passed through a 40µm nylon mesh filter and fixed in 1% paraformaldehyde for 10 minutes and subsequently washed twice in PBS. Cells were again filtered through a 40µm filter, and fluorescence was observed on a desktop guava flow cytometry unit. Debris and cell doublets were excluded using the forward and side scatter.

Dosing and treatment

Feed was removed from mice 16 hours before the intended dosing time. Mice were quickly anesthetized with 1% isoflurane. Then 0.3mL of HEVNP or other solutions were administered orally via disposable polypropylene gavage tips. Mice were fasted for an additional 4 hours after treatment to ensure adsorption of the material, after which time feed was replaced. Mice were euthanized by 5% isoflurane followed by cervical dislocation. After which time tissues were harvested.

Cryosectioning

Tissues were harvested from Ai9 mice and washed; in the case of solid organs, the tissue was washed in ice-cold phosphate-buffered saline (PBS); in the case of intestinal tissues, the tissue was repeatedly flushed with PBS solution then cut longitudinally and Swissrolled.[13] Briefly, once cut longitudinally, the tissue is wrapped around a glass dowel from proximal to distal, such that a compact region containing much of the tissue may be seen. Once washed, the tissues are immersed in 4% paraformaldehyde for 16hr or overnight. The tissues are then submerged in 30% sucrose in PBS solution for 24 hours. The tissue is then placed in a block mold and submerged in optimal cutting temperature (OCT) solution (Thermo Fisher 23-730-571). The tissue may then be cut into 10 µm thick slices and fixed onto poly-L-lysine coted slides. The tissue slices are allowed to thaw and dry at room temperature for 15 minutes, after which time they are washed in PBS 3 times, five minutes each wash. The samples may then be stained with Hoecesht 3332232, for 15 minutes. Subsequently, the tissues are washed three times in PBS, for five minutes each, with a final wash in ultrapure water. 10 µL of 70% glycerol solution is then deposited onto the slide, and a coverslip is mounted and sealed with clear nail polish. The sample is allowed to dry and is imaged on a Zeiss LSM 800.

4.3. Results and Discussion

When considering CRISPR Cas9 cargo, several options were discussed among the team. Plasmids were an attractive option due to their high stability and ease of production. However, the size limitation of HEVNP plasmid cargo was too small (~7kbp) to accommodate available cas9 plasmids with the appropriate guide RNAs. mRNA was

also considered; however, achieving the quantities needed for oral administration proved difficult. These two cargo also have known challenges with off-target activity and higher risk for insertional mutagenesis. Our group was highly interested in RNPs as a solution to these challenges, as it could be acquired in mmole quantities and offered other distinct advantages such as low risk for insertional mutagenesis, production capacity, quick DNA cleavage activity, and relatively limited off-target activity.[3–5]

To determine the capacity for HEVNP encapsulation of spCas9 RNPs, we used a cryo-EM density map to demonstrate the ability of spCas9 RNP to fit in the HEVNP capsid. The N-terminus residues of HEVNP monomer's shell domain are composed of 10+ positively charged residues that can capture the negatively charged RNA and Cas9 enzyme. We have optimized the procedure of CRISPR/Cas9 encapsulation by disassembly of HEVNP using reducing agents, the introduction of the Cas9/RNA complex (RNP), and gradual reassembly by adding Ca+ ions – the internal cavity of HEVNP is about 120Å, and the long-axis diameter of RNP is about 110Å. Our cryo-EM density map with a resolution of 2.8Å reveals Ca+ ion at the center of the 3-fold axis of the M domain, stabilized by three glutamic acids (E417) (C) – the removal and re-

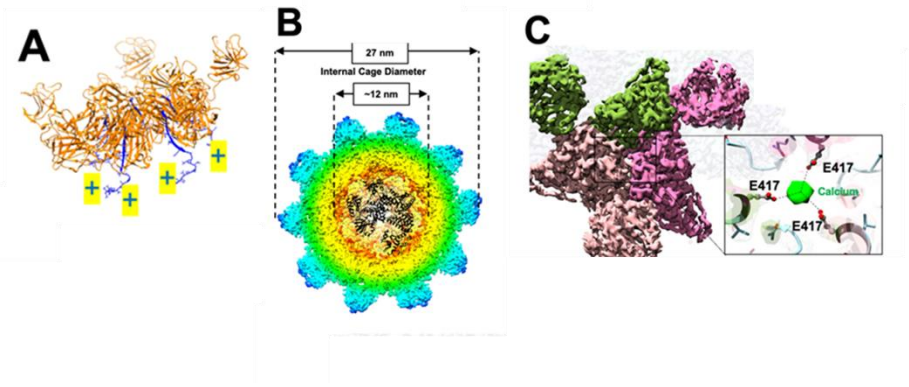

introduction of Ca+ will result in disassembly and reassembly of HEVNP, respectively.

Figure 1. A. A pentamer subunit of HEVNP (composed of 12 pentamers) with the positive tails of the N-terminus is highlighted in blue. These results facilitate the encapsulation of negatively charged cargo – such as DNA, RNA, or CRISPR enzyme. **B.** An illustration of HEVNP w/ Cas9 enzyme encapsulated (black). The diameter of HEVNP is 27 nm – its interior cavity is about 12 nm. **C.** The 2.8Å density map of HEVNP reveals a calcium ion sitting in the center of the 3-fold axis, stabilized by glutamic acid 417 from each subunit colored in green, pink, and orange. The removal of this calcium ion by reducing agents such as DTT or EGTA will result in the disassembly of HEVNP.

To validate the loading of Cas9 RNPs in HEVNPs, we incubated 1nmole RNP coupled with modified single guide RNA (sgRNA, 2'O-Methyl at first three and last bases, 3' phosphorothioate bonds at first three and last two bases) with 1nmole HEVNP and proceeded with our standard encapsulation procedure. Briefly, purified HEVNP were treated with EGTA, and monomers were isolated through size exclusion chromatography. Subsequently, the HEVNP monomers were incubated with cargo, RNP, and Ca^{2+} was added to the aqueous solution, thereby inducing HEVNP formation and encapsulation of the RNPs. Later the particles were passed again through size exclusion chromatography. Upon inspection via dynamic light scattering and transmission electron microscopy, particles were found to be the appropriate size

(~23nm). To determine if RNPs were encapsulated, the material was subjected to a denaturing bis-tris protein blot (NuPAGE™ 4 to 12%, Bis-Tris pre-cast gel). After staining with Simply Safe Coomassie blue stain, Cas9 and HEVNP monomer bands may be seen clearly, indicating that spCas9 is encapsulated in HEVNP. It should be noted that the HEVNP band is relatively larger than the spCas9 band. This is due to the fact that there are 64 copies of HEVNP monomer subunits, or 12 copies of HEVNP pentamer subunits per virus-like nanoparticle, whereas there is one copy of spCas9 per nanoparticle.

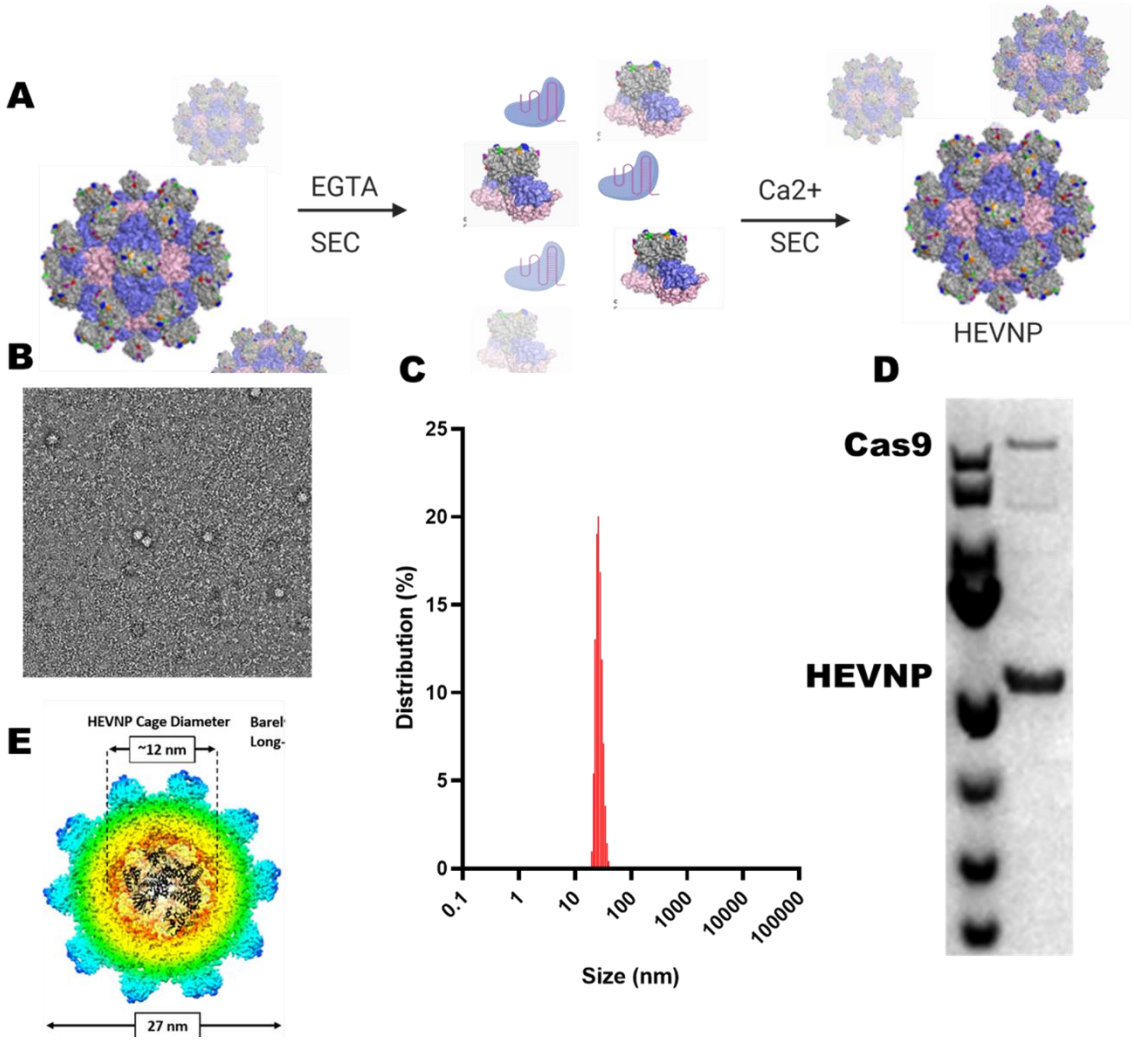

Figure 2: A. Skema represents the HEVNP encapsulation process. **B.** TEM of HEVNP nanomaterial. **C.** DLS of HEVNP size distribution. **D.** A protein blot in 4-12% bis-tris gel, stained with simply safe Coomassie blue stain. The sample is purified RNP-loaded HEVNP. Bands are indicative of Cas9 (162kDa) loading in HEVNP (64kDa), suggesting successful encapsulation.

Prime editors, as developed by the Liu group, have generated significant interest in recent years.[14] Prime editors are capable of inserting arbitrary DNA sequences into the genome with single-nucleotide precision and high efficiency compared to methods using donor DNA. As discussed above, RNPs are the preferred Cas9 format for increased efficiency in vivo editing. Other groups have demonstrated prime editing RNP efficiency in zebrafish,[15]; however, more complex delivery systems are needed for in vivo mammalian delivery.

We were interested to see if larger Cas9 platforms could be encapsulated in HEVNP; we, therefore, contracted with the macrolab facility at UC Berkely and procured purified prime editor 2 protein. Prime editors consist of spCas9-nickase linked to reverse transcriptase. In conjunction with a prime editor guide RNA (pegRNA) the prime editor is capable of instilling all 12 nucleotide substitutions for up to 44 base pairs without

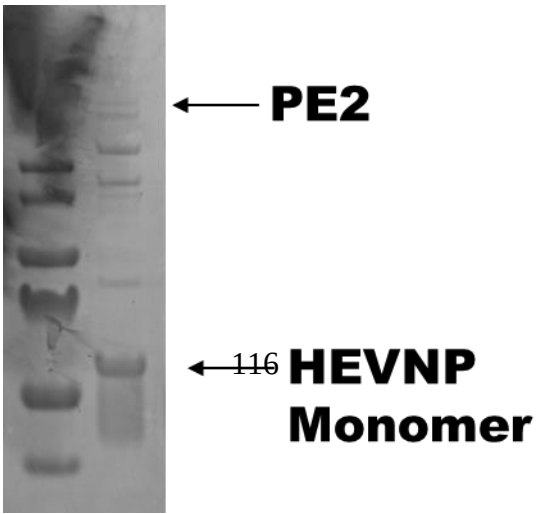

double-strand breaks or donor DNA, making it a powerful therapeutic tool. We, therefore, encapsulated prime editor RNPs using the HEVNP platform and validated their encapsulation using a protein blot and Coomassie blue stain. PE2 RNP and HEVNP bands can be seen here, suggesting the HEVNP system can encapsulate the larger PE2 RNP. A similar coomassie blue stain was conducted to validate the loading.

Figure 3: A protein blot in 4-12% bis-tris SDS-gel, stained with simply safe Coomassie blue stain. The sample is purified RNP loaded HEVNP. Bands are indicative of Prime-Editor loaded in HEVNP, suggesting successful encapsulation. Fragments below PE2 are likely the result of Cas9-Reverse transcriptase linker cleavage, leaving behind a cas9 with a smaller molecular weight. The HEVNP monomer subunit appeared as a single band at 64kDa

---

Before proceeding to editing studies, we desired to determine the ability of HEVNP to deliver spCa9 to the nucleus of target cells. HT29 human colon cancer cell line was acquired and culture with DMEM, 10% FBS and penicillin/streptomycin. Cells were then treated with RNPs alone, RNP loaded HEVNP and no treatment for 48hrs. Cells were then fixed in 10% paraformaldehyde for 10 minutes, then washed and stained with Hoechst 33342. The samples were subsequently stained with anti-Cas9 antibody (sigma, ABS2202) and secondary anti-rabbit Alexa fluor 555. In the case of no treatment, no Cas9 signal was observed. In the case of RNP alone, Cas9 signal around the surface of treated cells was seen. When encapsulated in HEVNP, Cas9 was

observed in the nucleus of treated cells. This suggested that HEVNP were capable of delivering spCas9 to the nucleus, which could edit the genome in vitro.

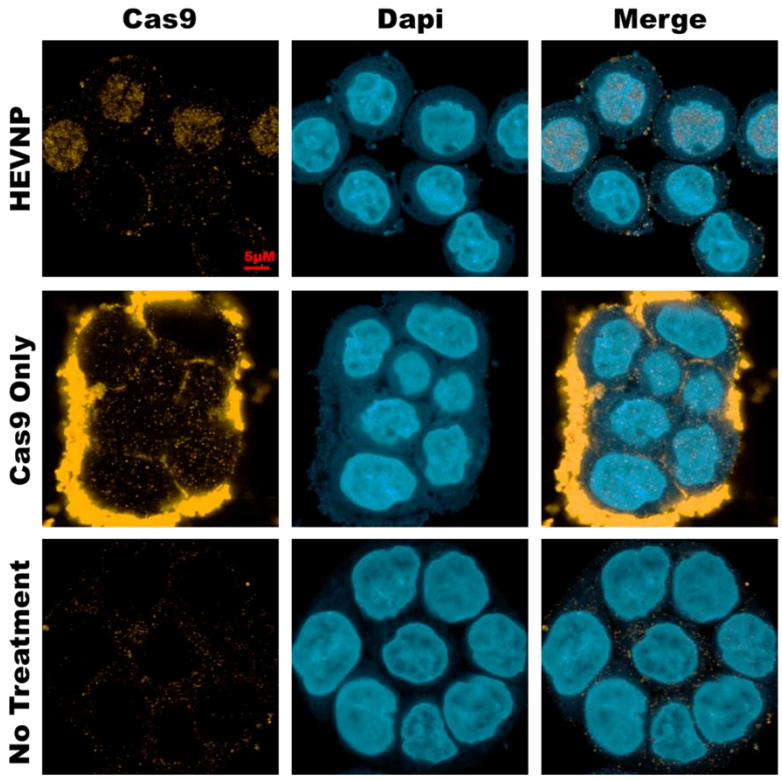

Figure 4: HT29 colon cancer cells treated with RNP loaded HEVNP, Cas9 RNP alone, or no treatment. Samples were immunofluorescence stained with anti-Cas9 antibody and subsequently DAPI. Imaging reveals Cas9 was delivered via HEVNP to the nucleus but Cas9 alone was found to remain at the exterior of the cell cluster.

To test the ability of RNP-loaded HEVNP to edit cells in vitro we procured HEK 293 cells stably expressing GFP and the parent cell line (no GFP expression). We then procured a GFP targeted gRNA sourced from Synthego derived from Cong et al.[12] We

dosed GFP expressing HEK cells with RNP encapsulated in either CRISPRmax, a commercially available lipid nanoparticle similar to lipofectamine, HEVNP, or no treatment. Events meeting forward scatter and side scatter quality standards were grouped, and the number of GFP + cells were enumerated using a guava desktop flow cytometer. We found that in the CRIPRmax case, 35.5% were GFP negative, while in the HEVNP case 39.7% were GFP negative, indicating that HEVNP were capable of enabling delivery of Cas9 RNP and gene editing in HEK cells with reasonable efficiency.

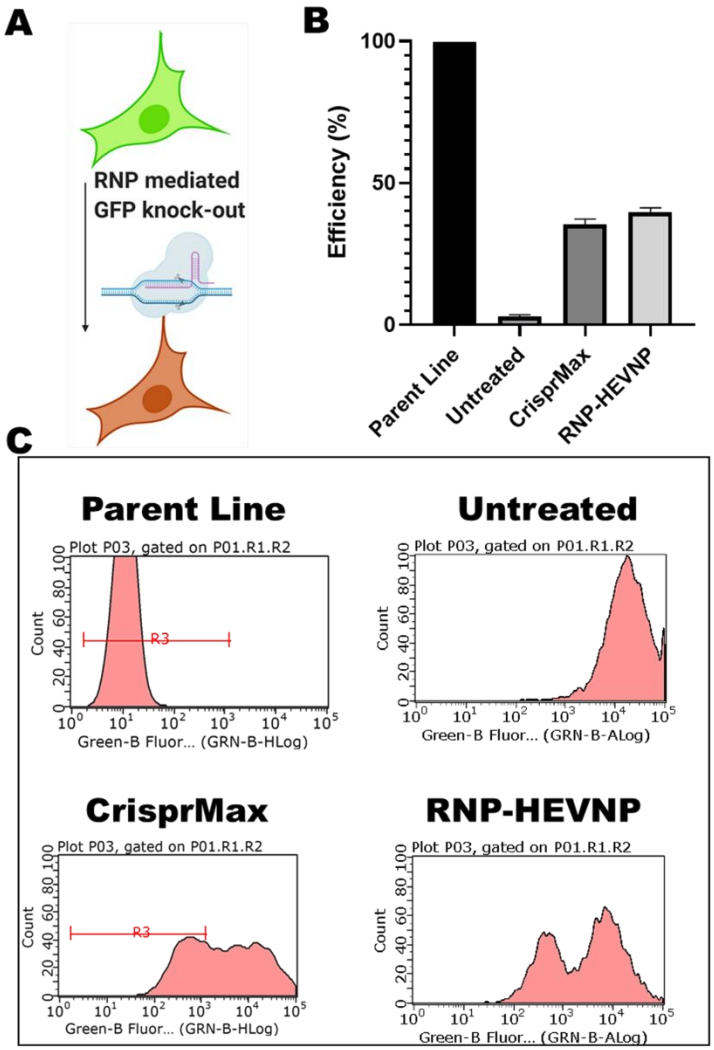

Figure 5: A. Basic schematic of Crispr-GFP knockout mechanism for the exploration of RNP efficiency. **B.** Gene editing efficiency as measured by the percentage of GFP negative cells. The parent cell line represents HEK cells that do not express GFP, Untreated represents untreated HEK cells expressing GFP. Crispr-max represents treatment with the same RNP as used in HEVNP encapsulation, but with the lipofectamine product, Crispr-max. RNP-HEVNP corresponds to RNP-loaded HEVNPs. Values were the result of three flow cytometry readings from three separate wells. **C.** Representative flow cytometry results from all trial groups.

GFP knockdown is a strong method for the determination of the platform efficiency; however, GFP negativity is difficult to visualize and quantitate *in vivo*. Therefore, a positive signaling platform was needed for in vivo testing of the platform. Ai9 and Ai14 model systems are commonly used as in vitro and in vivo editing reporters. The Ai9 model consists of a promotor, followed by a floxed stop codon, and subsequently the fluorescent probe Tandom Tomato (TdTomato). When the sequence is exposed to Cre recombinase or two cas9s armed with gRNA targeted to either side of the stop codon, the stop codon is excised, and the promoter is recombinated to proceed the TdTomato sequence, allowing for TdTomato expression directly. The TdToamto may then be imaged via microscopy or other optical methods.

To validate Crispr delivery in vitro, primary hepatocytes were derived from an Ai9 mouse. Briefly, the mouse was euthanized, the liver was quickly excised and finely diced before being subject to collagenase and dispase for 4 hrs. The solution was then

strained through a 40μM nylon cell strainer then washed in PBS 2X, and centrifuged at 140Xg. Primary liver culture cells were grown in Williams E media, supplemented with ITS, 5%FBS, and penicillin/streptomycin. Cells were treated with both RNP-loaded HEVNP, RNP CRISPRmax and no treatment. Both systems utilized two gRNAs targeting the left and right of the stop codon. Both the RNP solution and CRISPR max solution induced TdTomato expression. Both the Crisprmax system and RNP-loaded HEVNP induced TdTomato expression. Subsequently, the samples were fixed using 4% PFA, and imaged on a confocal scanning laser microscope (Zeiss, LSM 700). TdTomato expression can be seen in the case of treatment with both CrisprMax systems and RNP-loaded HEVNP, indicating HEVNP are capable of editing Ai9 systems.

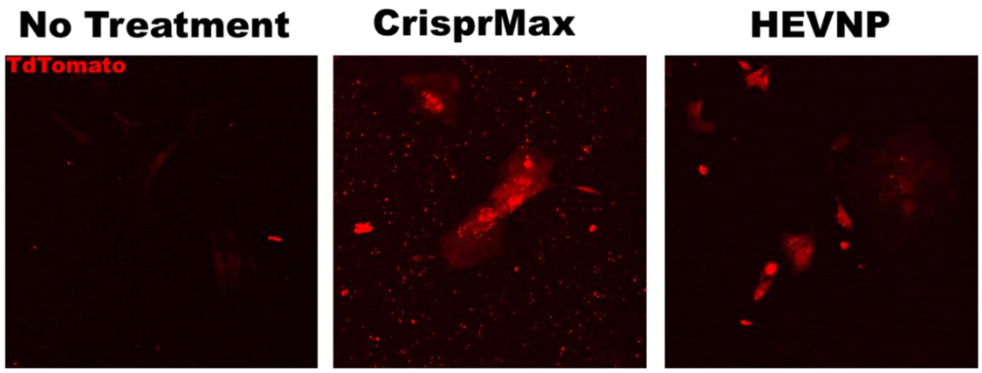

Figure 6: Primary Ai9 liver cells treated with both CrisprMax and RNP loaded HEVNP. TdTomato can be seen in the CrisprMax and HEVNP case but not in the control, indicating cells were edited by CRISPR-Cas.

Later the SCGE consortium small animal testing center (SATC) at Baylor generated a modulated Ai9 strain (modAi9) which required only a single guide RNA to excise the Ai9

stop codon. We procured mouse embryonic fibroblasts from the Small Animal Testing Center, and tested our HEVNP system. This system proved to be much more efficient when compared to the original Ai9 system and offers a promising new delivery detection platform.

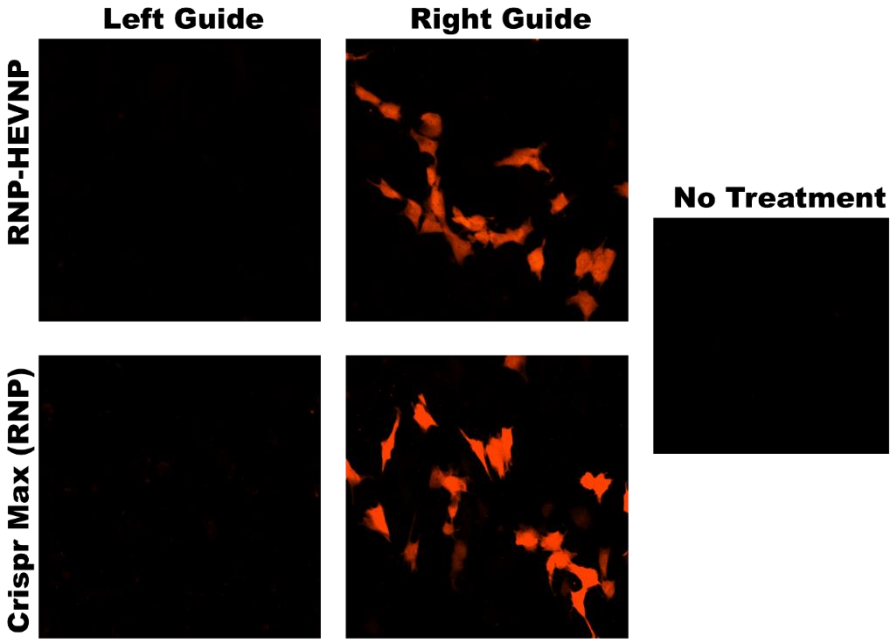

Figure 7: RNPs were prepared in two different formulations, one with a left guide and one with a right guide. As this model system only utilizes the right guide, the left guide served as a negative control in both cases. TdTomato expression was induced by the right guide in both cases, indicating cells were edited by RNP-HEVNP and crisprmax systems.

To test the delivery of HEVNP in vivo, HEVNP were loaded with a plasmid encoding for GFP expression. Mice were dosed with 2 mg/kg HEVNP via oral gavage. After 48 hours, intestinal tissues were harvested and “Swiss rolled” as described in the literature.[13] Briefly, the intestine is cut lengthwise to expose the lumen, and the tissue is rolled on itself from the proximal to distal tissue on a small glass dowl. The tissue is then fixed for 24 hr in PFA and stored in 70% EtOH. Subsequently, the tissue was stained via IHC for GFP expression. GFP expression was observed in the jejuneal crypt of treated mice. A very promising development as the intestinal crypt harbors the stem cells of the intestinal epithelium. If stem cells can be edited by the CRISPR Cas9 system, durable therapeutic outcomes may be possible with the HEVNP system.

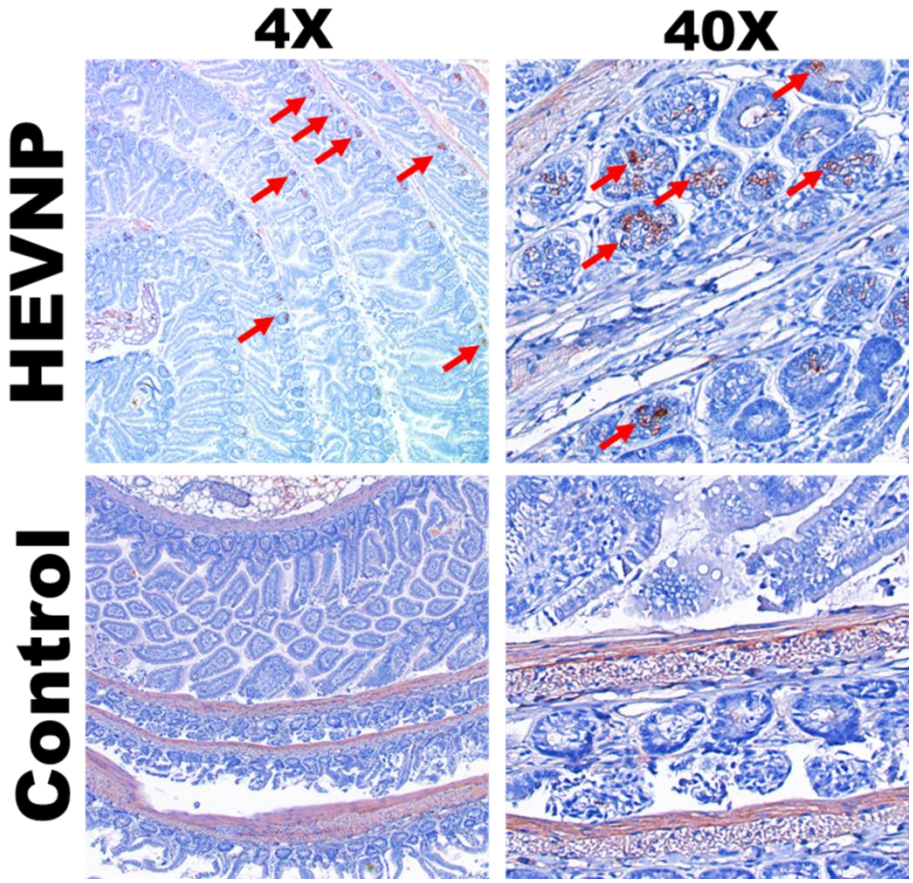

Figure 8: Mouse small intestinal Swiss rolls 48 hours after oral treatment with GFPexpressing plasmid. Micrographs depict hemoxylin stained tissue with IHC for GFP. Red arrows indicate IHC positive cells, showing that Plasmid-HEVNP are capable of transfecting the crypts of C57BL 6 mice.

To test the system in vivo, we acquired four Ai9 expressing mice and each of them orally with four separate regimes: (1) a single dose of equal molar quantities of RNP loaded HEVNP containing the Ai9 right and left guide (1nmole total dose), (2) regimen similar to the first regimen except that the HEVNPs were surface modified with polyarginine, (3) controlForty eight hours after the cessation of treatment, the mice were sacrificed and organs excised. The small intestine was cut into thirds, and Swiss rolled; the same was performed with the colon. The liver, kidney, spleen, heart, lungs were also excised and washed, and fixed in PFA. If the tissue was meant to be cryosection, it was further saturated with sucrose before embedding in OCT liquid. 10µm tissue slices were allowed to dry onto cleaned glass slides, the OCT embedding media was washed off in three rinses of PBS, and the samples were stained with Hoechst 33342. Tissue slices were embedded in 50% glycerol solution and imaged with confocal microscopy.

TdTomato signal was observed in the crypts of the small intestine and colon in all samples, although more crypts had positive signals in the mice treated with higher dose regime. Additional signal was seen in the liver and heart tissue relative to the control. This result is indicative of RNP-mediated genome editing via orally delivered HEVNP. The staining pattern was surprising but is consistent with both the reported literature of

HEVNP delivery and native hepatitis E infection. Previous imaging,[6] and imaging reported in this article describe that plasmid-loaded HEVNP transfect the crypts of the small intestine. Indeed, native hepatitis E virus has been known to replicate in the small intestine, liver, kidney, and spleen, and negative-sense RNA (suggesting HE viral infection) has even been detected in the cerebral spinal fluid of hepatitis E infected patients. Although we did not initially expect HEVNP transfection in cardiac tissue, perhaps it is not surprising as the native virus is very promiscuous.

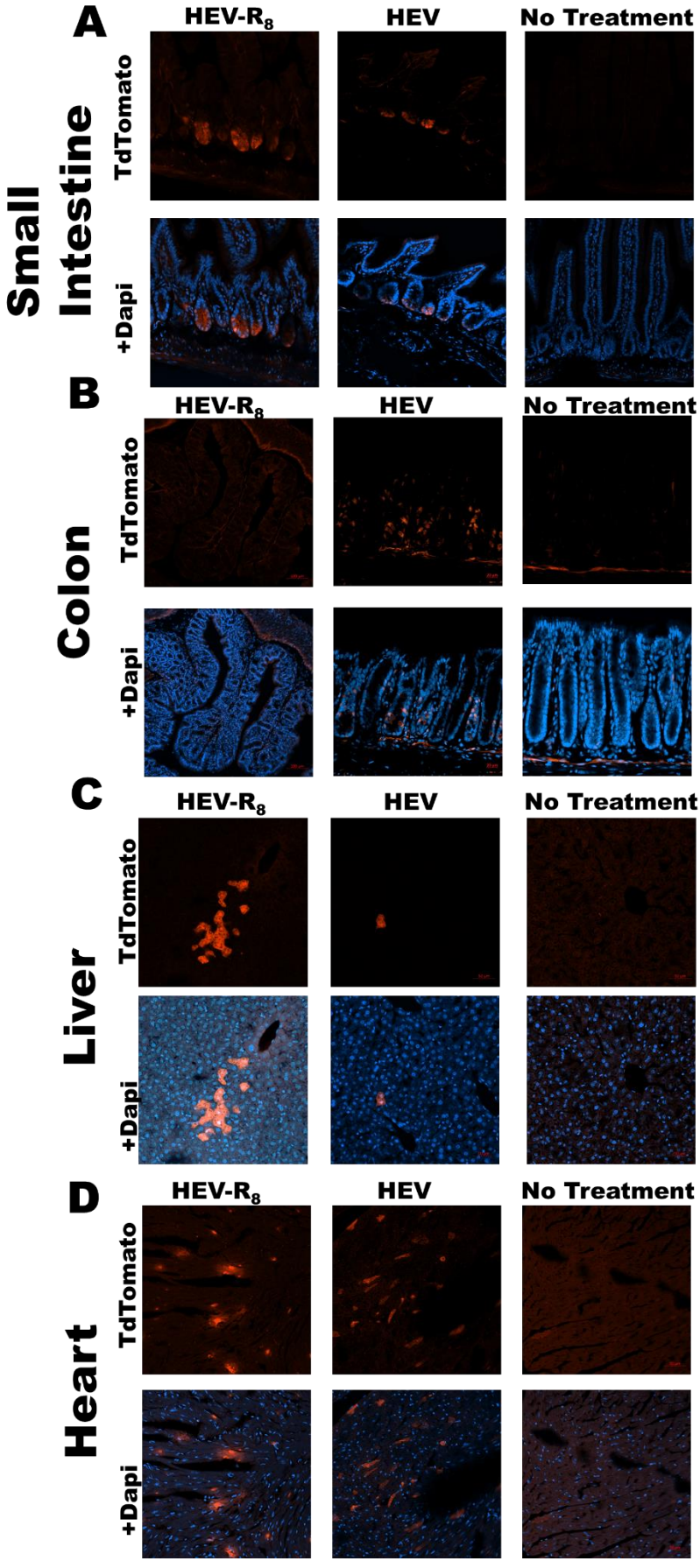
A
HEV-R8
HEV
No Treatment
Small Intestine
TdTomato
+Dapi
B
HEV-R8
HEV
No Treatment
Colon
TdTomato
+Dapi
C
HEV-R8
HEV
No Treatment
Liver
TdTomato
+Dapi
D
HEV-R8
HEV
No Treatment
Heart
TdTomato
+Dapi

Figure 9: A. TdTomato expression in the small intestine after treatment with polyarginine labeled -RNP loaded HEVNP, RNP-HEVNP or PBS. TdTomato expression was seen in the crypts of the small intestine. **B.** Colon slices of the same mice, expression was seen with HEVNP but not polyarginine-HEVNP. **C.** Liver cryosections of the same mice TdTomato expression was seen in the liver of treated mice. **D.** Cryosections from heart tissue of treated mice imaged for TdTomato.

We were interested in validating the visual TdTomato signal visualized in figure 9. To do so, we dosed an additional three mice with 3nmole of either oral RNP-HEVNP, IV RNP-HEVNP, or no treatment. We then resected the tissues of these mice and reserved a portion for amplicon sequencing. A small but significant difference can be observed in the oral dose mouse but not the other two conditions, indicating that editing was successful.

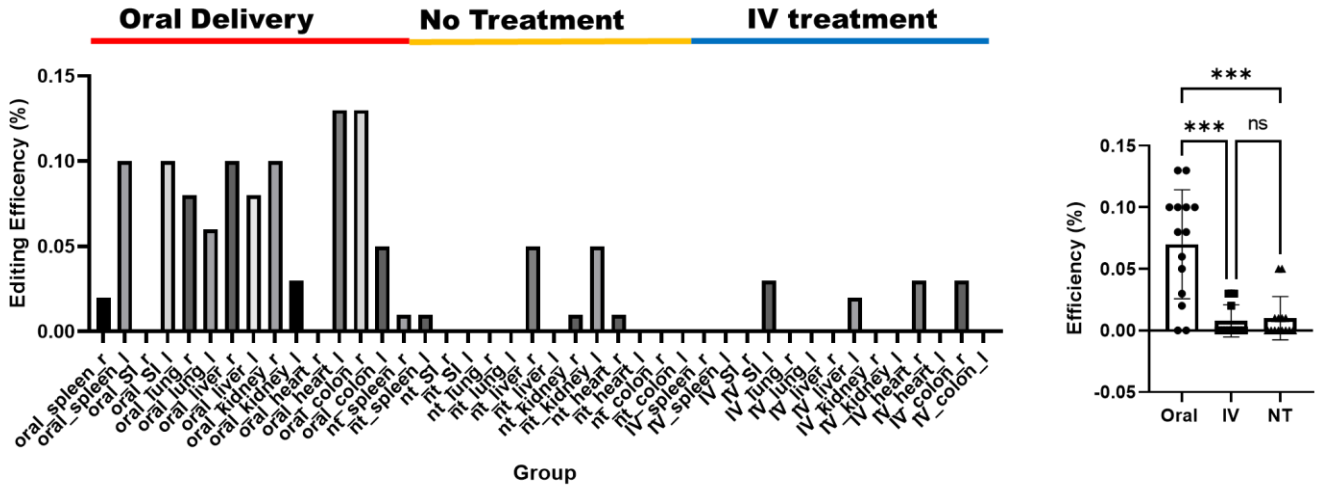

Figure 10: Amplicon sequencing of right and left gRNA targets. And subsequently average values for all tissues combined.

4.4. Conclusion:

Here we have developed the first orally stable Crispr Cas9 delivery system using hepatitis E virus-like particles. Not only is this system orally stable but the system encapsulates CRIPSR-Cas9 ribonucleoprotein, which have higher editing efficiencies, and an improved safety profile when compared to plasmid or mRNA systems. We show that this HEVNP delivery system is capable of effecting gene editing in a reporter system, in vitro and in vivo after oral administration, in the small intestine, the colon, the liver, and the heart. Moreover, we have demonstrated that prime editors may be encapsulated into HEVNP systems. As prime editors are the largest Cas9 editing system to date, It, therefore, stands to reason that nearly any Cas9 based RNP system may be encapsulated into the HEVNP system. This is an exciting advance for the treatment of genetic diseases of the gastrointestinal system.

4.5. References

1. Musunuru, K. *et al.* In vivo CRISPR base editing of PCSK9 durably lowers cholesterol in primates. *Nature* **593**, 429–434 (2021).
2. Koblan, L. W. *et al.* In vivo base editing rescues Hutchinson–Gilford progeria syndrome in mice. *Nature* **589**, 608–614 (2021).
3. Li, L., He, Z.-Y., Wei, X.-W., Gao, G.-P. & Wei, Y.-Q. Challenges in CRISPR/CAS9 Delivery: Potential Roles of Nonviral Vectors. *Hum. Gene Ther.* **26**, 452–462 (2015).
4. Liu, J. *et al.* Efficient delivery of nuclease proteins for genome editing in human stem cells and primary cells. *Nat. Protoc.* **10**, 1842–1859 (2015).

5. Yin, H., Kauffman, K. J. & Anderson, D. G. Delivery technologies for genome editing. *Nat. Rev. Drug Discov.* **16**, 387–399 (2017).
6. Kamita, S. G., Baikoghli, M. A., Maza, L. M. de la & Cheng, R. H. *A Noninvasive, Orally Stable, Mucosa-Penetrating Polyvalent Vaccine Platform Based on Hepatitis E Virus Nanoparticle*. *Synthetic Biology - New Interdisciplinary Science* (IntechOpen, 2019). doi:10.5772/intechopen.86830.
7. Chen, C. C., Stark, M., Baikoghli, M. & Cheng, R. H. Surface Functionalization of Hepatitis E Virus Nanoparticles Using Chemical Conjugation Methods. *J. Vis. Exp. JoVE* 57020 (2018) doi:10.3791/57020.
8. Cheng, R. H. Hepatitis E Nanoparticle: A Capsid-Based Platform for Non-Invasive Vaccine Delivery and Imaging-Guided Cancer Treatment. *Adv. Res. Gastroenterol. Hepatol.* **9**, (2018).
9. Balayan, M. S. *et al.* Evidence for a virus in non-A, non-B hepatitis transmitted via the fecal-oral route. *Intervirology* **20**, 23–31 (1983).
10. Biological and immunological characteristics of hepatitis E virus-like particles based on the crystal structure | PNAS. https://www.pnas.org/content/106/31/12986.short.
11. Yang, F. *et al.* One-bead one-compound combinatorial library derived targeting ligands for detection and treatment of oral squamous cancer. *Oncotarget* **10**, 5468–5479 (2019).
12. Cong, L. *et al.* Multiplex genome engineering using CRISPR/Cas systems. *Science* **339**, 819–823 (2013).

13. Bialkowska, A. B., Ghaleb, A. M., Nandan, M. O. & Yang, V. W. Improved Swiss-rolling Technique for Intestinal Tissue Preparation for Immunohistochemical and Immunofluorescent Analyses. *JoVE J. Vis. Exp.* e54161 (2016) doi:10.3791/54161.
14. Anzalone, A. V. *et al.* Search-and-replace genome editing without double-strand breaks or donor DNA. *Nature* **576**, 149–157 (2019).
15. Petri, K. *et al.* CRISPR prime editing with ribonucleoprotein complexes in zebrafish and primary human cells. *Nat. Biotechnol.* 1–5 (2021) doi:10.1038/s41587-021-00901-y.

5. Conclusion

Here, we have developed two novel nanomaterials. One nanomaterial utilizes the mechanics of self-assembly to disrupt the lysosome of cancer cells and thereby sensitizes non-small cell lung cancer to cisplatin chemotherapy. The other material is capable of delivering gene editing machinery to the small intestine and colon of mice. The first nanomaterial utilizes three key components to localize to the lysosome where it forms high aspect ratio nanofibers. First a hydrophobic motif, and fluorescent dye. Second the material contains the D-amino acid peptide sequence klvffk derived from the amyloid beta protein, which allows for fiber formation. Finally, the material contains the poly-arginine motif which allows for cell entry and lysosomal localization. Together these motifs form a nanoparticle which preferentially enters NSCLC cells through clathrin-mediated endocytosis, and disrupts the lysosome. This further allows for cisplatin sensitization and when dosed with cisplatin in vivo leads to good tumor response in vivo with little toxicity. However, some weight loss and liver accumulation was observed, so an improved nanomaterial was devised with the phototherapeutic porphyrin, crosslinkable side chains and heparin coating. We were able to show that this material has better biodistribution than previously developed material.

The second nanomaterial consists of Crispr-Cas ribonucleoprotein encapsulated in hepatitis E virus-like particles. We were able to show that these nanomaterials are capable of editing the gastrointestinal tract of Ai9 mice after

oral administration. RNP-HEVNP represents the first orally available Crispr-Cas delivery system.

Both nanomaterials have a bright future ahead and will continue to be developed over the coming years.